Electronic Supplementary Material (ESI) for Energy & Environmental Science.
This journal is © The Royal Society of Chemistry 2024

Electronic Supplementary Information (ESI) for

Surface Hydroxyl Group Dominating Aerobic Oxidation of Methane below Room Temperature

Baiyang Yu[a, b,#], Lu Cheng[c,#], Jiaju Wu [a, b,#], Bing Yang[d,*], Hong Li[d], Jing Xu[e], Ying Zhang[a, b], Chengsi Pan[a, b], Xiao-Ming Cao[c, f*], Yongfa Zhu[g], Yang Lou[a,b*]

[a]*Key Laboratory of Synthetic and Biological Colloids, Ministry of Education, School of Chemical and Material Engineering, Jiangnan University, Wuxi, Jiangsu 214122, China*

[b]*International Joint Research Center for Photoresponsive Molecules and Materials, Jiangnan University, Wuxi, Jiangsu 214122, China*

[c]*State Key Laboratory of Green Chemical Engineering and Industrial Catalysis, Centre for Computational Chemistry and Research Institute of Industrial Catalysis, East China University of Science and Technology, Shanghai 200237, China*

[d]*CAS Key Laboratory of Science and Technology on Applied Catalysis, Dalian Institute of Chemical Physics, 457 Zhongshan Road, Dalian, 116023, China*

[e]*School of Food Science and Technology, Jiangnan University, Wuxi, Jiangsu 214122, China*

[f]*School of Chemistry and Chemical Engineering, Shanghai Jiao Tong University, Shanghai 200240, China*

[g]*Department of Chemistry, Tsinghua University, Beijing 100084, China*

* *To whom the manuscript should be contacted: yang.lou@jiangnan.edu.cn; byang@dicp.ac.cn; xmcao@sjtu.edu.cn.*

Experimental Section

Synthesis of catalysts

Preparation of Pd_1/TS-1. The modified adsorption methods we recently developed were used to prepare the single atoms of TS-1-supported Pd via finely tuning the adsorption parameters in the aqueous solution.[1-3] TS-1 (SiO_2/TiO_2 = 30, the Brunauer–Emmett–Teller (BET) surface area of ca. 400 m^2/g; XFNANO Chemical Co.) was dispersed in deionized water (18.2 MΩ cm^{-1}). The pH of the Pd precursor ($Pd(NO_3)_2 \cdot 2H_2O$; Sinopharm Chemical Reagent Co., China) was finely tuned from 4.5 to 3.2. The diluted Pd precursors were pumped into the TS-1 suspension at approximately 0.2 mL/min under stirring. After aging for 2 h at room temperature, the sample was centrifuged and washed five times with deionized water; then, it was dried at 40 °C in vacuum to obtain Pd_1/TS-1 catalyst. The actual loading of Pd (0.95 wt.%) was measured via inductively coupled plasma optical emission spectrometer (ICP-OES).

Preparation of Pd_1/TS-1@CN. Pd_1/TS-1 coated with nitrogen-doped carbon layers was obtained via dopamine pyrolyzation.[4,5] Typically, 200 mg of as-prepared Pd_1/TS-1 was stirred in concentrated dopamine-containing (mass ratio of dopamine to catalyst: 1:400-1:0.5) tris-buffer solution (100 mL, 10 mM; pH 8.8) for 12 h. The suspension was separated via centrifugation, washed with deionized water three times and ethanol one time, and dried at 40 °C in vacuum. The obtained sample was subjected to annealing treatment at 750 °C in Ar flow for 4 h at a heating rate of 2 °C min^{-1}. The resulting samples were named on the basis of the mass ratio of dopamine to catalyst. For example, the synthesized catalyst was denoted as Pd_1/TS-1@CN (1:100) when the mass ratio was 1:100.

Preparation of Pd/TS-1 NP. The Pd nano particle catalyst (Pd/TS-1 NP) was prepared by deposition-precipitation.[6] Typically, TS-1 was dispersed in 100 mL deionized water, tuning the pH of solution to 9.0 by NaOH (purchased from Aladdin) and taking corresponding content $Pd(NO_3)_2 \cdot 2H_2O$ in 20mL deionized water to prepare metal precursor solution. Next, the diluted Pd precursors were pumped into TS-1 suspension at a speed of ~ 0.2 mL/min under stirring. At the same time, the solution of TS-1 was heated to 80 °C. After aging for 2 h at 80 °C, the sample was centrifuged and washed, finally dried at 60 °C in an oven overnight and calcined at 550 °C for 3 h in 5 % H_2. The dispersion status of Pd species is characterized by TEM and in situ CO-DRIFTs, which is detailedly discussed in **Figure S8** and **S9**.

Evaluation of catalytic performance

The DOM was performed in a 210-mL Teflon-coated stainless-steel autoclave. The catalyst (20 mg) was dispersed in 20-mL deionized water. The charged autoclave was sealed and purged three times with CH_4 gas. It was then pressurized to a desired value with CH_4, H_2, and O_2 gas (28 bar of CH_4, 1.2 bar of H_2, 6 bar of O_2 and 4.8 bar of Ar). The solution was cooled to the desired reaction temperature (15 °C), where a thermocouple was directly inserted into the solution to measure the temperature. Regarding the safe operation of experiments, such a low reaction temperature (15 °C) decreases the safety concern of using a mixture of H_2 and O_2 in the reaction system. Once the temperature reached the set value, the solution was vigorously stirred at ca. 1,200 rpm for a certain time (1 h). After the reaction, the reaction gas was analyzed via gas chromatography (GC, propark T column) equipped with a methanizer unit and FID detector. Only O_2 and CH_4 could be detected in a typical GC of gas mixture after the DOM (**Figure S56**; the detection limit of CO_2 is 1–2 ppm). The oxygenates in the liquid were analyzed based on ^{1}H NMR spectra using Bruker 400 MHz NMR. 3-(trimethylsilyl)-1-propanesulfonic acid sodium salt (DSS, purchased from TCI) was used as a calibration standard. The solvent suppression technique was used to suppress the dominant H_2O signal during NMR measurement. Moreover, 0.7 mL of the product solution was mixed with 0.1 mL D_2O (with 0.1012 μmol DSS) in the tube. The ^{1}H NMR spectra of liquid products over Pd_1/TS-1@CN (1:100) after the DOM are shown in **Figure S57**. The identified oxygenated products in liquid were dissolved methane (δ = 0.17 ppm), acetic acid (δ = 2.07 ppm), methanol (δ = 3.34 ppm), methyl hydroperoxide (δ = 3.86 ppm), methanediol (δ = 5.04 ppm), and formic acid (δ = 8.28 ppm). To accurately quantify the products, their standard curves were established respectively (**Figure S58**). Methanediol ($CH_2(OH)_2$), a product of the hydration of formaldehyde, was obtained from the diluted commercial aqueous solution of formaldehyde. Methyl hydroperoxide (CH_3OOH) was prepared in the lab using the method reported by Davies et al.[7]

The number of products was calculated based on their standard curves. The detailed calculation method is as follows: the peak area ratio of product to standard substance (4,4-dimethyl-4-silapentane-1-sulfonic acid, DSS) was obtained based

on the ^{1}H NMR spectrum. The ratio of product to standard substance (DSS) in the tube was calculated based on the standard curve. The quantity ratio of the aforementioned substances was multiplied by the quantity ratio of DSS substances in the tube (0.1012 μmol) to obtain the amount of the product in the tube. Finally, the number of products in the solution after the DOM was obtained by multiplying the corresponding proportional coefficient.

The mass yields of catalysts and the selectivity of methanol were calculated using the following equations:

$$\text{Yields of product } (\mu\text{mol}\bullet\text{gcat} - 1\bullet\text{h} - 1) = \frac{\text{Products } (\mu\text{mol})}{\text{Catalyst (g)}\bullet\text{Time (h)}}. \quad (1)$$

$$\text{Selectivity of liquid product } (\%) = \frac{\text{Total liquid products } (\mu\text{mol})}{\text{Total carbonaceous products } (\mu\text{mol})}. \quad (2)$$

In the cycling tests, 20 mg of catalysts from a total of 200 mg were used for the catalytic methane oxidation. After each cycling measurement reaction, a parallel experiment was conducted using the rest of the catalysts under identical reaction conditions. Then, all the catalysts were mixed, washed, collected, and dried at 40 °C for 12 h in vacuum to remove any organic chemicals adsorbed on catalysts. Then, 20 mg of catalysts were used from the collected samples for the next recycling experiment.

Catalyst characterization

X-ray diffraction (XRD) analysis was carried out on a Bruker D8 focus diffraction spectrometer using Cu Kα radiation with a scanning angle (2 theta) of 5-80 ° at a speed of 2 °/min, operated at 40 kV and 40 mA.

The metal loadings of the catalysts were measured by inductively coupled plasma optical emission spectroscopy (ICP-OES) on an optima 730 instrument (AGILENT ICP-OES 730).

The in-situ H_2-pulse experiments on catalyst samples were conducted on an auto-controlled flow reactor system (TP-5076, Tianjin Xianquan Instrument Co., Ltd, China) equipped with a thermal conductivity detector (TCD). The reaction temperature of in-situ H_2-pulse experiments is 15 ^{o}C and the volume of each pulse of H_2 is 1 ml (42.3 μmol). The molar quantity calculation is calculated according to the following gas law:

$$n = \frac{P\bullet V}{R\bullet T}\# \quad (3)$$

In the following gas law, n is the molars (mol); P is the pressure of H_2 (Pa); V is the volume of H_2 (m^3); R is molar gas constant (J/(mol•K)); T is temperature (K).

UV-Visible (UV-Vis) spectra of the catalysts were recorded on UV-3600 plus (SHIMADZU) in the diffuse reflectance (DR) mode at room temperature. The baseline was corrected using $BaSO_4$ as a reference material. Samples were scanned from 300 to 800 nm at a scan rate of 120 nm/min. The intensity of the UV-vis DR spectra was presented in the form of the Kubelka-Munk function.

High resolution transmission electron microscopy (HR-TEM) images were collected on a JEM-2100 transmission electron microscope (JEOL, Japan) with an acceleration voltage of 200 kV.

Nitrogen adsorption-desorption isotherms were measured at -196 °C on an ASAP 2460 analyzer (Micromeritics Co. Ltd.). Before the measurement, the sample was degassed at 120 °C for 24 h under vacuum to remove moisture and impurities. The Brumauer Emmett Teller (BET) method was used to calculate the specific surface areas and pore sizes of samples.

Raman spectroscopy was performed on a Renishaw Invia + Reflex Raman spectrometer with a CCD detector, and the wavelength of the excitation line was 514 nm.

X-ray photoelectron spectra (XPS) were carried out on a Thermo ESCALAB 250Xi spectrometer using Al-Kα radiation source. The binding energies were calibrated using C1s peak of contaminant carbon (Binding Energy = 284.8 eV) as an internal standard. Pd K-edge XAFS analyses were performed with Si (311) crystal monochromators at the BL14W Beam line at the Shanghai Synchrotron Radiation Facility (SSRF) (Shanghai, China). Before the analysis at the beamline, samples were placed into aluminum sample holders and sealed using Kapton tape film. The XAFS spectra were recorded at room temperature using a 4-channel Silicon Drift Detector (SDD) Bruker 5040.

Pd K-edge extended X-ray absorption fine structure (EXAFS) spectra were recorded in fluorescence mode. Negligible changes in the line-shape and peak position of Pd K-edge XANES spectra were observed between two scans taken for a specific sample. The XAFS spectra of these standard samples were recorded in transmission mode. The spectra were processed and analyzed by the software codes Athena and Artemis.

Electron paramagnetic resonance (EPR) measurements were performed on a Bruker EMX plus model spectrometer operating at the X-band frequency at 298 K, with an operating frequency of 9.85 GHz and a microwave power of 2 mW.

Diffuse reflectance infrared Fourier transform (DRIFT) spectra of chemisorbed CO were recorded in an in-situ diffuse reflectance cell on a Nicolet iS50 spectrometer (Thermo Scientific). Each spectrum was collected for 64 scans at a resolution of 4 cm^{-1}. The temperature was tested at room temperature for CO chemisorption. After collecting a background spectrum of the sample under the Ar gas, the cell was switched to 1 vol.% CO/Ar mixed gas for CO adsorption for 1 h, followed by purging with the Ar gas. The collected spectra were subtracted from the sample background spectra in Ar gas to obtain the spectra for chemisorbed CO.

5,5-dimethyl-1-pyrroline N-oxide (DMPO) spin-trapping electron paramagnetic resonance (EPR) experiments were conducted on a Bruker Emxplus spectrometer at 15 °C. For extra H_2O_2 sample, 20 mg catalyst, 0.2 mL DMPO (50 mg/mL) and 20 mL 0.5 M H_2O_2 solution were added into a 210 ml autoclave and stirred at 1200 rpm for 10 min. For in-situ H_2O_2 sample, 20 mg catalyst, 0.2 mL DMPO (50 mg/mL), 20 mL D.I. H_2O solution was added into a 210 ml autoclave and pressurized with 12 bar H_2 and O_2, then stirred at 1200 rpm for 10 min.

In the isotopic tracer experiments, 20 mg catalyst was dispersed in 20 mL deionized water ($H_2{}^{16}O$). ^{18}O labelled O_2 (≥ 99 %) was used in the co-reaction with CH_4 and H_2. The reactions were performed at 15 °C for 1h with an initial partial pressure of 28 bar, 6 bar and 6 bar for CH_4, O_2 and H_2, respectively. ^{18}O labelled H_2O (≥ 99 %) was alternatively used to verify the participation of the oxygen atom from H_2O in the co-reactions with $^{16}O_2$ under the same conditions. After the reaction, the liquid oxygenates (such as CH_3OH) were measured by Pegasus HRT+4D (LECO, USA). The isotopic tracer experiment of ^{13}C is similar. 20 mg catalyst was dispersed in 10 mL deionized water. ^{13}C labelled CH_4 (≥ 99 %) was used in the reaction with O_2, H_2 and Ar. The reactions were performed at 15 °C for 2 h with an initial partial pressure of 2 bar, 6 bar, 1.2 bar and 30.8 bar for $^{13}CH_4$, O_2, H_2 and Ar, respectively. After the reaction, the liquid oxygenates (such as CH_3OH) were measured by Pegasus HRT+4D (LECO, USA) and ^{13}C NMR spectra using Bruker 400 MHz NMR.

The laser-induced fluorescence (LIF) spectrum was used to further detect surface adsorbed •OH*. The •OH* radicals adsorbed on the Pd_1/TS-1@CN surface after the treatment of H_2+O_2 were detected by monitoring the LIF on the A-X transition. The •OH* radicals were excited by the $A^2\Sigma^+(v'=1)\leftarrow X^2\Pi(v=0)$ transition around 282 nm, and the fluorescence of the $A^2\Sigma^+(v'=1)\rightarrow X^2\Pi(v''=1)$ transition around 310 nm was collected on a photomultiplier tube through two quartz glass lenses and a monochromator. The signals were detected by a photo-luminescence spectrometer (FS5, Edinburgh, UK).

Diffuse reflectance infrared Fourier transform spectra (DRIFTs) of reactive gas (H_2, O_2, and CH_4) were recorded in an in-situ diffuse reflectance cell on a Nicolet iS50 spectrometer (Thermo Scientific). Each spectrum was collected for 64 scans at a resolution of 4 cm^{-1}. The sample was pretreated in the cell with a flowing Ar gas at 120 °C for 30 min. The temperature was then cooled down to 15 °C and connected to a gas chamber that permitted the adjustment of the gas pressure into the cell. After collecting a background spectrum of the sample under the Ar gas, for DRIFTs with H_2 and O_2 as probe molecules, the cell was switched to 99.9 vol.% O_2 and 99.9 vol.% H_2 gas for H_2 and O_2 adsorption and reaction for 30 min to obtain the in-situ FT-IR spectrum. The collected spectra were subtracted from the sample background spectra in Ar gas to obtain the spectra for chemisorbed various hydroxyl species. For H_2-O_2-CH_4 DRIFTs, after adsorption and reaction of H_2 and O_2 for 30 min, the gas pipeline is directly switched to 99.9 vol.% CH_4 for CH_4 adsorption and reaction for 30 min to obtain the in-situ FT-IR spectrum. For pure CH_4-DRIFTs, after the cell cooling down to 15 °C, the 99.9 vol.% CH_4 is directly introduced to sample cell for CH_4 adsorption for 30 min to obtain the in-situ FT-IR spectrum without the adsorption of H_2 and O_2.

Theoretical calculation methods and model construction

To disclose the mechanism of the DOM catalyzed by Pd_1/TS-1@CN, the periodic density functional theory calculations were performed using the Vienna Ab-initio simulation package.[8] The projector augmented wave method was

used to describe the interaction between atomic nuclei and electrons. The cutoff energy of the plane wave was set to 450 eV.[9] The van der Waals interaction in zeolite was described in the DFT-D3(BJ) scheme,[10] and the generalized gradient approximation PBE functional was used to describe the exchange correlation.[11] The convergence criterion value was set to 0.05 eV/Å for the maximal force of all the relaxed atoms. The constraint minimization method was used to determine the transition state with the same force convergence criterion.[12] The vibrational frequency analysis was further performed based on harmonic oscillator approximation to confirm the TS with one imaginary vibrational frequency and the corresponding vibrational mode along the reaction coordination. The Gibbs free energy calculation details (including zero-point energy, internal energy, and entropy contribution) can be found in our previous work.[13] In particular, the molecular entropy confined in the TS-1 zeolite pore lost 38% compared to the free gas molecule.[14] Accordingly, the value of lost molecular entropy was used to correct the small molecule entropy of TS-1 zeolite.

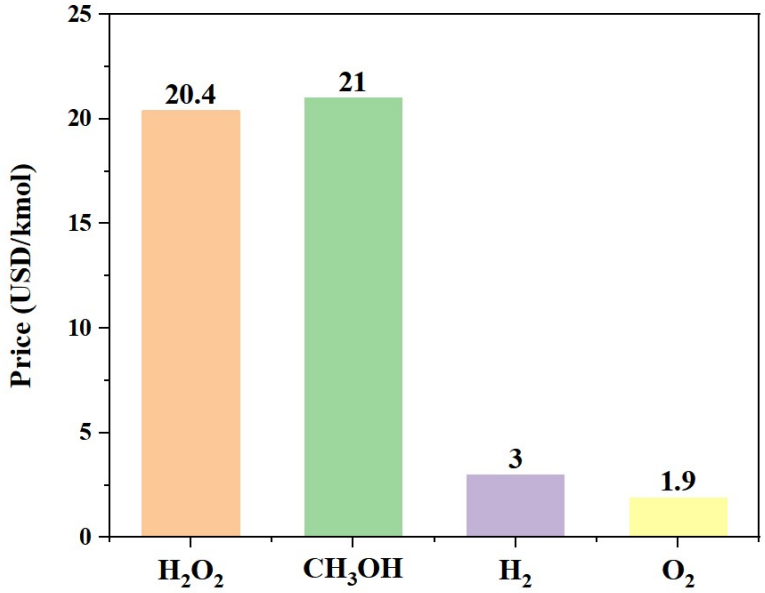

Fig. S1 The price of H_2O_2, CH_3OH, H_2 and O_2. The price derived from the references[15-18], respectively.

The price of H_2O_2 is approximately 20.4 USD per kilomole, which is similar to that of the product, methanol (21 USD per kilomole). Alternatively, the price of H_2 is approximately 3 USD per kilomole, and O_2 is approximately 1.9 USD per kilomole, which is much cheaper and more economically valuable than using H_2O_2.[15-18]

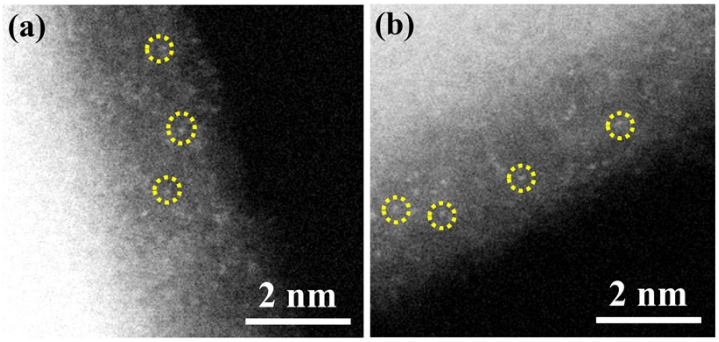

Fig. S2 HAADF-STEM images of fresh Pd_1/TS-1 (a-b).

The single Pd atoms can be directly visualized on TS-1 for Pd_1/TS-1 from the HAADF-STEM images, indicating that the palladium species are atomically dispersed on TS-1.

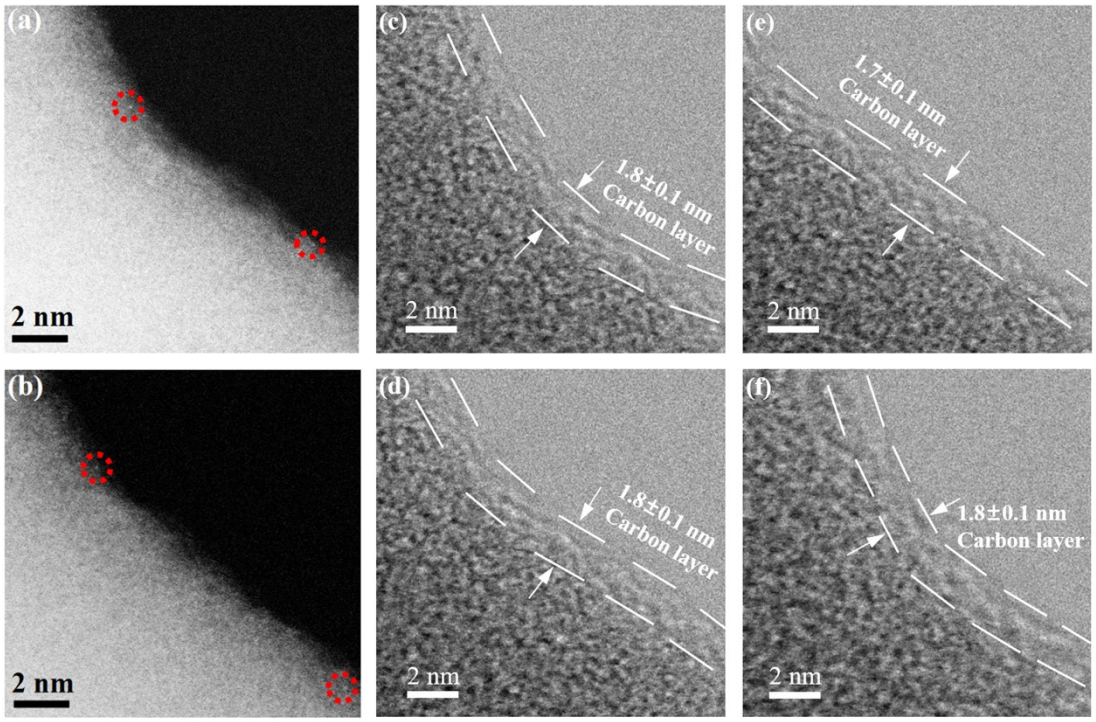

Fig. S3 HAADF-STEM images of fresh Pd_1/TS-1@CN (1:100) (a-f).

The single Pd atoms (red circles) can be directly detected on fresh Pd_1/TS-1@CN (1:100), indicating that coating thin carbon layers did not change the dispersion of Pd species supported on TS-1. Furthermore, the thickness of carbon layers on Pd_1/TS-1 (1:100) is around 3 (~1.8 nm) layers[19] as confirmed by HAADF-STEM.

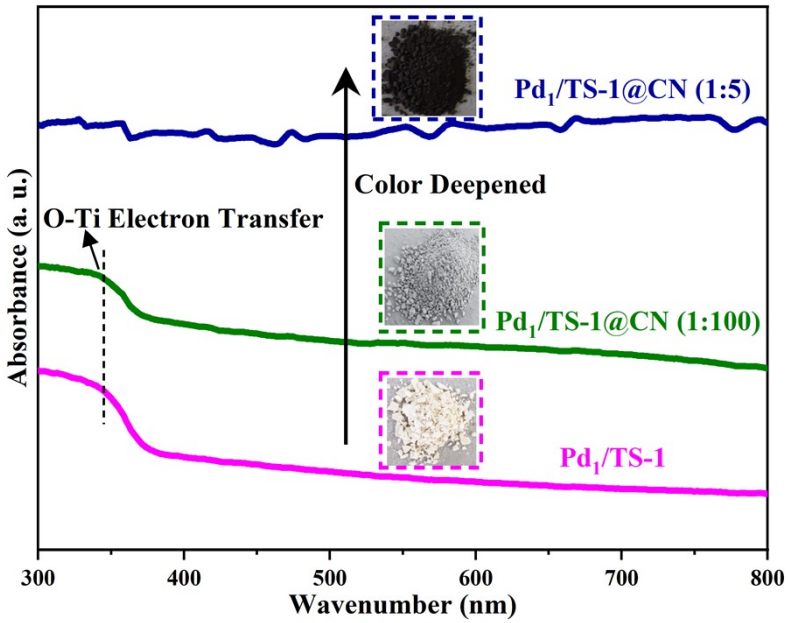

Fig. S4 The UV-Vis DR spectra of Pd_1/TS-1, Pd_1/TS-1@CN (1:100) and Pd_1/TS-1@CN (1:5).

The thickness of N-doped carbon layers can be precisely controlled by tuning the mass ratio of dopamine to catalyst. As confirmed by the gradual color change from light yellow to black (inset) and the UV-Vis DR spectra, the characteristic O-Ti electron transfer (peak centered at 340 nm) in TS-1 support gradually turns invisible compared with that of Pd_1/TS-1 when the mass ratio gradually increases.[20]

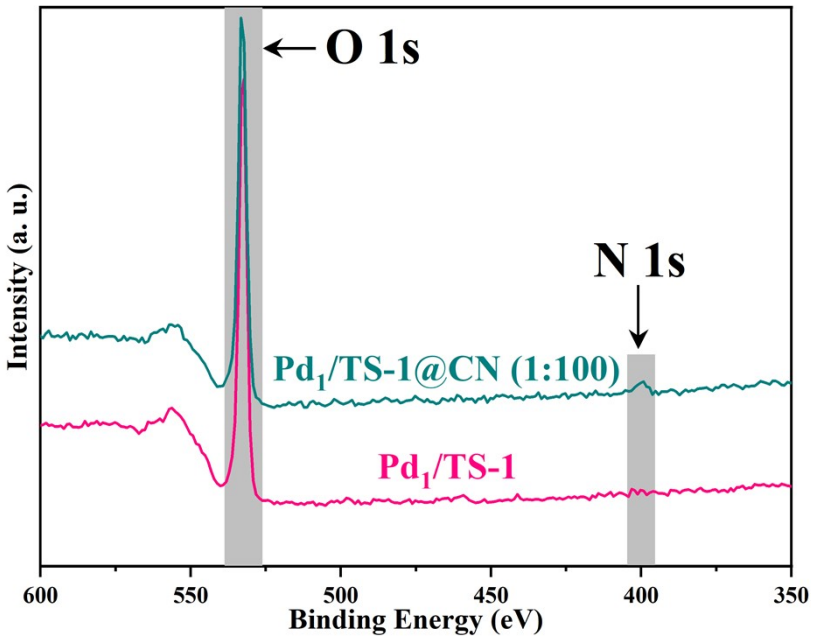

Fig. S5 X-ray photoelectron spectroscopy of Pd_1/TS-1 and Pd_1/TS-1@CN (1:100).

X-ray photoelectron spectroscopy (XPS) revealed the presence of N 1s signal at ~400 eV in Pd_1/TS-1@CN (1:100) compared with Pd_1/TS-1, suggesting that N element exists in the coated carbon layers.[21,22]

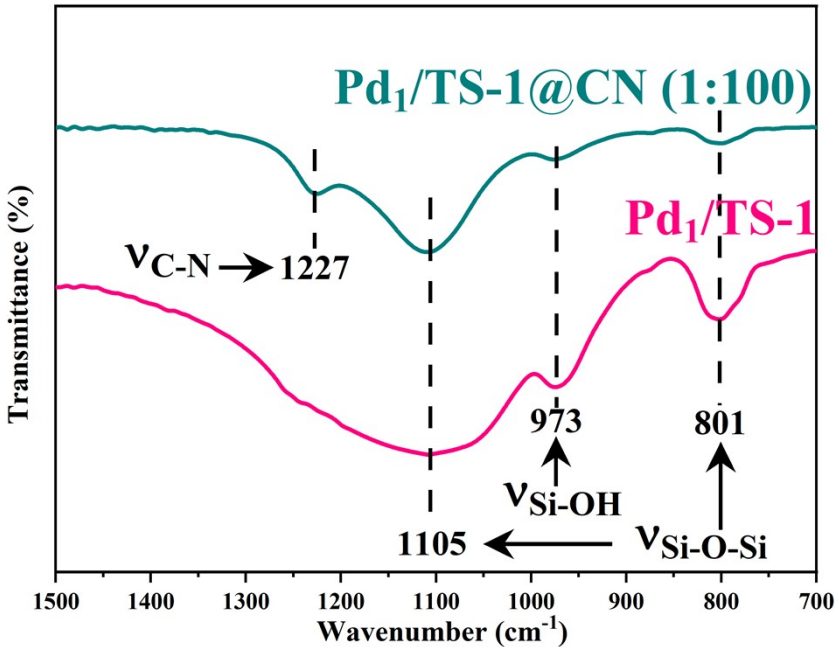

Fig. S6 Comparison of FT-IR spectra for Pd_1/TS-1 and Pd_1/TS-1@CN (1:100).

The FT-IR spectra of Pd_1/TS-1@CN (1:100) exhibited the characteristic stretching vibration modes of the C-N group at around 1,227 cm^{-1}, clearly indicating that the coated carbon layers are doped with N element.[23] In addition, the typical absorption peaks of both Pd_1/TS-1 and Pd_1/TS-1@CN (1:100) associated with the symmetric stretching vibration ν_s (Si-O-Si) at 801 cm^{-1}, the asymmetric stretching vibration ν_{as} (Si-O-Si) at 1,105 cm^{-1} and the Si-OH stretching vibration at 973 cm^{-1} were found.[24]

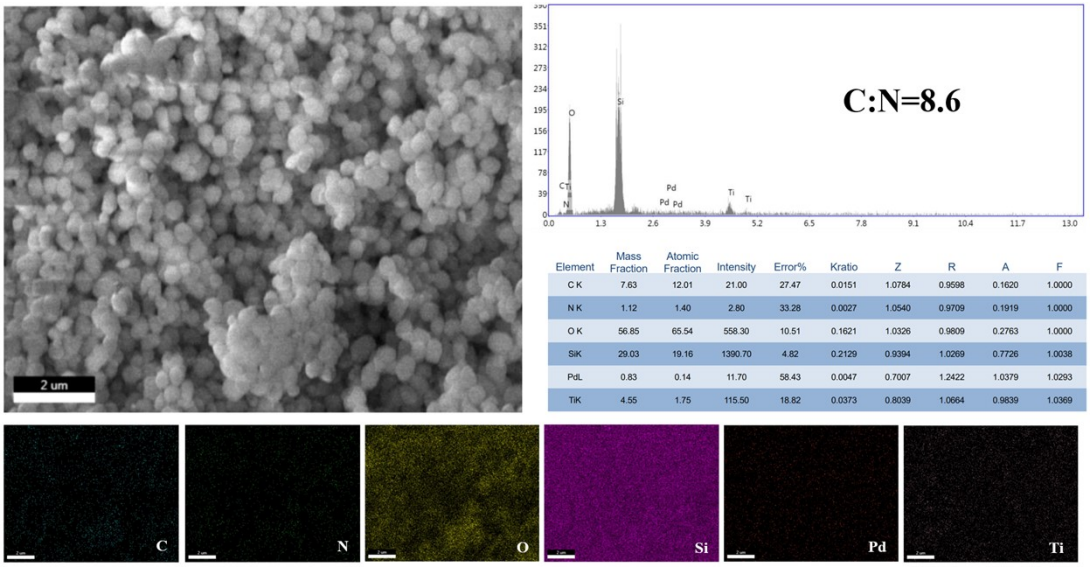

Element	Mass Fraction	Atomic Fraction	Intensity	Error%	Kratio	Z	R	A	F
C K	7.63	12.01	21.00	27.47	0.0151	1.0784	0.9598	0.1620	1.0000
N K	1.12	1.40	2.80	33.28	0.0027	1.0540	0.9709	0.1919	1.0000
O K	56.85	65.54	558.30	10.51	0.1621	1.0326	0.9809	0.2763	1.0000
SiK	29.03	19.16	1390.70	4.82	0.2129	0.9394	1.0269	0.7726	1.0038
PdL	0.83	0.14	11.70	58.43	0.0047	0.7007	1.2422	1.0379	1.0293
TiK	4.55	1.75	115.50	18.82	0.0373	0.8039	1.0664	0.9839	1.0369

Fig. S7 Energy-dispersive X-ray spectroscopy of Pd_1/TS-1@CN (1:100).

The energy-dispersive X-ray spectroscopy clearly confirms that the ratio of nitrogen-to-carbon is 1:8.6.

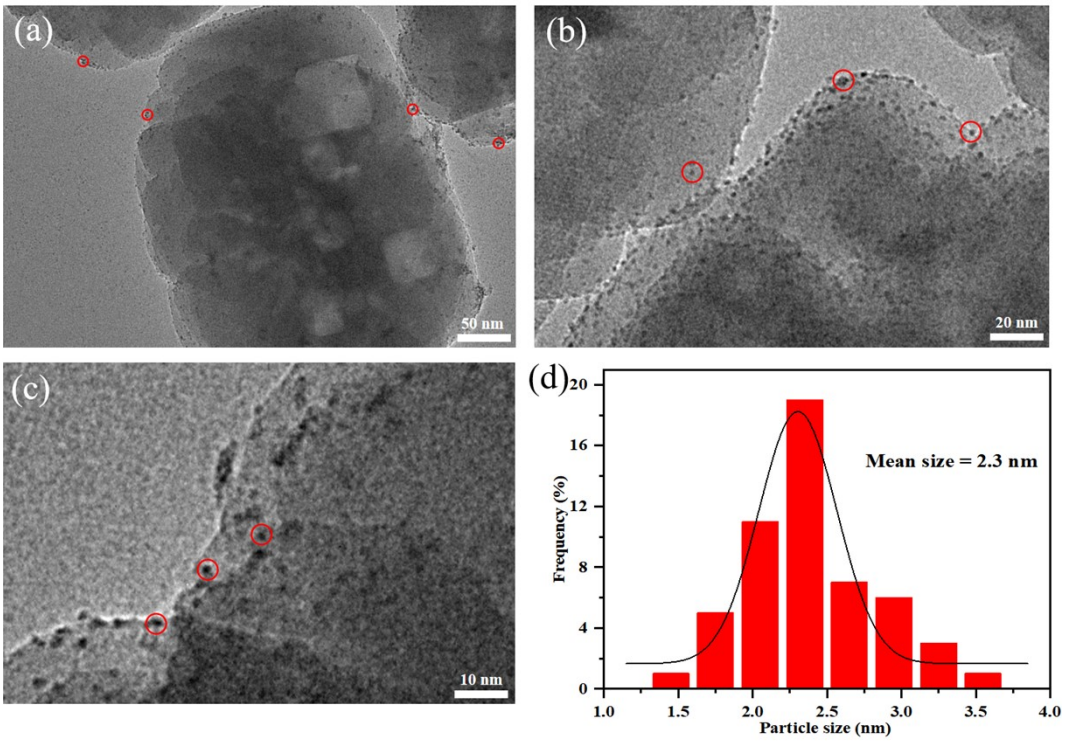

Fig. S8 TEM images of Pd/TS-1 NP (a-d) wherein the cycles marked the nanoparticle site.

It can be observed the aggregated Pd (red circles) suggesting that Pd atoms in Pd/TS-1 NP are in the form of nanoparticles. The average size of Pd particles is 2.3 ± 0.5 nm.

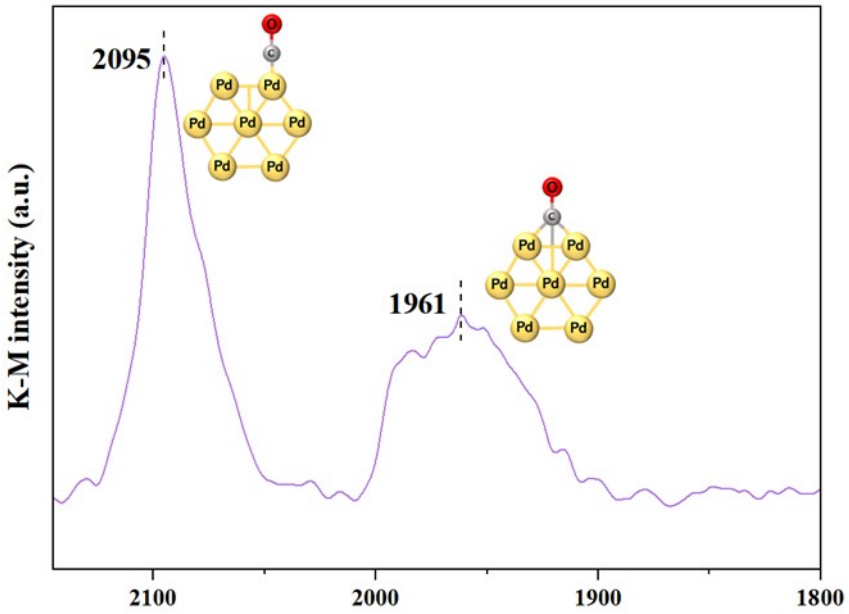

Fig. S9 CO-DRIFTs of Pd/TS-1 NP.

According to the CO-DRIFTs, the Pd/TS-1 NP exhibits linear (centered at 2,095 cm^{-1}) and bridge CO adsorption (centered at 1,961 cm^{-1}) on Pd nanoparticles[25], indicating that the Pd species are in the form of nanoparticles.

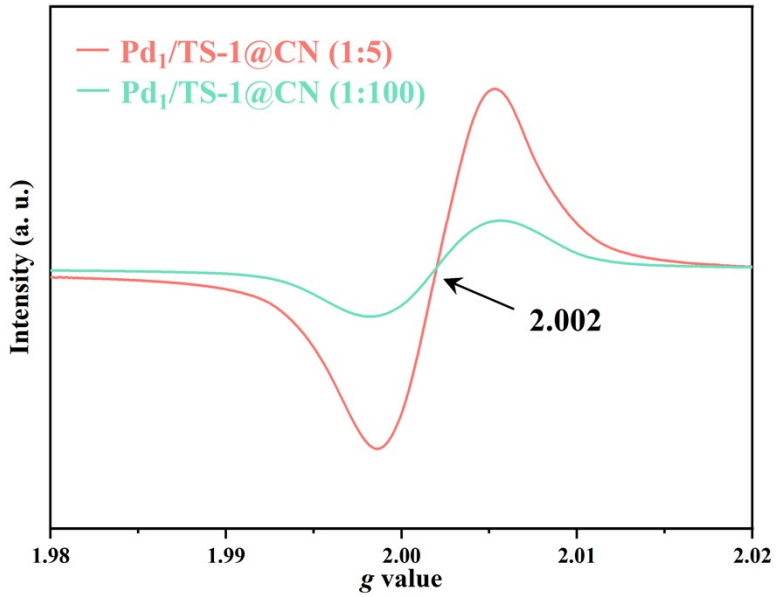

Fig. S10 The electron paramagnetic resonance data of Pd_1/TS-1@CN (1:100) and Pd_1/TS-1@CN (1:5).

The enhanced electron paramagnetic resonance (EPR) signal (g=2.002) associated with the unpaired electron on the carbon atoms of the aromatic rings within Π-bonded nanosheets confirms the presence of more vacancy defects in Pd_1/TS-1@CN (1:5) compared with that in Pd_1/TS-1@CN (1:100)[26], which guarantees better accessibility of reactants to the active sites.[27]

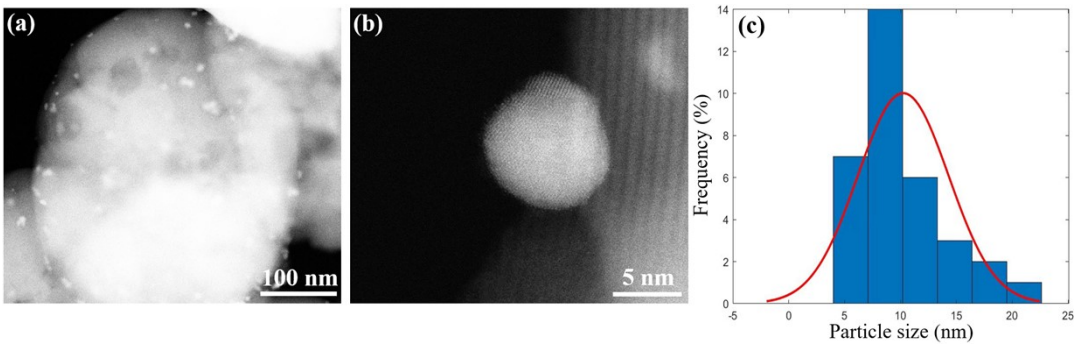

Fig. S11 HAADF-STEM images of used Pd_1/TS-1 (after 5 cycles) (a-b) and corresponding statistical analysis on particle size (c).

The size distribution of Pd particles is acquired by using the software to count the number and gauge the size of nano particles. The average size of Pd nanoparticles on the used Pd_1/TS-1 is 10.2 ± 3.3 nm.

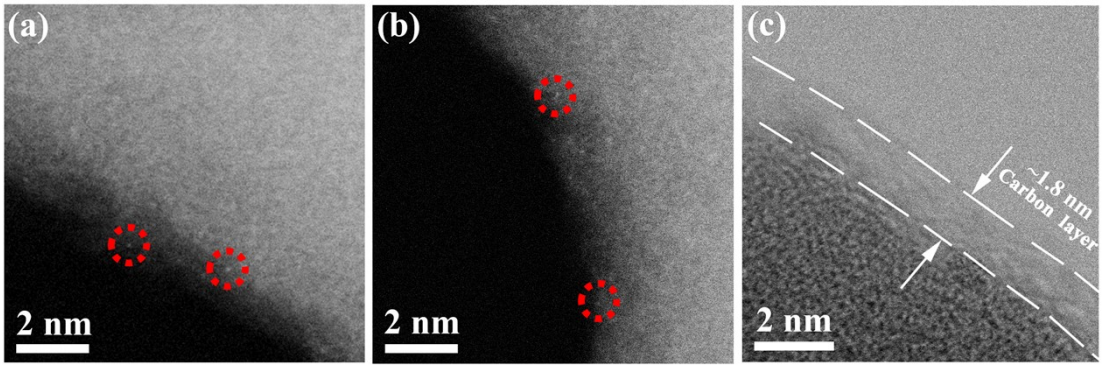

Fig. S12 HAADF-STEM images of used Pd_1/TS-1@CN (1:100) (after 30 cycles) (a-c).

The single Pd atoms (red circles) can still be directly detected on used Pd_1/TS-1@CN (1:100), indicating that the strategy of coating thin carbon layers significantly enhanced the stability of single Pd atoms anchored on TS-1. In addition, the thickness of carbon layer (~ 1.8 nm) on used Pd_1/TS-1@CN (1:100) is almost unchanged compared with the fresh sample (~ 1.8 nm), which also confirms the excellent stability of the carbon layers coated on Pd_1/TS-1.

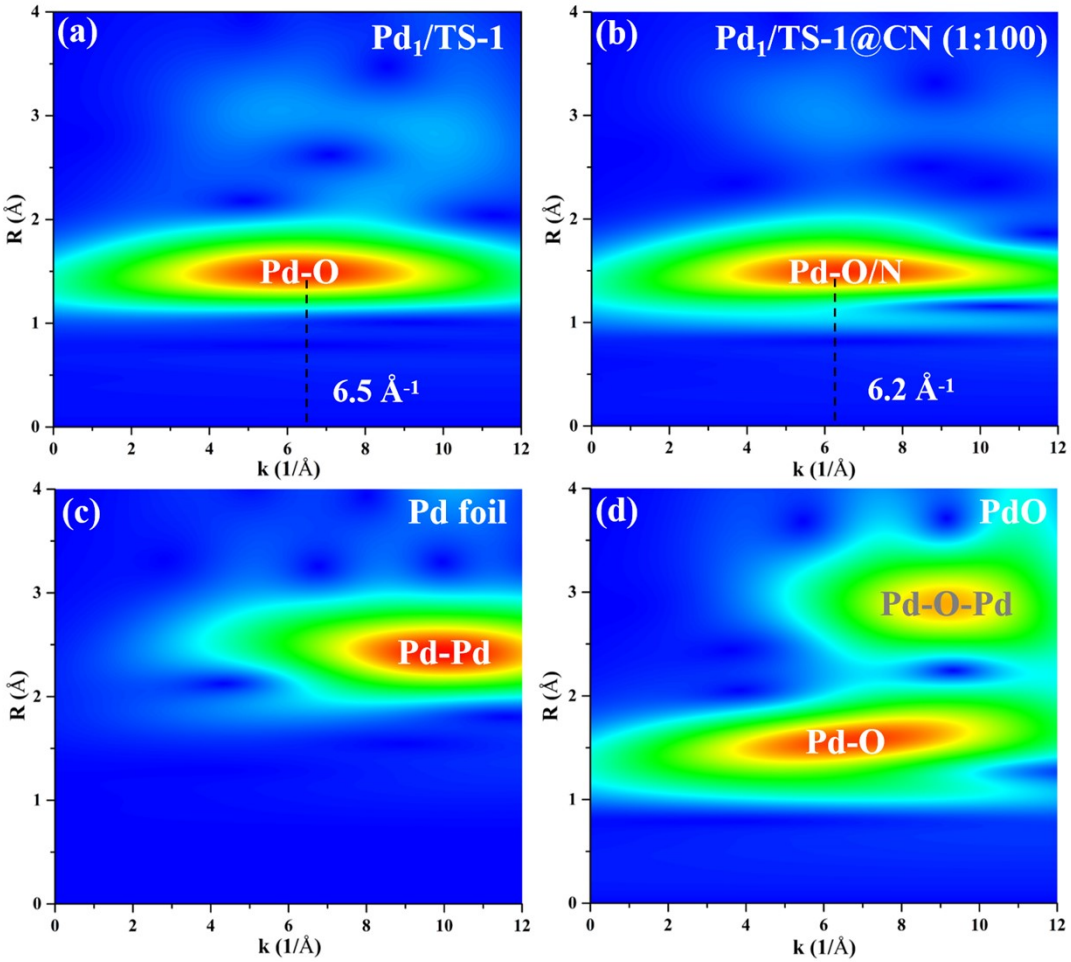

Fig. S13 Wavelet transform (WT) analysis of the Pd K-edge EXAFS oscillations of Pd_1/TS-1 (a), Pd_1/TS-1@CN (1:100) (b), Pd foil (c), and PdO (d).

In order to reveal the local coordination of Pd species in Pd_1/TS-1 and Pd_1/TS-1@CN (1:100) more clearly, the wavelet transform (WT) of the Pd K-edge EXAFS oscillations is analyzed. No intensity maximum related to Pd-Pd (10.0 $Å^{-1}$) or Pd-O-Pd (9.5 $Å^{-1}$) coordination can be observed in both Pd_1/TS-1 and Pd_1/TS-1@CN (1:100) compared with that of the reference Pd foil and PdO samples, which confirms that Pd atoms are atomically dispersed on both Pd_1/TS-1 and Pd_1/TS-1@CN (1:100) and is in agreement with the HAADF-STEM results. The WT contour plots of Pd_1/TS-1@CN (1:100) (6.2 $Å^{-1}$) present a lower center of gravity compared with that of Pd_1/TS-1 (6.5 $Å^{-1}$), indicating that part of the O ligands coordinated with Pd atom are changed into N ligands. These results clearly demonstrate that the thin N-doped carbon layers coated on Pd_1/TS-1 have significantly modulated the local coordination environment of single Pd atoms.

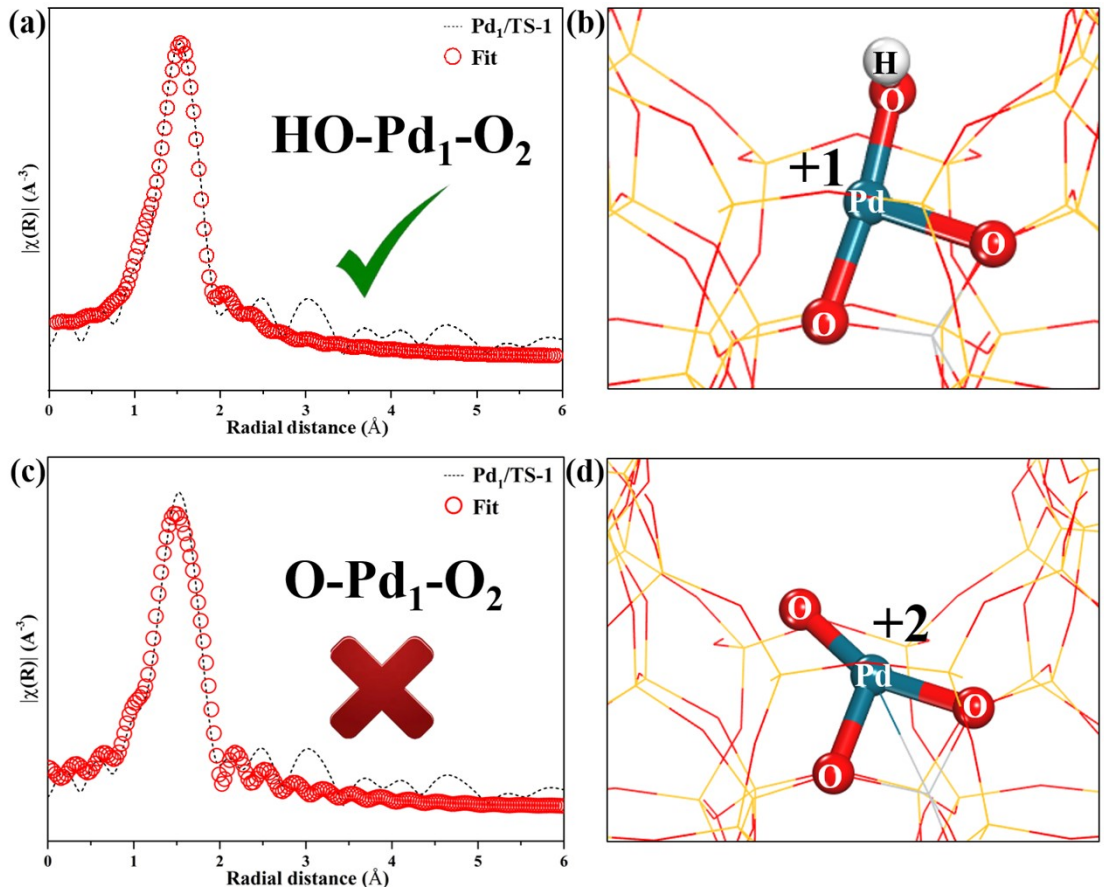

Fig. S14 EXAFS fitting curve for Pd_1/TS-1 and the corresponding valence state of Pd atom via Bader charge analysis.

For Pd_1/TS-1 sample, two model active sites have been compared since each Pd atom is coordinated with three oxygen atoms as verified by EXAFS data, but only the HO-Pd_1-O_2 is the most reliable reaction site (R-factor=0.017), which secures that the fitting results are reliable and enable to accurately demonstrate the local structure of isolated Pd atoms in the Pd_1/TS-1. The detailed fitting data reveals that Pd atoms are coordinated with one hydroxyl oxygen (O_{OH}) and two framework oxygens (O_{FM}), respectively. In addition, the R-factors of O-Pd_1-O_2 (0.053) model that fitted original EXAFS data are obviously higher than that of HO-Pd_1-O_2 model (R-factor=0.017), which further confirms that the HO-Pd_1-O_2 is the most reliable reaction site.

Furthermore, the Bader charges of Pd^+ in Pd_2O and Pd^{2+} in PdO are respectively +0.41|e| and +0.89|e| (**Table S6**). The Bader charge analysis shows that the charges in HO-Pd_1-O_2 and O-Pd_1-O_2 are +0.44|e| and +0.88|e|, respectively, which indicates the oxidation state of Pd in HO-Pd_1-O_2 is Pd^+ and the oxidation state of Pd in O-Pd_1-O_2 is Pd^{2+}. Combined with the XANES and XPS data, the oxidation state of Pd species in HO-Pd_1-O_2 configuration is more reasonable. These results provide solid evidence that the HO-Pd_1-O_2 configuration as the active site of the Pd_1/TS-1 catalyst is reliable.

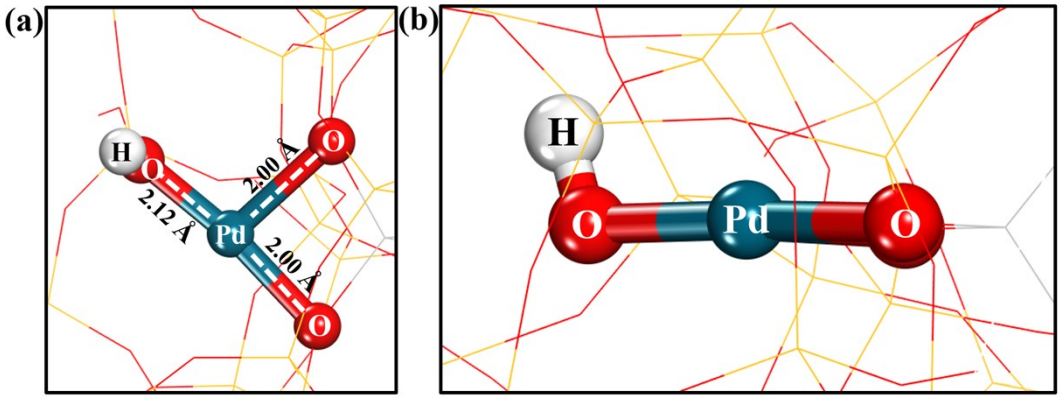

Fig. S15 The geometric configuration of Pd_1-O_3 in Pd_1/TS-1. The vertical view of (a) and the front view of (b).

The bond length of single Pd atom and hydroxyl oxygen (Pd-O_{OH}) is 2.12 Å and the average bond length of single Pd atom and framework oxygen (Pd-O_{FM}) is 2.00 Å as shown in **Table S4**.

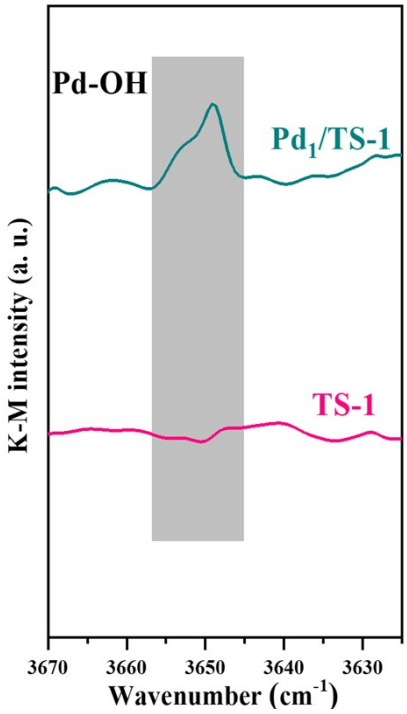

Fig. S16 Comparison of diffuse reflectance infrared Fourier transform spectra for Pd_1/TS-1 and TS-1.

As confirmed by FT-IR spectra for Pd_1/TS-1 and TS-1, the peak centered at approximately 3,650 cm^{-1} is associated with Pd-OH in Pd_1/TS-1[28], indicating the configuration of the Pd center in Pd_1/TS-1 is HO-Pd_1-O_2 rather than O-Pd_1-O_2.

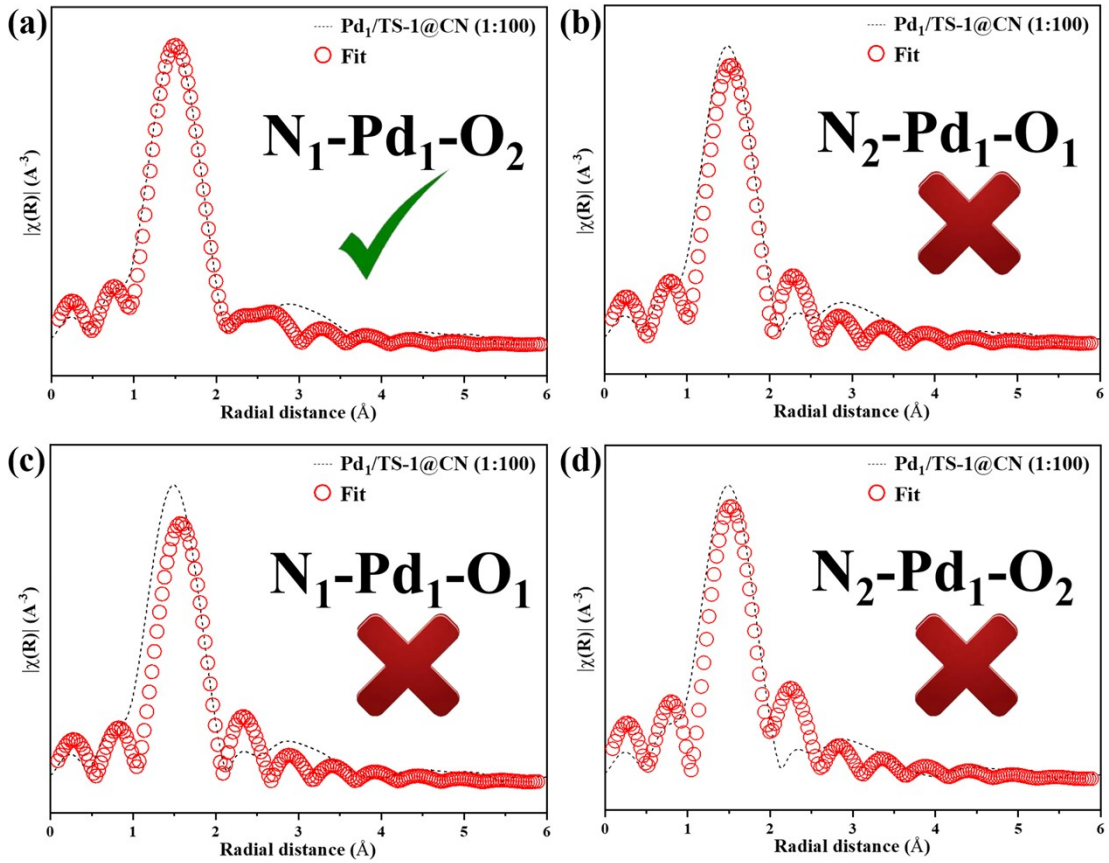

Fig. S17 EXAFS fitting curve for Pd_1/TS-1@CN (1:100) by using the models of N_1-Pd_1-O_2, N_2-Pd_1-O_1, N_1-Pd_1-O_1 and N_2-Pd_1-O_2.

Based on the XANES analysis of C, N and O species, the single Pd atoms on Pd_1/TS-1@CN (1:100) are both coordinated with O and N ligands. Furthermore, several model active sites have been searched by DFT optimized but only the N_1-Pd_1-O_2 is the most reliable reaction site (R-factor=0.009), where the isolated Pd atoms are coordinated with two framework oxygen atom of TS-1 and one pyrrole nitrogen atoms of N-C coating. In addition, the R-factors of N_2-Pd_1-O_1 (0.078), N_1-Pd_1-O_1 (0.135) and N_2-Pd_1-O_2 (0.112) models are obviously higher than that of N_1-Pd_1-O_2 model (R-factor=0.009), which further confirms that the N_1-Pd_1-O_2 is the most reliable reaction site.

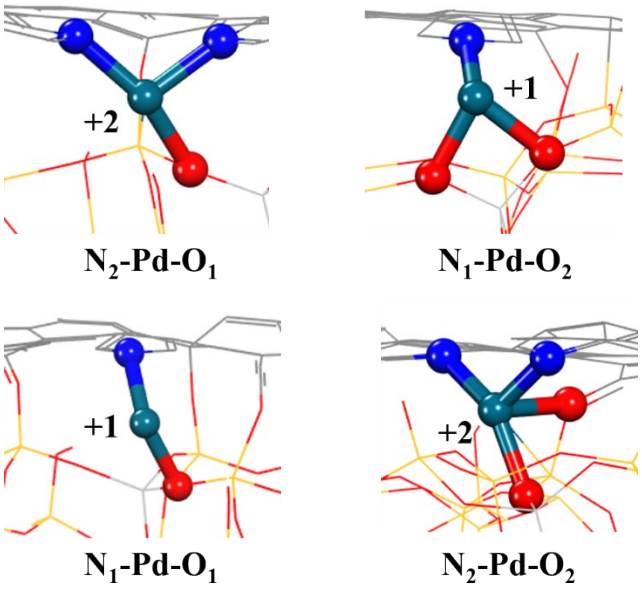

Fig. S18 The optimized structures of N_2-Pd_1-O_1, N_1-Pd_1-O_2, N_1-Pd_1-O_1 and N_2-Pd_1-O_2 with the valence state of Pd atom.

The analysis of CO-DRIFTs, HAADF-STEM, EXAFS, and WT data of the Pd_1/TS-1@C catalyst indicates that the active site has a mononuclear structure. Once the TS-1 structure is optimized, we investigate the potential mononuclear Pd active sites, including N_1-Pd_1-O_2, N_2-Pd_1-O_1, N_1-Pd_1-O_1 and N_2-Pd_1-O_2. The detailed EXAFS fitting data verifies that each Pd atom is coordinated with one nitrogen atom and two framework oxygen atoms. We find that the detailed bond length and coordination structure of the modeled N_1-Pd_1-O_2 species in the active site fit the EXAFS data well, which confirms the accuracy of the built active-site model of the Pd_1/TS-1@CN catalyst for DFT simulation. The valence state of the Pd_1 atoms of Pd_1/TS-1@CN is close to the Pd^+, consistent with XANES and XPS characterization. These provide reliable evidence to model the active site of the Pd_1/TS-1@CN catalyst. The Bader charge analysis shows that the charges in N_2-Pd-O_1, N_1-Pd-O_2, N_1-Pd-O_1 and N_2-Pd-O_2 are +0.83|e|, +0.45|e|, +0.41|e|, and +0.89|e|, respectively. According to the reference Bader charges of Pd^+ in Pd_2O and Pd^{2+} in PdO (**Table S6**), the valence states of Pd atom correspond to +2, +1, +1, and +2, respectively.

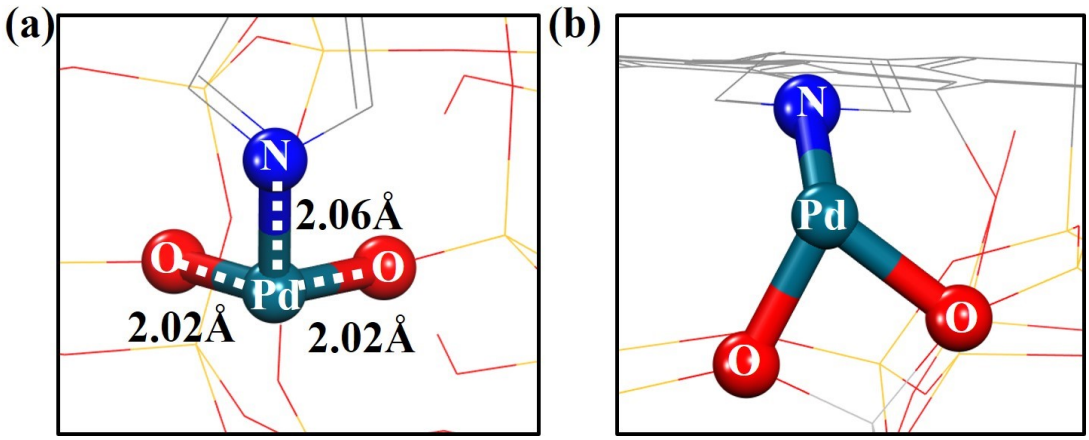

Fig. S19 The geometric configuration of N_1-Pd_1-O_2 in Pd_1/TS-1@CN (1:100). The vertical view (a) and the front view (b).

The bond length of single Pd atom and pyrrole nitrogen (Pd-N) is 2.06 Å and the average bond length of Pd and framework oxygen (Pd-O_{FM}) is 2.02 Å as verified by the EXAFS fitting data (**Table S5**).

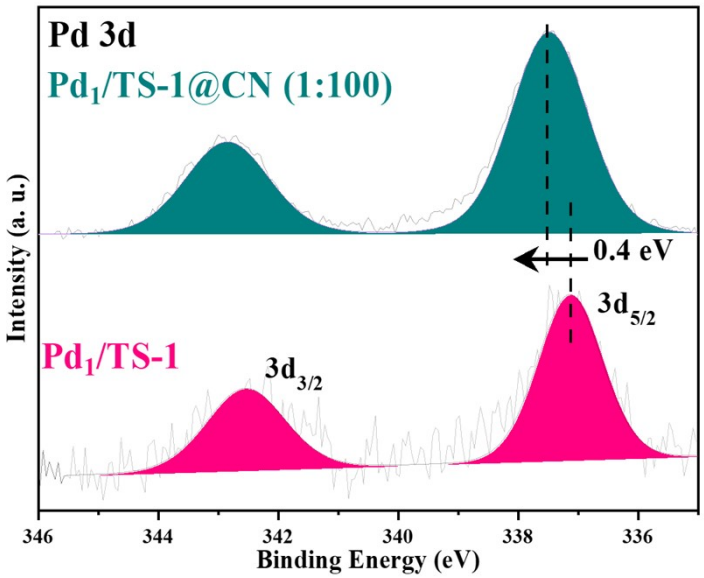

Fig. S20 XPS spectra of Pd 3d for Pd_1/TS-1 and Pd_1/TS-1@CN (1:100).

For Pd_1/TS-1 sample, there is one peak centered at 337.1 eV in the Pd $3d_{5/2}$, slightly higher than that of metallic Pd species (335.6 eV) and lower than that of Pd^{2+} species (338.6 eV), which is in line with the XANES data.[29-31] For Pd_1/TS-1@CN (1:100), there is one peak centered at 337.5 eV in the Pd $3d_{5/2}$ signal, around 0.4 eV higher than that of Pd_1/TS-1, which indicates that the valence state of the single Pd atoms is increased after coating N-doped carbon layers and corroborates the XANES data.[32]

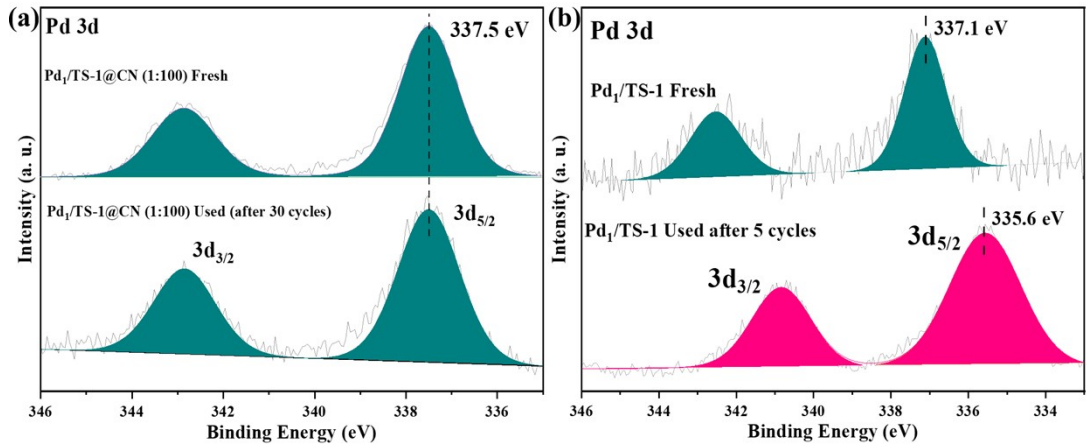

Fig. S21 XPS spectra of Pd_1/TS-1@CN (1:100) fresh and Pd_1/TS-1@CN (1:100) used (after 30 cycles) (a); XPS spectra of Pd_1/TS-1 fresh and Pd_1/TS-1 used (after 5 cycles) (b).

The valence state of metal atom is determined by its coordination environment.[33,34] The XPS data over Pd_1/TS-1@CN (1:100) used for 30 cycles exhibit that there is no shifting for the binding energy of Pd 3d orbit compared with the fresh catalyst (both of 337.5 eV for $Pd_{5/2}$), indicating the valence state of the Pd species is unchanged after the DOM reaction. By contrast, the XPS spectra over Pd_1/TS-1 after 5 cycles show that the binding energy of Pd 3d decreased by 1.5 eV compared with the fresh catalyst and the peak centered at 335.6 eV of $Pd_{5/2}$ is assigned to the metallic Pd species[35,36], suggesting that the Pd species clustered to nanoparticles after the DOM reaction. These results demonstrate that coating thin carbon layers could significantly enhance the stability of single Pd atoms supported on TS-1, which is consistent with the results of HAADF-STEM.

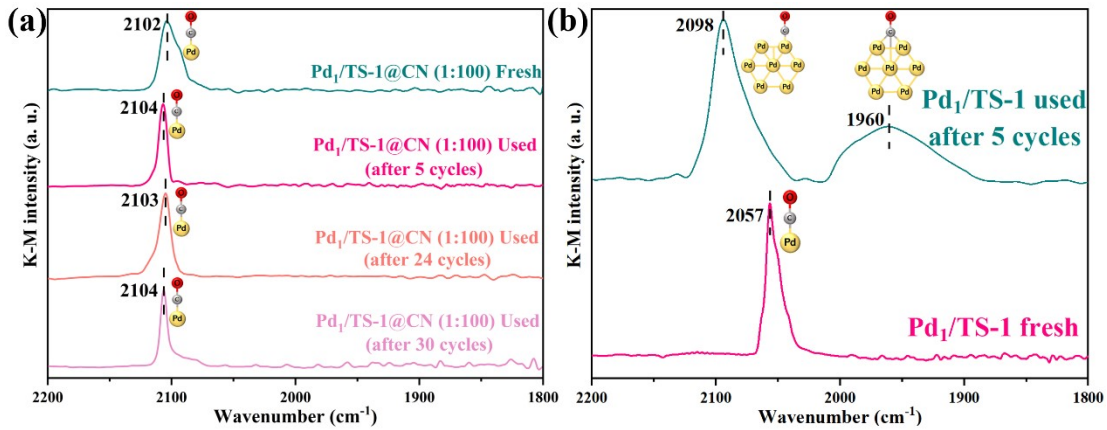

Fig. S22 CO-DRIFTs of fresh and used Pd_1/TS-1@CN (1:100) (a); CO-DRIFTs of fresh and used Pd_1/TS-1 (b).

For CO adsorption over used Pd_1/TS-1@CN (1:100) samples (after 5, 24, 30 cycles, respectively), there is only one peak (2,103 ± 1 cm^{-1}) associated with CO linear adsorption on the isolated Pd sites (Pd_1-CO).[2,37] Besides, no bridge-adsorbed CO peaks under 2,000 cm^{-1} are observed on all used Pd_1/TS-1@CN (1:100) samples, which suggests that the single Pd atoms are stably anchored on the support during the DOM reaction.[2,37] However, the reference Pd_1/TS-1 catalyst after 5 cycles shows linear (centered at 2,098 cm^{-1}) and bridge CO adsorption (centered at 1,960 cm^{-1}) on Pd nanoparticles[25], indicating that the Pd species are not stable under the DOM reaction condition.

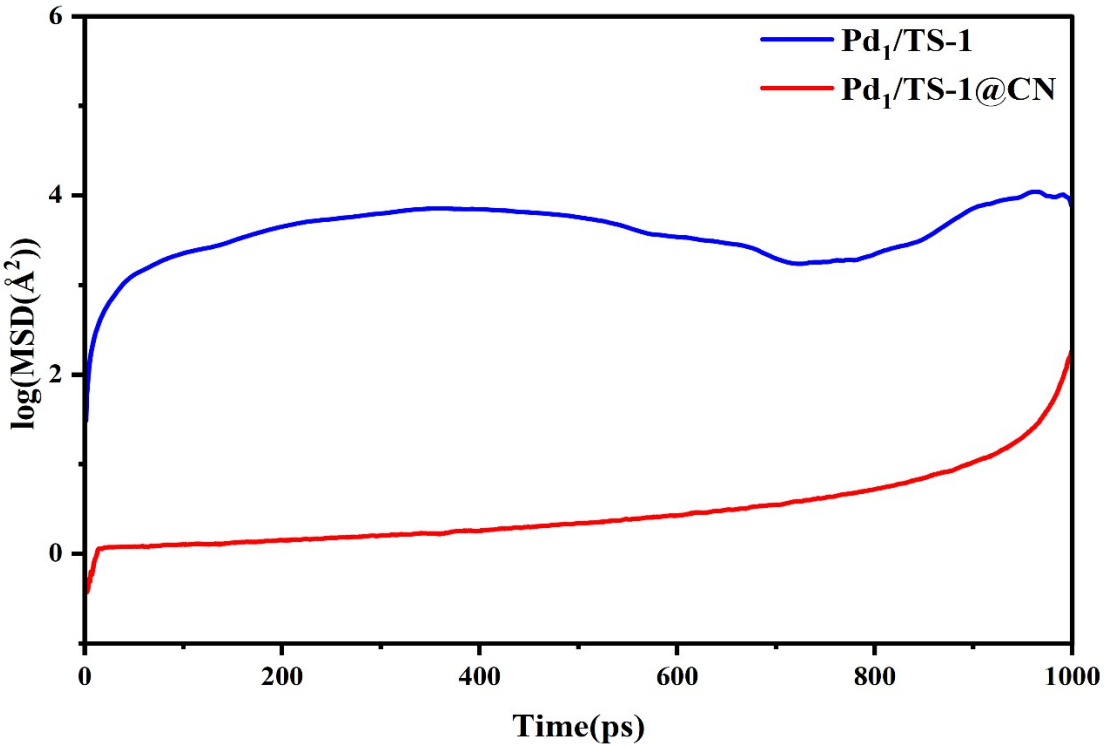

Fig. S23 The mean squared displacement of Pd atom at Pd_1/TS-1 and Pd_1/TS-1@CN.

The stability of Pd_1 center was measured by Mean Squared Displacement (MSD), which is the deviation between the instantaneous position and the initial position of the particle as it evolves over time as follows:

$$MSD(t) = \frac{1}{N}\sum_{i}^{N}\left|r_i(t) - r_i(0)\right|^2 \#(4)$$

The MSD analysis was performed based on the 1 ns molecular dynamics (MD) simulation within the canonical (NVT) ensemble by the Nose-Hoover thermostat method at 15 °C. The COMPASS force field was used. After 1 ns MD, the MSD of the Pd atom on Pd_1/TS-1 is up to 11,000 Å^2, which is remarkably greater than that of Pd_1/TS-1@CN (970 Å^2). The calculation results show that the stability of the Pd single atom coated with ultra-thin N-doped carbon is significantly improved.

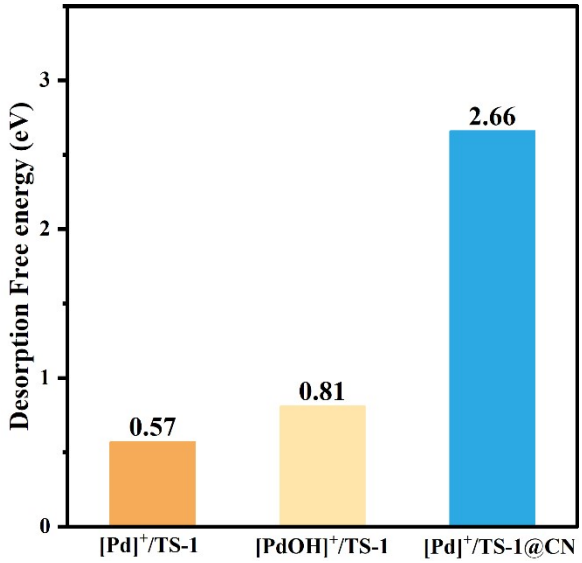

Fig. S24 The desorption energies of active sites $[Pd]^+$/TS-1, $[PdOH]^+$/TS-1, and $[Pd]^+$/TS-1@CN anchored over the ZSM-5 zeolite framework.

The DFT calculations also show that the desorption energy of Pd species away from the TS-1 skeleton is evidently lower than that of $[Pd]^+$/TS-1@CN site (2.66 eV), which indicates that the N_1-Pd_1-O_2 configuration enhances the stability of single atom Pd sites in the pore distribution of TS-1 zeolite.

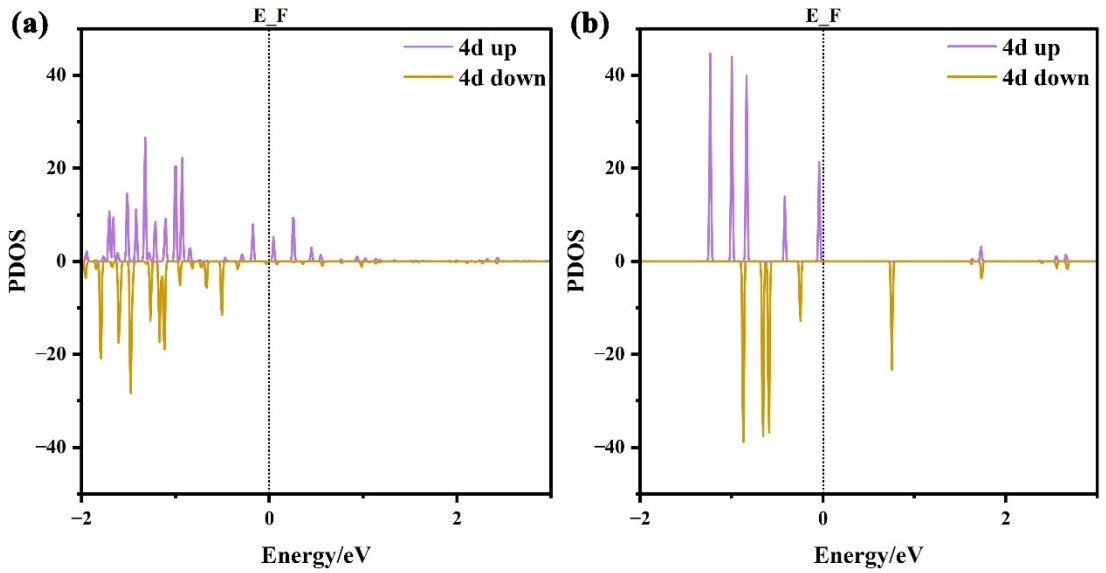

Fig. S25 The PDOS of 4d orbital of Pd atom in Pd_1/TS-1 (a) and Pd_1/TS-1@CN (1:100) (b).

The PDOS analysis of Pd atoms in the active centers of Pd_1/TS-1 and Pd_1/TS-1@CN (1:100) reveal that the PDOS of Pd 4*d* orbital is broadened after coating the ultrathin N-doped carbon layer. Moreover, the change of 4d PDOS around Fermi level suggests that the Pd-N bonding interaction significantly modifies the electronic structure of Pd atoms.

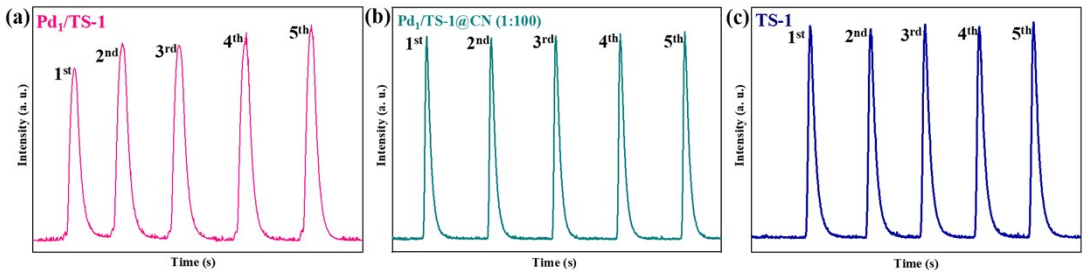

Fig. S26 In-situ H_2 pulse of Pd_1/TS-1 (a), Pd_1/TS-1@CN (1:100) (b), and TS-1 (c). Test temperature: 15 °C; the mass of catalysts is 100 mg; the volume of each pulse of H_2 is 1 ml (42.3 μmol).

The hydrogen consumption is calculated by integrating the residual hydrogen signal after each pulse. All samples used the fifth pulse signal as the reference value and the first four pulse signals as the calculated value to calculate hydrogen consumption. The consumption of H_2 on Pd_1/TS-1@CN (1:100) is 0.107 μmol/g, which is 17.8 times lower than that of Pd_1/TS-1 (1.917 μmol/g) and similar with that of pure TS-1 (0.109 μmol/g) as shown in **Fig. 3d** in the main manuscript.

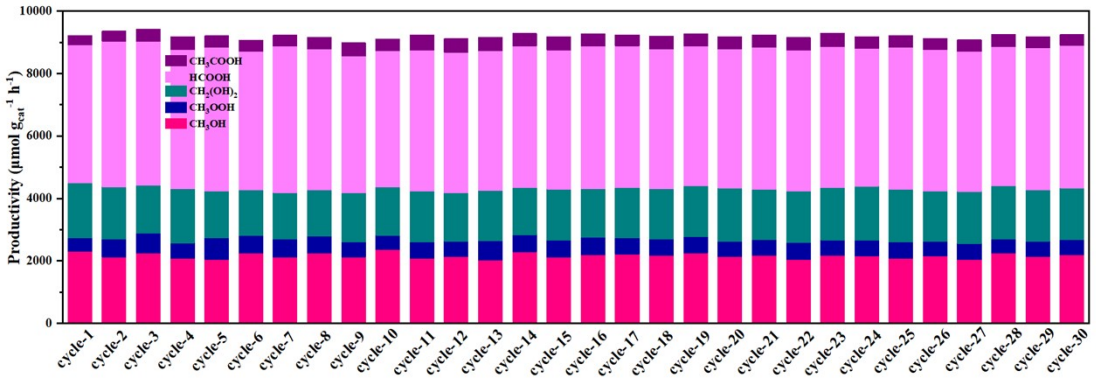

Fig. S27 Reaction cycles of DOM over Pd_1/TS-1@CN (1:100). Reaction Condition: 20 mg catalysts dispersed in 20 ml D. I. H_2O, 15 °C with 28 bar CH_4, 6 bar O_2 and 6 bar H_2 for 1 h.

There is no considerable loss of the catalytic yield (9,204 ± 220 μmol•g_{cat}^{-1}•h^{-1}) even under a higher concentration of H_2 for at least 30 cycles, indicate that the N_1-Pd_1-O_2 site considerably enhances the stability of Pd active sites and correspondingly maintains the excellent catalytic capability of the DOM using molecular oxygen at 15 °C.

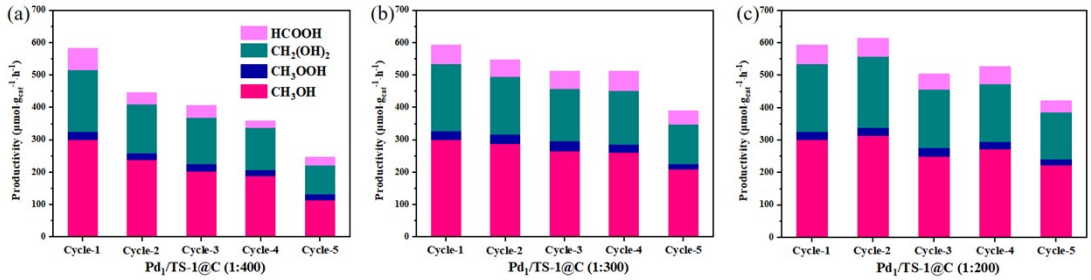

Fig. S28 Reaction cycles of DOM over Pd_1/TS-1@CN (1:400) (a), Pd_1/TS-1@CN (1:300) (b) and Pd_1/TS-1@CN (1:200) (c). Reaction Condition: 20 mg catalysts dispersed in 20 ml D. I. H_2O, 15 °C with 28 bar CH_4, 6 bar O_2, 1.2 bar H_2 and 4.8 bar Ar for 1 h.

By tuning the mass ratio of dopamine to catalyst, the influence of the thickness of N-doped carbon layers on the catalytic performance is investigated. The stability testing results indicate that the over-thin N-doped carbon layers (mass ratio < 1:100) cannot efficiently enhance the stability.

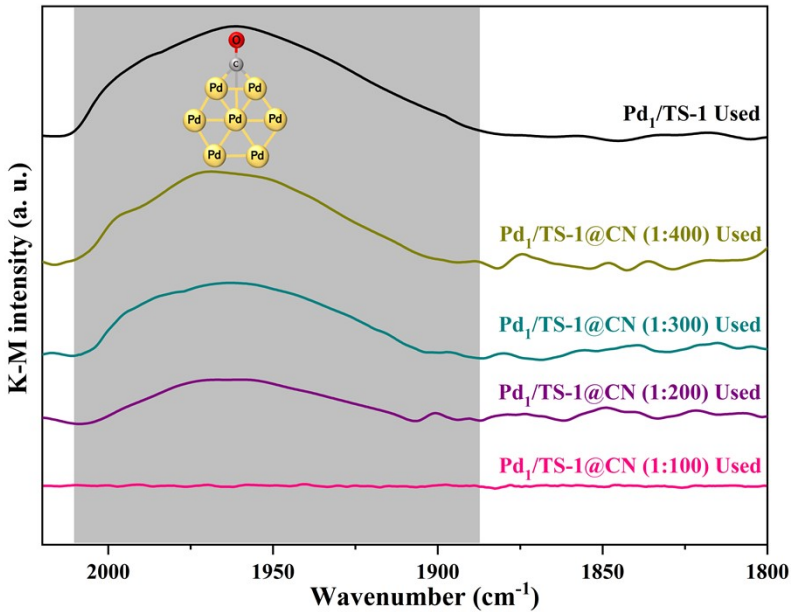

Fig. S29 CO-DRIFTs of the used Pd_1/TS-1@CN catalysts with different mass ratios of dopamine to catalyst after 5 cycles.

For CO-DRIFTs of the used Pd_1/TS-1@CN (1:200, 1:300 and 1:400) and Pd_1/TS-1 catalysts, the presence of bridged CO-adsorption peak centered at 1,960 cm^{-1} indicates that the atomically dispersed Pd species were agglomerated to nanoparticles under the reaction conditions.[25] Alternatively, the absence of any bridged CO-adsorption peak over Pd_1/TS-1@CN (1:100) indicates that the Pd single atoms are still atomically dispersed on the TS-1. Those results confirm that the over-thin N-doped carbon layers cannot efficiently enhance the catalytic stability of atomically dispersed Pd species.

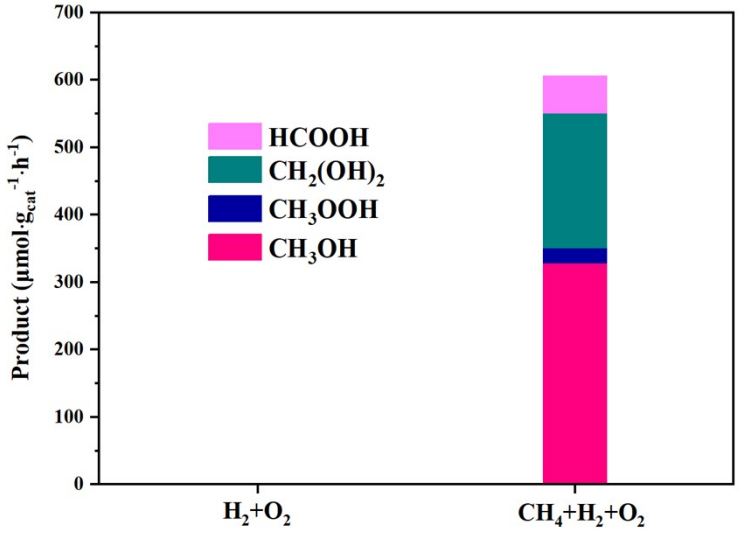

Fig. S30 The comparison experiment of H_2+O_2 and CH_4+H_2+O_2. Reaction Condition (H_2+O_2): 20 mg Pd_1/TS-1@CN (1:100) dispersed in 20 ml D.I. H_2O, 15 °C with 32.8 bar Ar, 6 bar O_2 and 1.2 bar H_2 for 1 h. Reaction Condition (CH_4+H_2+O_2): 20 mg catalysts dispersed in 20 ml D.I. H_2O, 15 °C with 28 bar CH_4, 6 bar O_2, 1.2 bar H_2 and 4.8 bar Ar for 1 h.

No any products of liquid oxygenates are observed in the liquid after DOM when CH_4 is removed from the reaction atmosphere, suggesting that the source of carbon in products such as methanol comes from CH_4 rather than N-doped carbon layers.

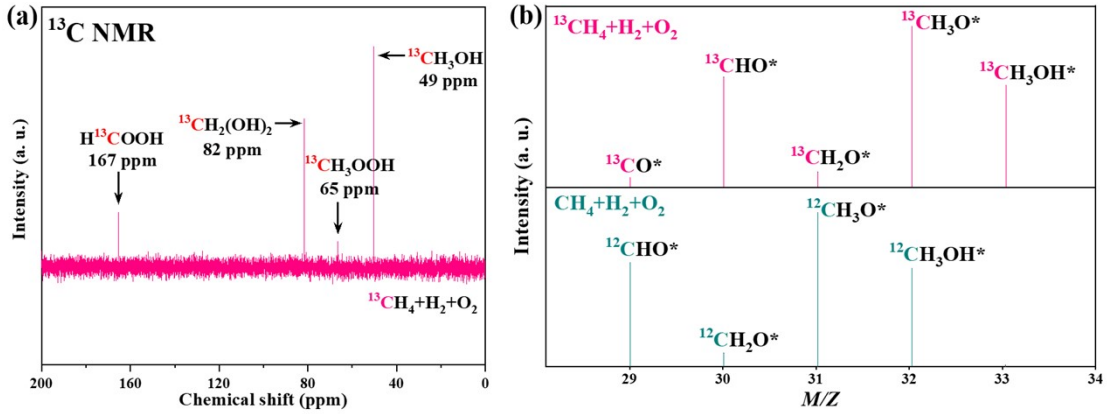

Fig. S31 ^{13}C NMR spectra of the oxygenates produced with $^{13}CH_4 + H_2 + O_2$ + Ar as the feed gas (a) and mass spectrum of the CH_3OH from the conversion of $^{13}CH_4 + H_2 + O_2$ + Ar and $CH_4 + H_2 + O_2$ + Ar (b). Reaction Condition: 20 mg catalysts dispersed in 10 mL D. I. H_2O, 15 ℃ with 2 bar $^{13}CH_4$ or CH_4, 6 bar O_2, 1.2 bar H_2 and 30.8 bar Ar for 2 h.

In order to track the carbon source in the produced oxygenates, the isotopic experiments were conducted by using $^{13}CH_4$ as the feed gas for DOM. As shown in **Fig. 31a**, it can be observed four signals at 49, 65, 82 and 167 ppm in ^{13}C NMR spectrum, which were attributed to $^{13}CH_3OH$, $^{13}CH_3OOH$, $^{13}CH_2(OH)_2$ and $H^{13}COOH$, respectively. It confirms that the oxygenates products indeed originated from CH_4 conversion. In addition, mass spectrum also exhibits that the oxygenated products containing ^{13}C, e.g., $^{13}CH_3OH$ (**Fig. 31b**), can be detected after the DOM when using $^{13}CH_4$ as the carbon source. Those results confirm that the carbon source in the formed oxygenates products are originated from CH_4.

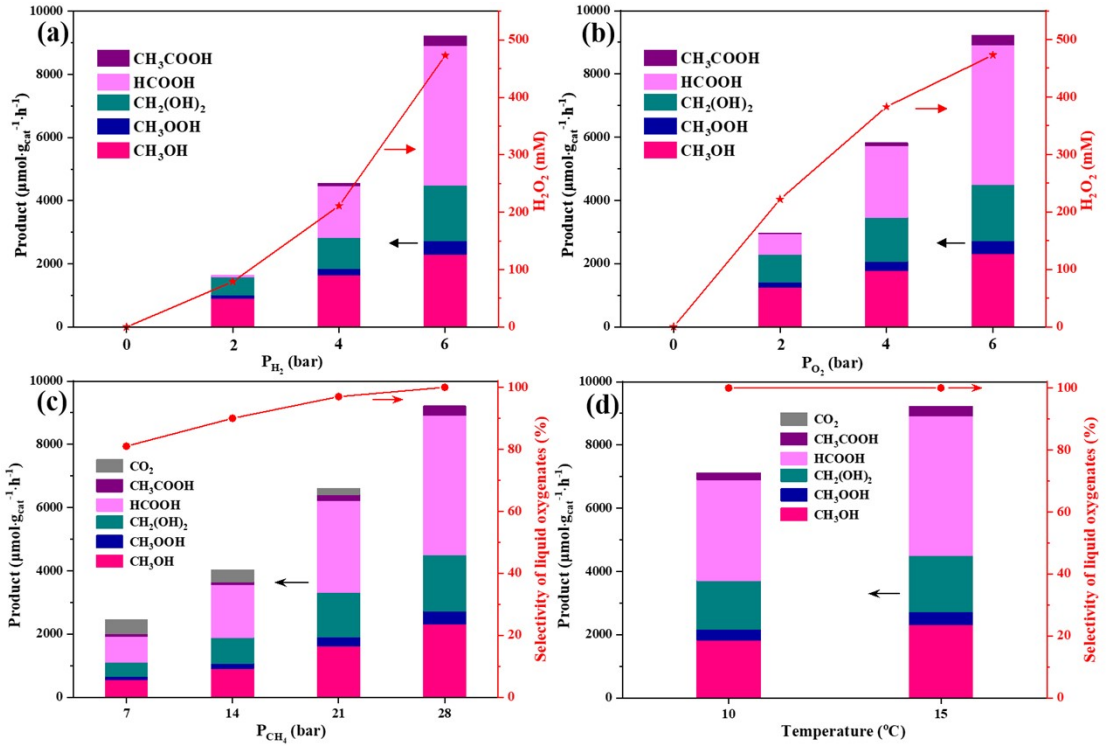

Fig. S32 The influence of reaction condition on DOM over Pd_1/TS-1@CN (1:100). Productivity of Pd_1/TS-1@CN (1:100) for DOM on different H_2 pressure (a); O_2 pressure (b); CH_4 pressure (c) and reaction temperature (d). Reaction Condition (a): 20 mg catalysts, 20 ml H_2O, 15 °C, 6 bar O_2 and 28 bar CH_4 for 1 h. Reaction Condition (b): 20 mg catalysts, 20 ml H_2O, 15 °C, 6 bar H_2 and 28 bar CH_4 for 1 h. Reaction Condition (c): 20 mg catalysts, 20 ml H_2O, 15 °C, 6 bar O_2 and 6 bar H_2 for 1 h. Reaction Condition (d): 20 mg catalysts, 20 ml H_2O, 15 °C, 6 bar H_2, 6 bar O_2 and 28 bar CH_4 for 1 h.

The effect of reaction conditions on activity and selectivity for DOM over Pd_1/TS-1@CN (1:100) has been investigated. First, as the H_2 pressure decreases from 6 to 0 bar, the yield of liquid oxygenates decreases sharply from 9,214 μmol•g_{cat}^{-1}•h^{-1} (6 bar) to 4,556 μmol•g_{cat}^{-1}•h^{-1} (4 bar), 1,643 μmol•g_{cat}^{-1}•h^{-1} (2 bar) and 0 μmol•g_{cat}^{-1}•h^{-1} (0 bar), suggesting that low H_2 pressure would significantly inhibit the conversion of methane to liquid oxygenates. Meanwhile, as the O_2 pressure decreases from 6 to 0 bar, the yield of liquid oxygenates decreases from 9,214 μmol•g_{cat}^{-1}•h^{-1} (6 bar) to 5,824 μmol•g_{cat}^{-1}•h^{-1} (4 bar), 2,966 μmol•g_{cat}^{-1}•h^{-1} (2 bar) and 0 μmol•g_{cat}^{-1}•h^{-1} (0 bar), suggesting that low O_2 pressure would also inhibit the conversion of methane to liquid oxygenates. Interestingly, the yield decrease of liquid oxygenates caused by the decrease of H_2 pressure is more significantly than that of the decrease of O_2 pressure, indicating that the effect of H_2 pressure on DOM is more significant than that of the O_2 pressure. The DFT calculations further reveal the significant discrepancy of H_2 and O_2 partial pressures on the yield of liquid oxygenates. After the O_2 molecules readily adsorb onto the mononuclear Pd site with a free adsorption energy of -1.12 eV, the O_2* is preferentially hydrogenated via a non-Horiuti−Polanyi mechanism, i.e., the direct hydrogenation by the molecular hydrogen to produce HOO* and H* ($[Pd(OOH)(H)]^+$. At this step, the rate-determining step for the formation of active hydroxyl oxygen species is the hydrogenation process (0.91 eV) rather than the oxygen adsorption process (-1.12 eV). Thus, the effect of H_2 pressure causes huge influence for DOM than that of O_2 pressure (details discussed in DFT section, **Fig. 6a** in the main manuscript).

Afterwards, it can be seen that the output and selectivity of liquid oxygenates increases proportionally with the increase of methane pressure, indicating high methane pressure benefits the high yield and selectivity of liquid oxygenates. Moreover, as the reaction temperatures increase from 10 to 25 ^{o}C, the yield of liquid oxygenates enhances from 7,126 to 9,214 $\mu mol \bullet g_{cat}^{-1} \bullet h^{-1}$, suggesting that high temperatures promote the conversion of methane to oxygenates.

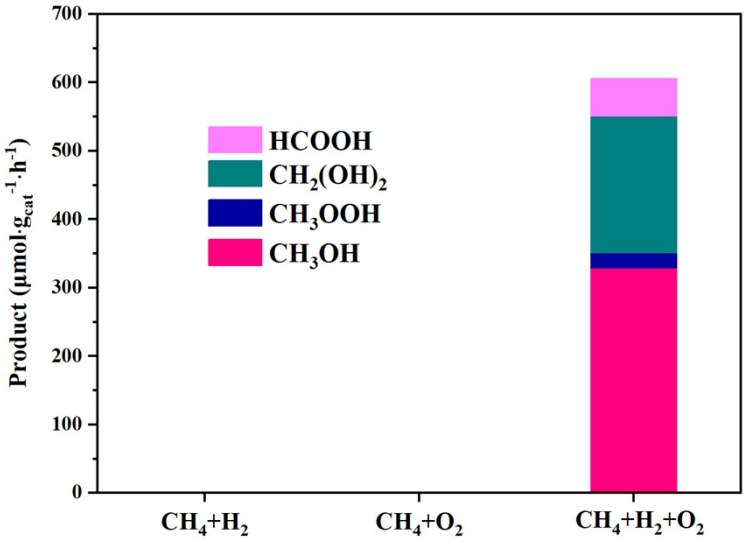

Fig. S33 The comparison experiment of CH_4+H_2 CH_4+O_2 and $CH_4+H_2+O_2$. Reaction Condition (CH_4+H_2): 20 mg Pd_1/TS-1@CN (1:100) dispersed in 20 ml D.I. H_2O, 15 °C with 28 bar CH_4, 10.8 bar Ar and 1.2 bar H_2 for 1 h. Reaction Condition (CH_4+O_2): 20 mg Pd_1/TS-1@CN (1:100) dispersed in 20 ml D.I. H_2O, 15 °C with 28 bar CH_4, 6 bar O_2 and 6 bar Ar for 1 h. Reaction Condition ($CH_4+H_2+O_2$): 20 mg Pd_1/TS-1@CN (1:100) dispersed in 20 ml D.I. H_2O, 15 °C with 28 bar CH_4, 6 bar O_2, 1.2 bar H_2 and 4.8 bar Ar for 1 h.

No any products of liquid oxygenates could be observed in the liquid after DOM when H_2 or O_2 are removed from the reaction atmosphere, suggesting that the source of oxygen in product comes from O_2, and H_2 is an essential auxiliary agent for the production of reactive oxygen species.

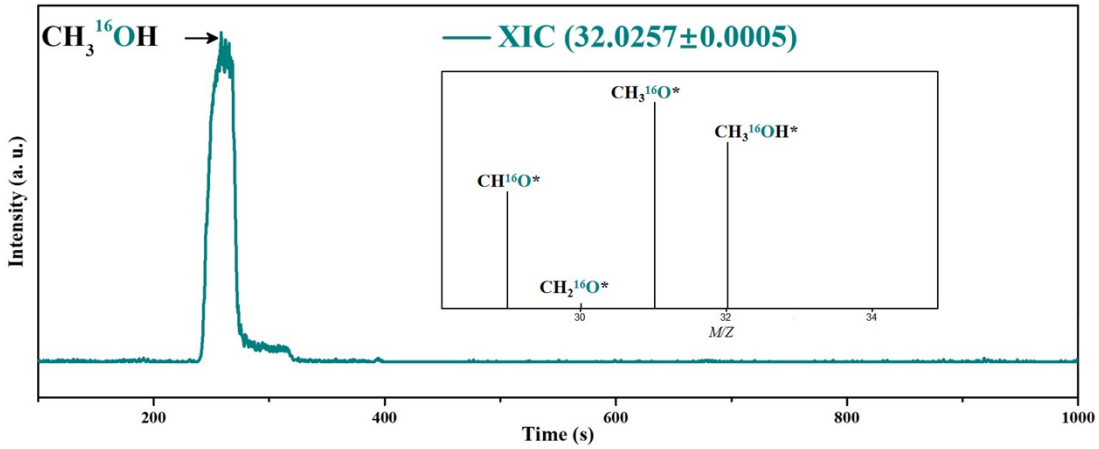

Fig. S34 GC-MS analysis of the raw liquid solution and the corresponding mass spectrum of CH_3OH products by using $^{16}O_2$ and $H_2{}^{18}O$.

GC-MS analysis confirms that only the oxygenated products contained ^{16}O such as CH_3OH can be detected after DOM when using $H_2{}^{18}O$, indicating that oxygen atoms in H_2O do not participate in DOM reaction in our catalyst system.

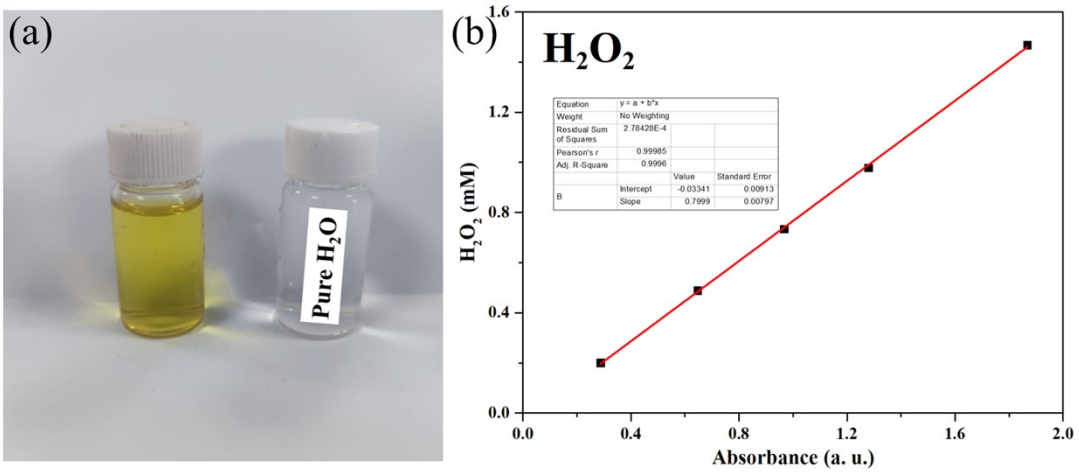

Fig. S35 Concentration of H_2O_2 detected via UV-Vis spectrum (a) and standard curve for H_2O_2 quantification (b). The ordinate (Y) represents the content of H_2O_2 and the abscissa (X) represents the absorbance at 400 nm.

H_2O_2 is observed in the liquid by a potassium titanium oxalate method as reported after the DOM.[38,39] Due to the high concentration of H_2O_2 present in the system, the reaction solution is diluted 40 times with D.I. water in order to achieve the requisite detection range of a standard curve. Then 4 mL solution was taken from the reactor with an injector topped with a 4 μm filter at given time intervals, and then, mixed with 1 mL of 0.02 M potassium titanium (IV) oxalate solution. The solution then changed from transparent to yellow due to the formation of a titanium (IV) - peroxide complex (TiO_2^{2+}) by H_2O_2 and potassium titanium (IV) oxalate. The formation of TiO_2^{2+} is as follows and absorbs with a λ_{max} of about 400 nm. The absorbance at 400 nm was used to determine the concentration of H_2O_2 and monitored by a UV-Vis spectrometer (UV-9010, Pushi Inc, Beijing, China). By reacting with potassium titanium oxalate to develop color, it was detected at a concentration of 49.8±3.3 mM.

$$H_2O_2 + K_2TiO(C_2O_4)_2 \bullet 2H_2O \xrightarrow{H_2SO_4} TiO_2^{2+} \text{ (a yellow titanium (IV) - peroxide complex).} \quad (5)$$

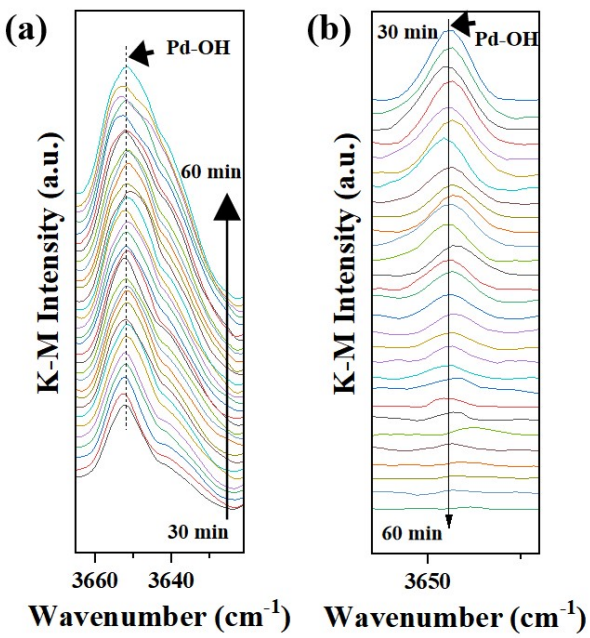

Fig. S36 The peak of Pd–OH species under in-situ H_2+O_2 DRIFTs on Pd_1/TS-1@CN (1:100) after the correction of baseline (a); on Pd_1/TS-1 after the correction of baseline (b).

The concentration of the surface hydroxyl species adsorbed on the isolated Pd sites is estimated by integrating the peak area of the Pd–OH peak. The Pd-OH concentration on Pd_1/TS-1@CN estimated based on integrating the peak area of Pd–OH species constantly increases and stay constant with the reaction time is further extended after 53 min (**Fig. S36a**), while Pd-OH on Pd_1/TS-1 considerably decreases after 18 min (**Fig. S36b**). These results reveal that the stability of surface hydroxyl species on Pd_1/TS-1@CN is considerably higher than that on Pd_1/TS-1.

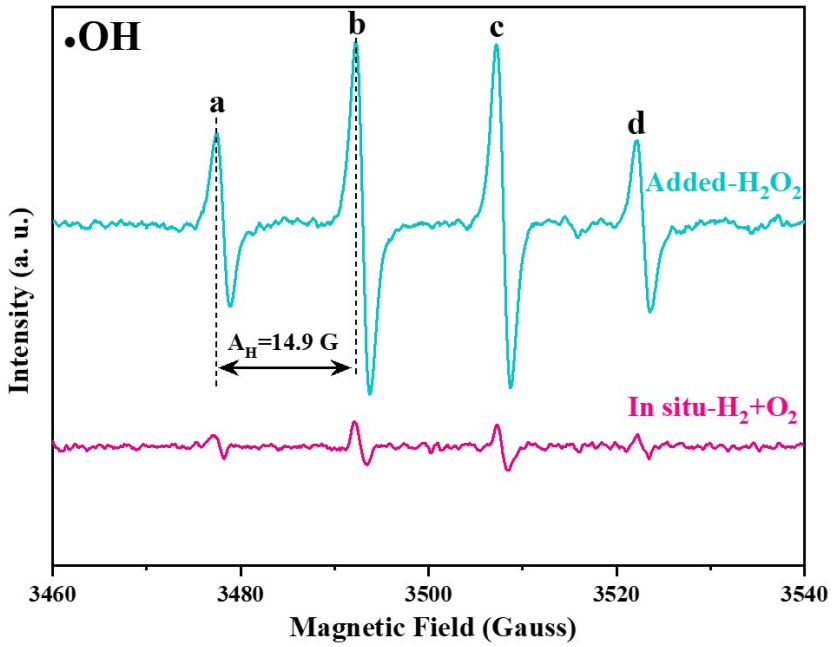

Fig. S37 EPR spectra of hydroxyl radicals trapped by 5, 5'-Dimethyl-1-pyrroline N-oxide (DMPO) of Pd_1/TS-1@CN (1:100) through different atmosphere/oxidant.

As shown in **Fig. S37**, the 1:2:2:1 quartet signals with the hyperfine splitting constants measured as A_H = 14.9 G were clearly observed and attributed to the •OH species.[40] The absence of six prominent characteristic signals with the hyperfine splitting constants measured as A_H = 10.6 G ruled out the presence of •OOH species.[40,41] To identify whether the free hydroxyl radicals (•OH) formed by the dissociation of H_2O_2 in the reaction medium are the active oxygen species for DOM, the electron paramagnetic resonance (EPR) spectra are conducted. By calculating the total integral area of the quadruple splitting peak of EPR, the concentration of •OH when H_2O_2 is used as oxidant is estimated ~43 times higher than that using H_2 and O_2.

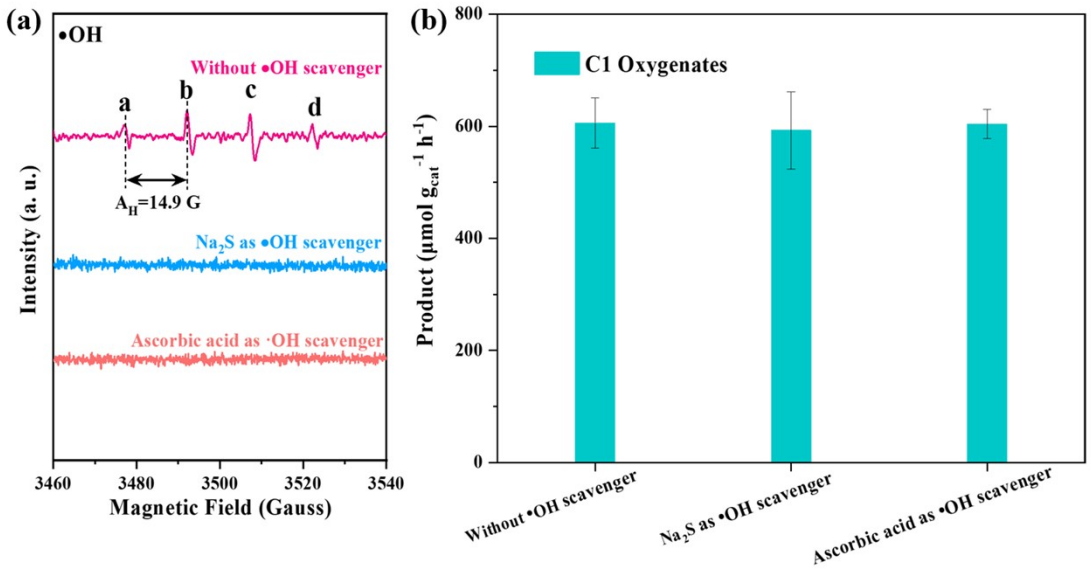

Fig. S38 EPR spectra of hydroxyl radicals trapped by 5, 5'-Dimethyl-1-pyrroline N-oxide (DMPO) of Pd_1/TS-1@CN (1:100) through different conditions (a) and comparison experiments of the yield of liquid oxygenates for addition of •OH scavenger and without •OH scavenger (b).

To identify whether the free hydroxyl radicals (•OH) is the reactive oxygen species for the DOM in our reaction system, Na_2S and ascorbic acid were added to conduct quenching experiments of free •OH for DOM.[42] Before adding the free •OH scavengers in the solution, the 1:2:2:1 quartet signals with the hyperfine splitting constants measured as A_H = 14.9 G were clearly observed, which is attributed to the free •OH species.[40] After adding the free •OH scavengers, there are no aforementioned signals associated with the free •OH, which indicates that free •OH is quenched.

However, the yield of the C1 liquid oxygenates products after adding Na_2S (598 ± 68.9 μmol•g_{cat}^{-1}•h^{-1}) and ascorbic acid (604 ± 26.1 μmol•g_{cat}^{-1}•h^{-1}) as the free •OH scavenger is similar to that without adding the free •OH scavenger (606 ± 44.6 μmol•g_{cat}^{-1}•h^{-1}). These results indicate that the free •OH species existing in the solution are not the reactive oxygen species for the DOM.

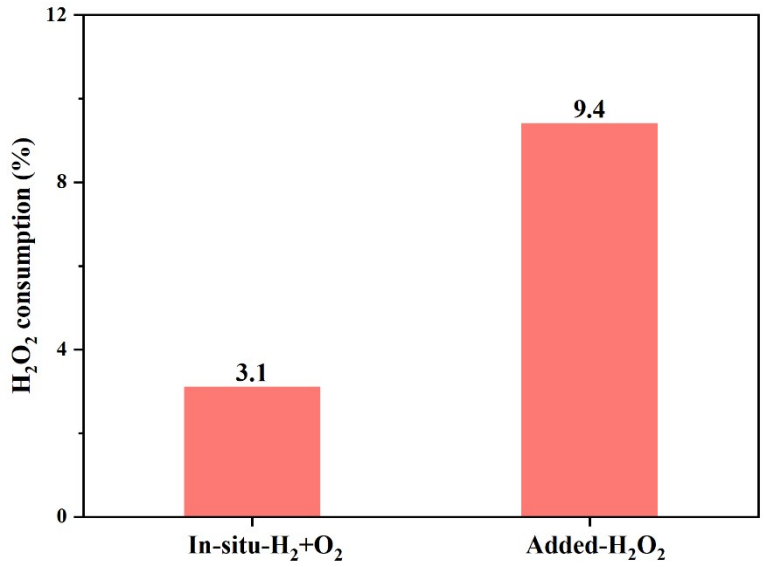

Fig. S39 The consumption for externally added H_2O_2 and in-situ H_2+O_2.

The consumption of externally added H_2O_2 is ~3 times higher than that of the in-situ produced reactive oxygen species by H_2 and O_2, which further indicates that externally added H_2O_2 is easy to self-decompose at the active site rather than to activate methane.

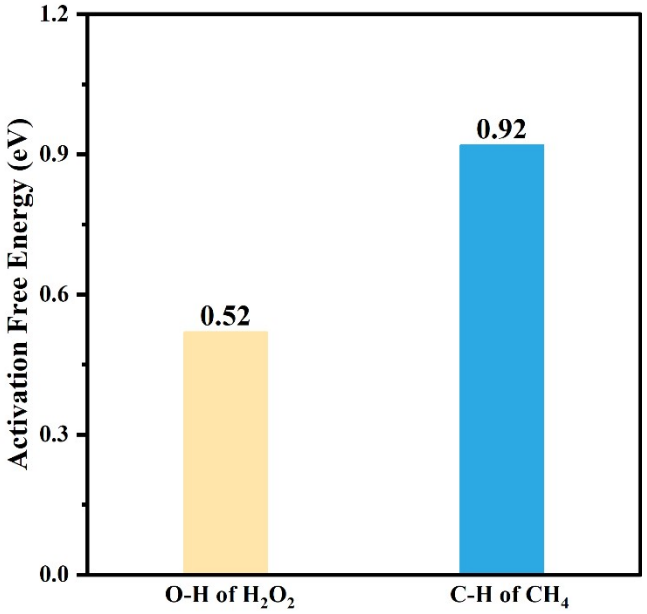

Fig. S40 The comparison on the bond activation energy of C-H and O-H bond for DOM over Pd_1/TS-1@CN (1:100).

The DFT calculation reveals that although methane could be intrinsically activated at active sites $[Pd(OH)_2]^+$/TS-1@C by using H_2O_2 as oxidant, regarding the limited number of active sites, the competition reaction between methane and hydrogen peroxide oxidation must exist. DFT calculations show that the C-H bond activation free energy barrier (G_a = 0.92 eV) of CH_4 is much higher than the O-H bond activation free energy barrier (G_a = 0.52 eV) of H_2O_2 at the active site, indicating the self-decomposition process of H_2O_2 at the active site is easy.

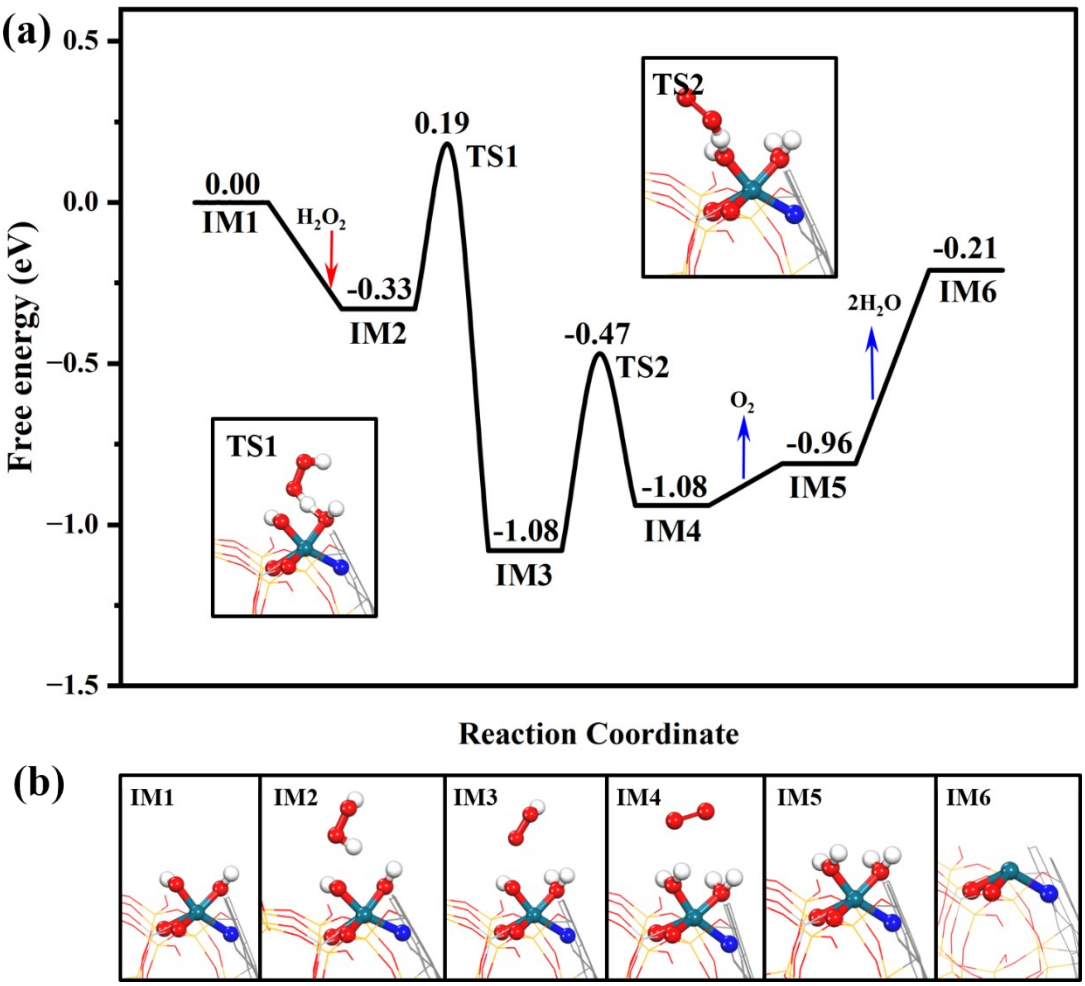

Fig. S41 Gibbs free energy profiles of hydrogen peroxide oxidation at $[Pd(OH)_2]^+$/TS-1@CN site at 288 K (a) with the geometry structures of the corresponding transition states and intermediate states (b).

The hydrogen bonding enables to stick the H_2O_2 molecule on $[Pd(OH)_2]^+$/TS-1@CN (IM2) with the adsorption energy of -0.33 eV. The hydrogen atom could be readily abstracted from H_2O_2 by the •OH* at $[Pd(OH)_2]^+$/TS-1@CN to generate •OOH and $[Pd(OH)(H_2O)]^+$/TS-1@CN (IM3) via a radical-like mechanism, which only needs to overcome a free energy barrier of 0.52 eV (TS1). It requires a free energy barrier of 0.61 eV (TS2) for the subsequent oxidative dehydrogenation of •OOH to produce O_2. Finally, the $[Pd]^+$/TS-1@CN is regenerated after the desorption of H_2O. Those results confirm that the self-decomposition of H_2O_2 would easily occur rather than to form stable reactive oxygen species for DOM when the H_2O_2 is directly used as oxidant.

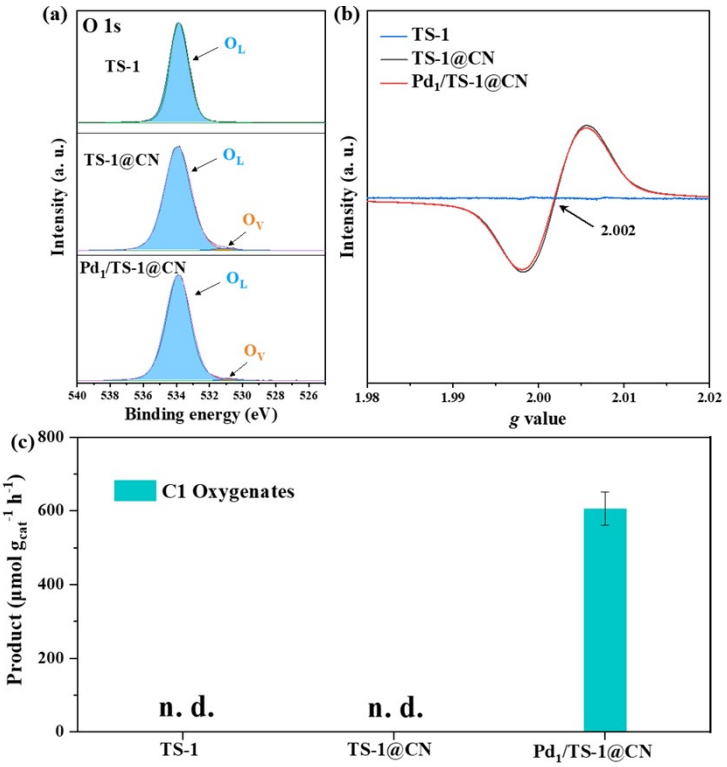

Fig. S42 The impact of vacancies on DOM. XPS of O 1s for TS-1, TS-1@CN and Pd1/TS-1@CN (a); The electron paramagnetic resonance of TS-1, TS-1@CN and Pd1/TS-1@CN (b) and the yield of liquid oxygenates over TS-1, TS-1@CN and Pd1/TS-1@CN (c).

To explore the oxygen vacancies in Pd_1/TS-1@CN catalyst, the XPS of O 1s for TS-1, TS-1@CN and Pd_1/TS-1@CN were conducted analyzed. As shown in **Fig. S42a**, only one peak at 533.8 eV associated with the lattice oxygen is observed but the peak at around 531.0 eV associated with the oxygen vacancies is barely observed on the TS-1[43], which indicates that the oxygen vacancies is barely present in TS-1. Our DFT simulation results also confirm the above experimental result that the formation energy of oxygen vacancy in TS-1 is 5.98 eV, which suggests it is difficult to form oxygen vacancies in TS-1[44]. Similarly, the XPS results for TS-1@CN and Pd_1/TS-1@CN show that the peaks at 531.0 eV associated with the chemisorbed oxygen species at oxygen vacancies are negligible[44,45], which also suggests the oxygen vacancies are barely present in TS-1@CN and Pd_1/TS-1@CN samples.

Alternatively, our electron paramagnetic resonance (EPR) results confirm that there are significant carbon vacancies. The significant ERP signal (g=2.002) associated with the unpaired electron on the carbon atoms of the aromatic rings within Π-bonded nanosheets [26] confirms the presence of more vacancies in both TS-1@CN and Pd_1/TS-1@CN compared with that in TS-1 (**Fig. S42b**). Therefore, for the specific Pd_1/TS-1@CN catalyst, the vacancies are mainly originated from the carbon defects rather than the oxygen vacancies.

To identify the impact of the carbon defects on the direct oxidation of methane (DOM), the DOM was conducted on TS-1 and TS-1@CN but the liquid oxygenates were not detected (**Fig. S42c**), which suggests the carbon defects in TS-1@CN do not activate CH_4. However, the yield of liquid oxygenates on the Pd_1/TS-1@CN is as high as 606 ± 44.6 $\mu mol \cdot g_{cat}^{-1} \cdot h^{-1}$. These results indicate that the carbon vacancies do not play a dominant role in DOM.

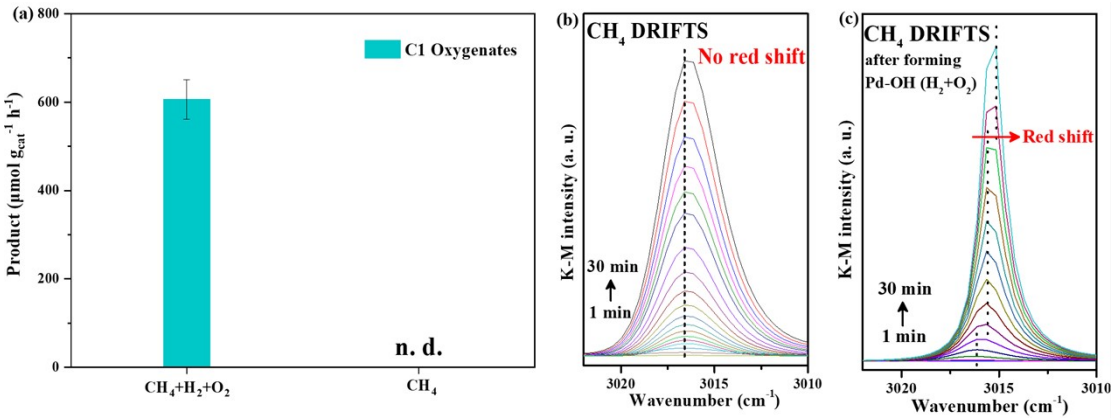

Fig. S43 The impact of Pd_1 active sites and surface hydroxyl groups on oxidation of methane. The yield of liquid oxygenates on Pd_1 active sites and surface hydroxyl groups (a); the in-situ CH_4-DRIFTs of the partial enlarged view of ν_{C-H} region without H_2 and O_2 co-adsorption on Pd_1/TS-1@CN (1:100) (b) and after H_2 and O_2 co-adsorption on Pd_1/TS-1@CN (1:100) (c).

In addition, to identify the impact of the Pd_1 active sites and surface hydroxyl groups on the DOM, the DOM reaction of CH_4+H_2+O_2 and sole CH_4 over Pd_1/TS-1@CN (1:100) was conducted. The DOM reaction of CH_4+H_2+O_2 over Pd_1/TS-1@CN (1:100) was to identify the impact of surface hydroxyl groups formed by H_2+O_2 Pd_1/TS-1@CN (1:100) while sole CH_4 over Pd_1/TS-1@CN (1:100) was to identify the impact of Pd_1 active sites. As shown in **Fig. S43a**, the liquid oxygenates of sole CH_4 over Pd_1/TS-1@CN (1:100) were not detected, suggesting that the Pd_1 active sites do not play a dominant role in generating the surface active oxygen species to drive the DOM. Moreover, to further verify the origin of reactive oxygen species for the DOM, in-situ FT-IR was probed. For the in-situ CH_4-DRIFTs on Pd_1/TS-1@CN (1:100) (**Fig. S43b**), when only CH_4 is introduced without H_2 and O_2, the C-H bond stretching vibration peak of methane exhibits no redshift. When CH_4 was introduced after the co-adsorption of H_2 and O_2 (**Fig. S43c**), the peak of the C-H stretch vibration of methane is gradually redshifted from 3,017 to 3,015 cm^{-1}. These results indicate that the C-H bond of CH_4 is activated by the surface hydroxyl species on Pd sites rather than the Pd_1 sites during the DOM.

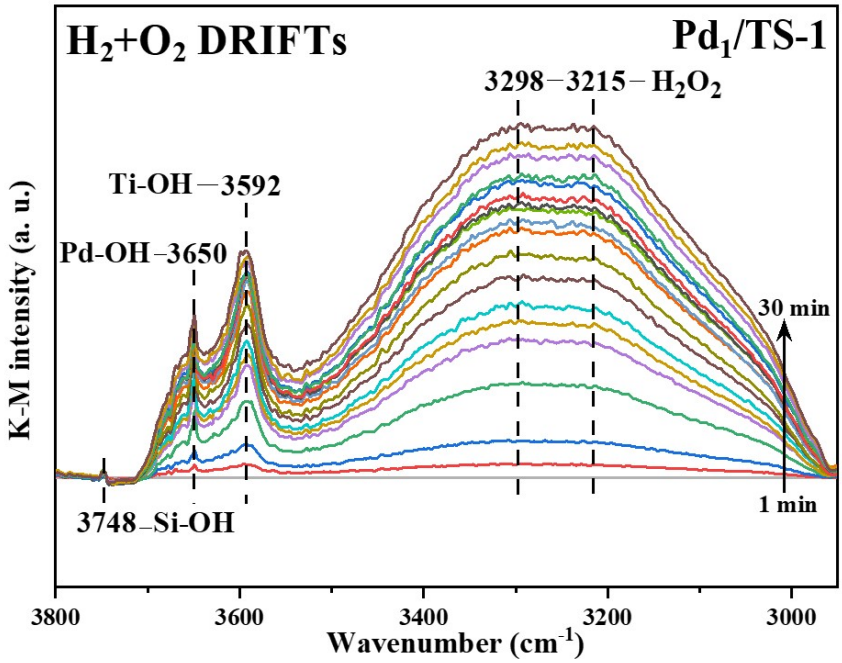

Fig. S44 The in-situ H_2+O_2 DRIFTs on Pd_1/TS-1.

For H_2 and O_2 DRIFTs on Pd_1/TS-1, the surface hydroxyl species adsorbed on isolated Pd sites are also observed[28, 46-48], which indicates that the H_2 and O_2 form reactive oxygen species and explains the excellent initial catalytic activity.

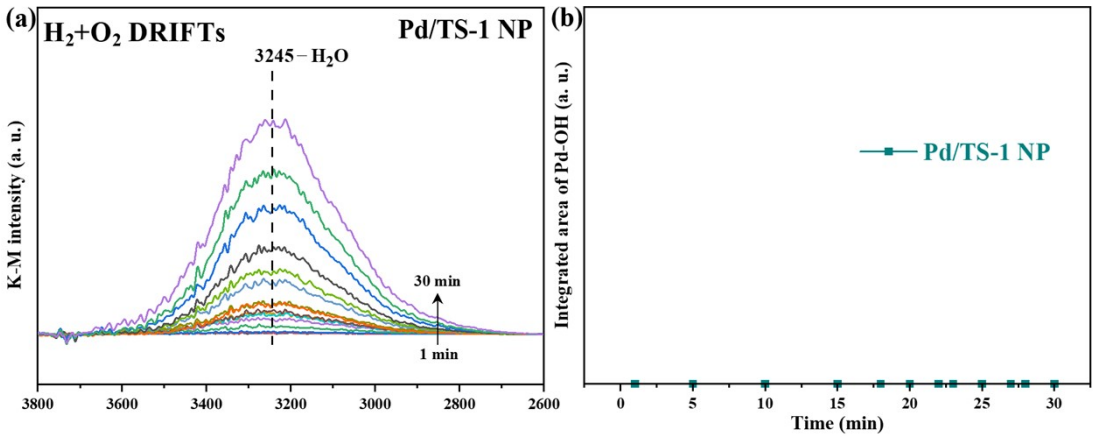

Fig. S45 The in-situ H_2+O_2 DRIFTs on Pd/TS-1 NP (a) and the integrated area of Pd-OH (b).

For H_2 and O_2 DRIFTs on Pd/TS-1 NP as shown in **Fig. S45a**, only H_2O peak cantered at 3,245 cm^{-1} can be observed[49,50], and the surface hydroxyl species adsorbed on Pd particles are barely observed. The integrated IR absorbance of a particular vibrational mode is well known to be proportional to the number of adsorbed species and can thus be used as a quantitative measure for the reaction progress.[51,52] Hence, the concentration of surface hydroxyl species adsorbed on Pd sites is estimated by integrating the peak area of Pd-OH peak. The concentration of surface hydroxyl species is estimated to be zero as shown in **Fig. S45b**, which explains the poor initial catalytic activity for DOM.

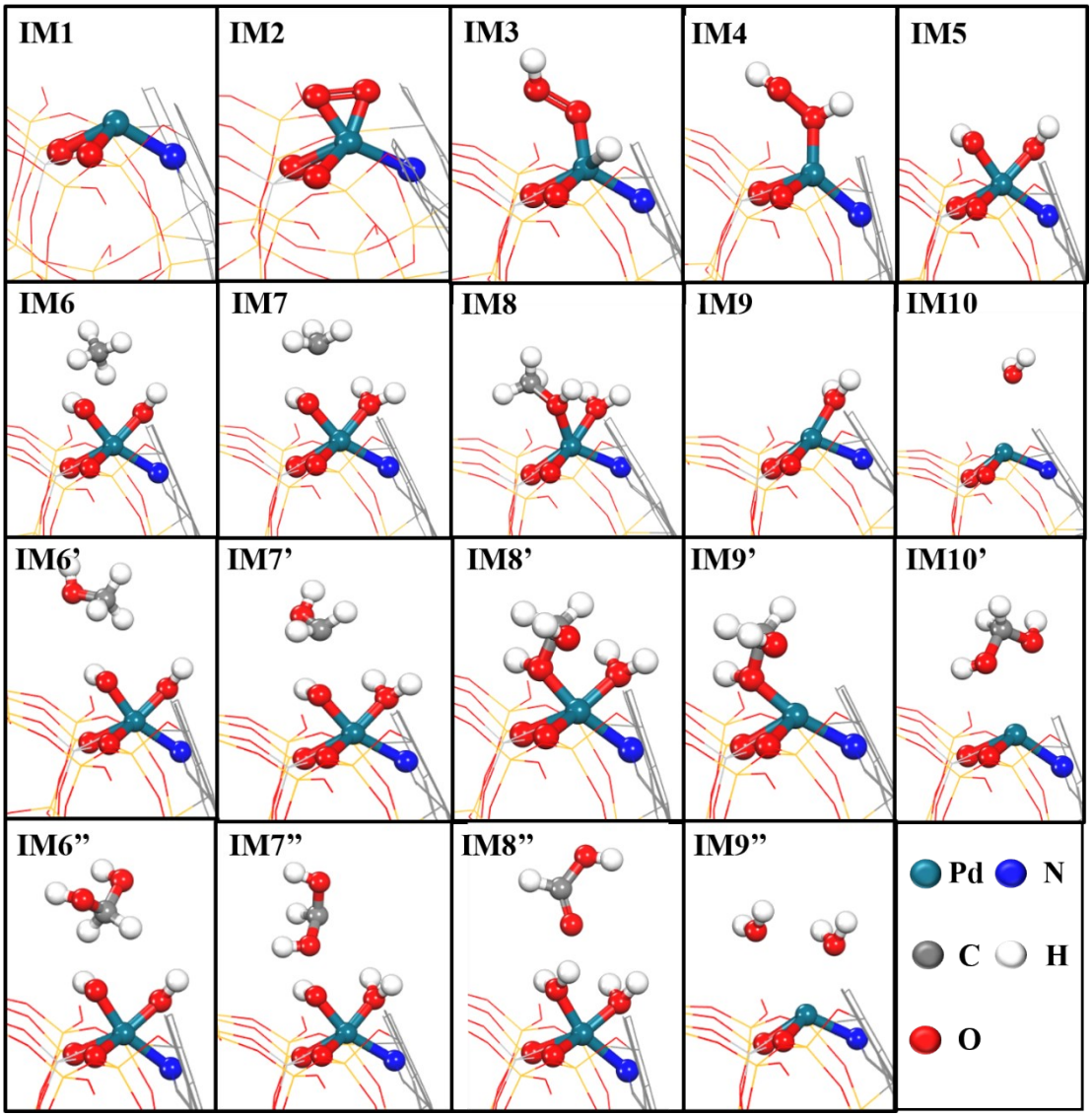

Fig. S46 Reaction pathways for methane activation on the Pd_1/TS-1@CN.

Fig. S46 presents the models for key intermediate species confined in the channels of the Pd_1/TS-1@CN.

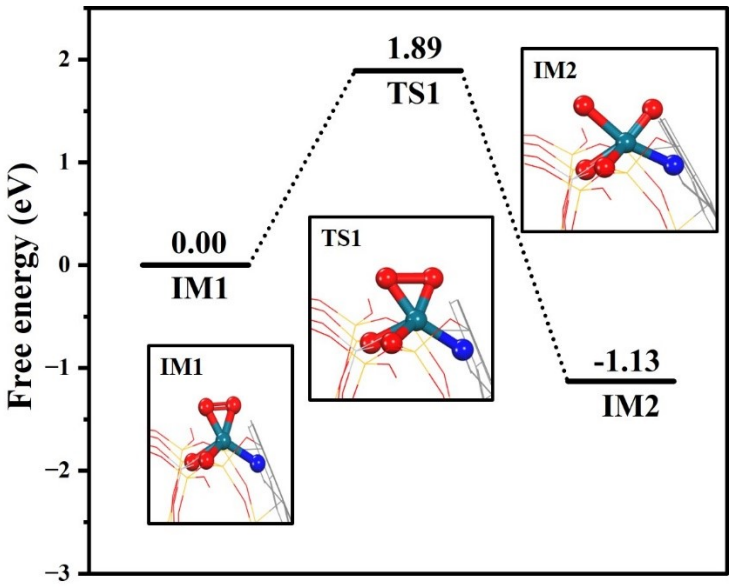

Fig. S47 Gibbs free energy profiles of oxygen activation at $[Pd]^+$/TS-1@CN site at 288 K with the geometry structures of the corresponding transition states and intermediate states.

Initially, an O_2 molecule can readily adsorb onto the mononuclear Pd site, generating the $[PdO_2]^+$ (IM1) site with a strong free adsorption energy of -1.13 eV. The O-O bond of O_2 is strengthened to 1.34 Å, implying the formation of superoxide.[53] However, it is formidable for O_2 to capture more electrons from Pd atom to boost O-O bond activation to generate O_2^{2-}* or assist the O-O bond breaking towards the generation of O^{2-}*. The O-O bond activation of O_2 at the $[PdO_2]^+$ site requires overcoming a free energy barrier of 1.89 eV. Therefore, it is necessary to introduce H_2 to assist oxygen activation, which is consistent with the experimental results.

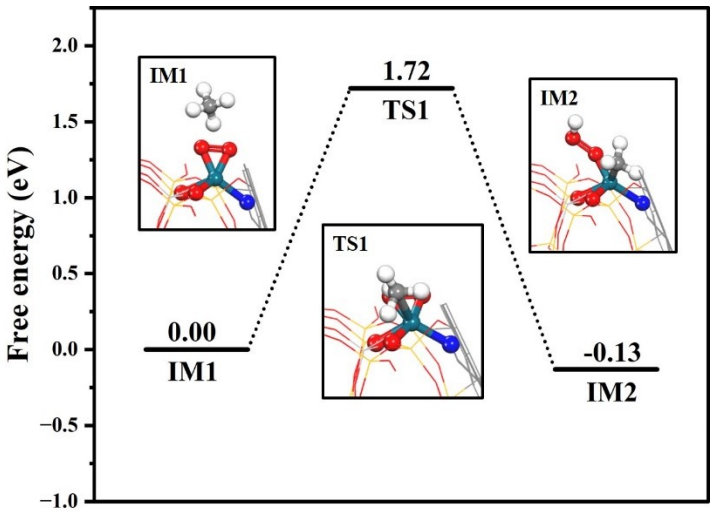

Fig. S48 Gibbs free energy profiles of direct activation of methane by oxygen at $[PdO_2]^+$/TS-1@CN site at 288 K with the geometry structures of the corresponding transition states and intermediate states.

Initially, an O_2 molecule can readily adsorb onto the mononuclear Pd site, generating the $[PdO_2]^+$ (IM1) site with the formation of superoxide. The direct activation of methane by O_2* as an active oxygen species is difficult and needs to be overcome a free energy barrier of 1.72 eV, which is consistent with the experimental results.

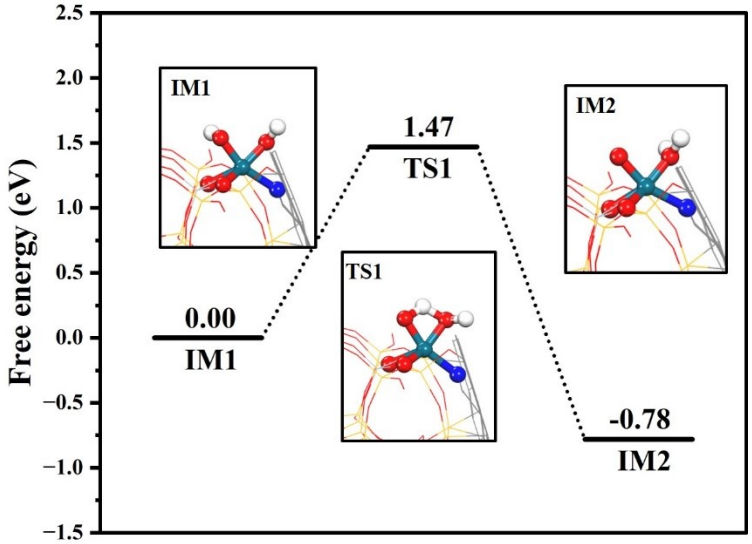

Fig. S49 Gibbs free energy profiles of hydrogen migration of hydroxyl groups at $[Pd(OH)_2]^+$/TS-1@CN site at 288 K with the geometry structures of the corresponding transition states and intermediate states.

After the pre-activation of the reaction site generated $[Pd(OH)_2]^+$ site, then two OH* on Pd atoms are stable and the H migration between the hydroxyl groups is difficult, which needs to overcome a free energy barrier of 1.47 eV.

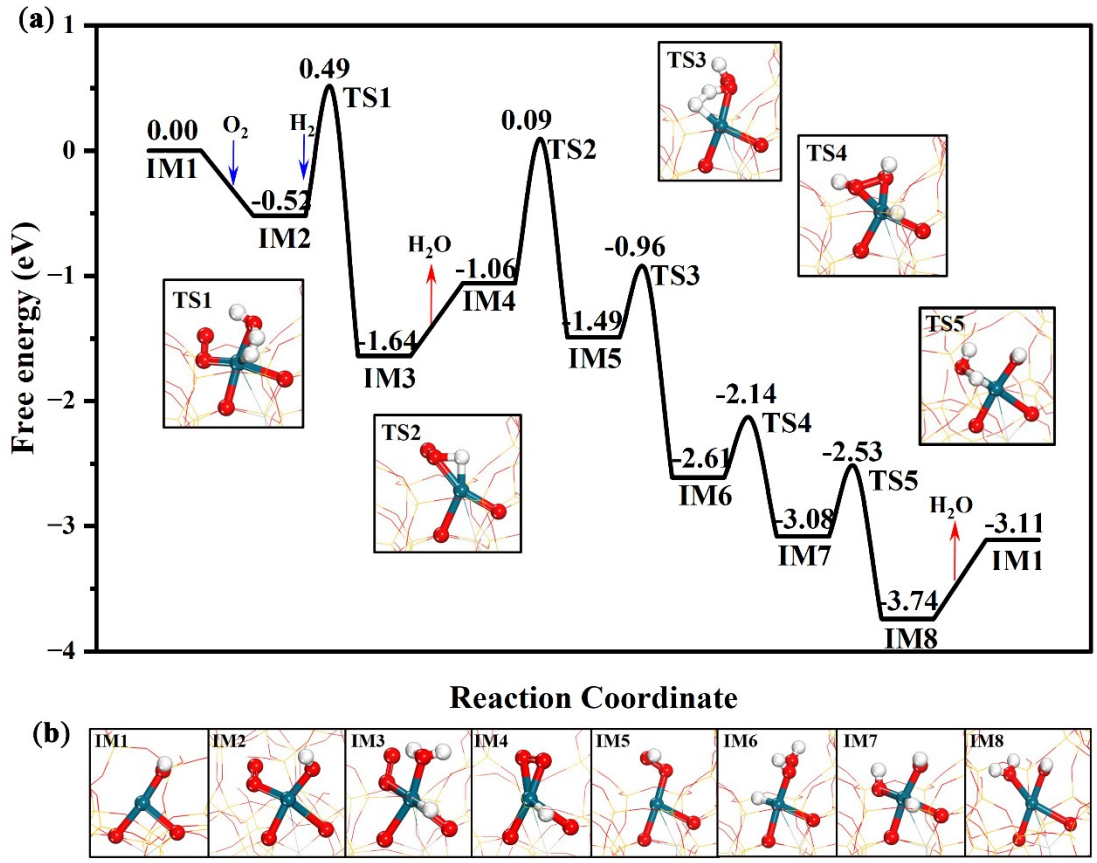

Fig. S50 Gibbs free energy profiles of H_2 and O_2 activation at $[PdOH]^+$/TS-1 site at 288 K with the geometry structures of the corresponding transition states (a) and intermediate states (b).

Oxygen adsorbs on the Pd atom of $[PdOH]^+$, forming $[PdOH(O_2)]^+$ (IM2) with an adsorption energy of -0.52 eV. The OH* at $[PdOH(O_2)]^+$ readily abstracts the hydrogen atom from H_2, resulting in $[PdH(O_2)(H_2O)]^+$ (IM3), which requires overcoming a free energy barrier of 1.01 eV (TS1). The desorption of H_2O is an endothermic process with an energy requirement of 0.58 eV. Facilitating hydrogen transfer in $[PdH(O_2)]^+$ (IM4) to produce OOH* requires overcoming a free energy barrier of 1.15 eV (TS2). H_2 dissociates at the $[PdOOH]^+$ (IM5) site, requiring overcoming a 0.53 eV free energy barrier, resulting in $[PdH(H_2O_2)]^+$ (IM6) formation. Finally, the dissociation of the O-O bond in H_2O_2 requires overcoming a 0.47 eV energy barrier, generating OH* at the $[PdH(OH)_2]^+$ (IM7) site. Although the OH* adsorbed on Pd can activate methane, the H adsorbed on Pd is easier to migrate to OH*, only requiring overcome a 0.55 eV free energy barrier (TS5). The desorption energy of H_2O is 0.63 eV.

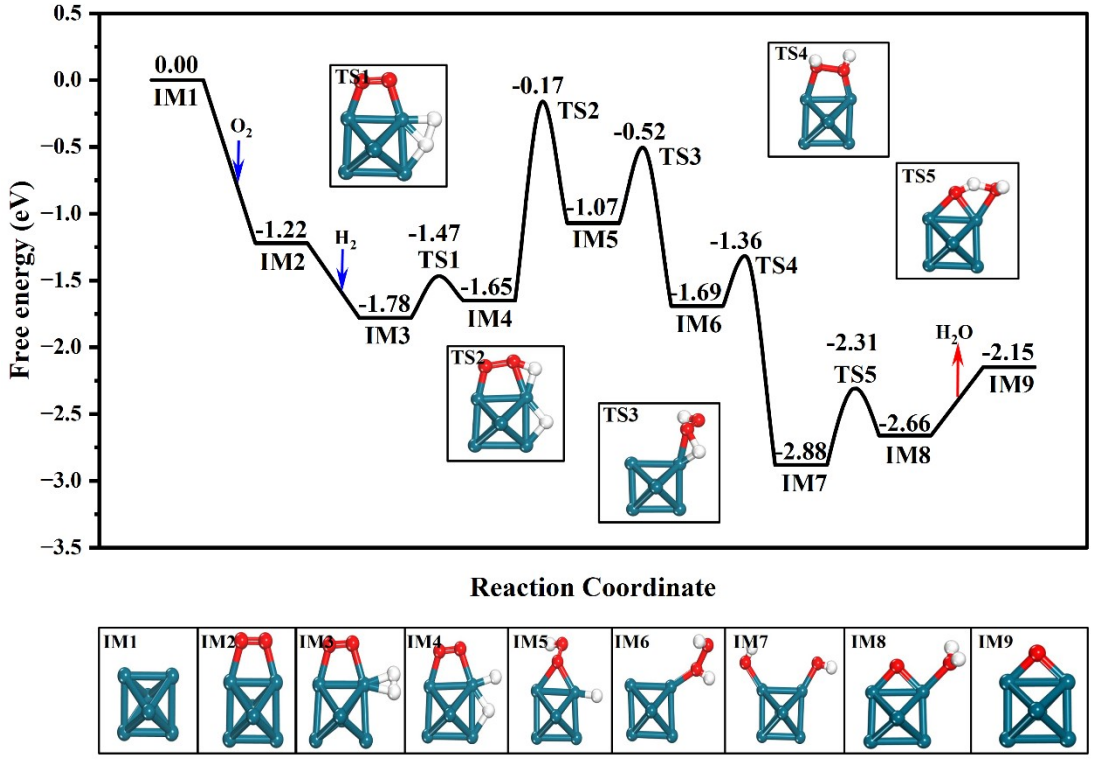

Fig. S51 Gibbs free energy profiles of H_2 and O_2 activation at Pd-cluster site at 288 K with the geometry structures of the corresponding transition states (a) and intermediate states (b).

Oxygen adsorbs onto the Pd atom, forming an intermediate (IM2) with a binding energy of -1.22 eV. Subsequently, H_2 adsorbs onto the Pd atom, resulting in an intermediate (IM3) with a binding energy of -0.56 eV. H_2 readily dissociates, leading to the formation of H atoms on the Pd-cluster surface, requiring overcoming a free energy barrier of 0.31 eV (TS1). The migration of the H atom to O_2 necessitates overcoming a free energy barrier of 1.48 eV (TS2), resulting in OOH* formation. The subsequent hydrogenation of OOH* to H_2O_2* requires overcoming a free energy barrier of 0.55 eV (TS3). Favorably, H_2O_2 could easily be dissociated to 2OH* with a free energy barrier of 0.33 eV (TS4). Importantly, the facile proton transfer (G_a = 0.51 eV, TS5) enables the elimination of the OH*.

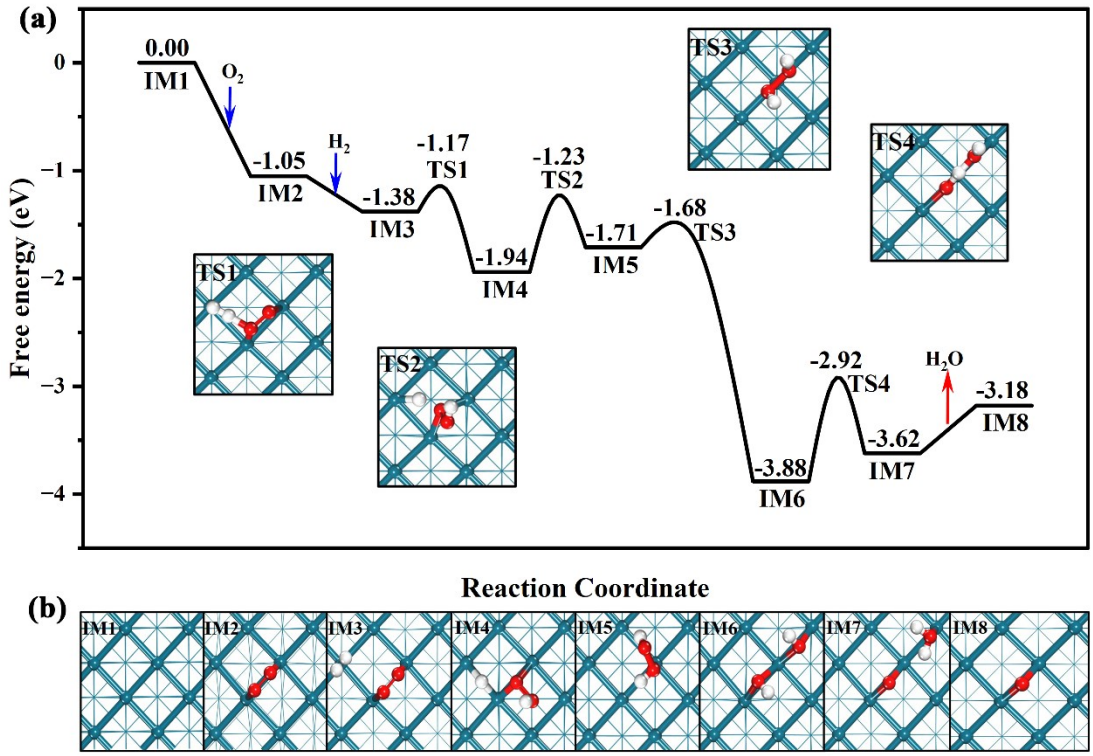

Fig. S52 Gibbs free energy profiles of H_2 and O_2 activation at Pd(111) surface at 288 K with the geometry structures of the corresponding transition states (a) and intermediate states (b).

Oxygen adsorbs onto the Pd atom, forming an intermediate (IM2) with a binding energy of -1.05 eV. Subsequently, H_2 adsorbs onto the Pd atom, resulting in an intermediate (IM3) with a binding energy of -0.33 eV. Then, the dehydrogenation of H_2 to O_2 only needs to overcome the 0.21 eV free energy barrier (TS1), resulting in OOH*(IM4) formation. The subsequent hydrogenation of OOH* to H_2O_2* requires overcoming a free energy barrier of 0.71 eV (TS2). The H_2O_2* could be readily dissociated into 2OH* with a negligible free energy barrier of 0.03 eV (TS3). It is possible to convert two OH* to O* and H_2O, which needs to overcome a free energy barrier of 0.96 eV (TS4).

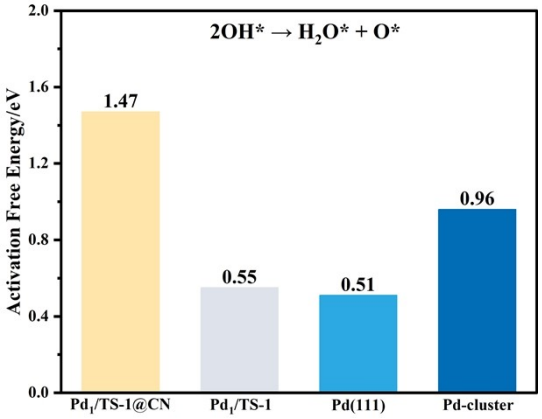

Fig. S53 The free energy barrier of H migration between two hydroxyl groups on Pd_1/TS-1@CN, Pd_1/TS-1, Pd (111) surface, and Pd-cluster.

The free energy barrier of H migration between two hydroxyl groups to form H_2O on single Pd site of Pd_1/TS-1@CN, Pd_1/TS-1, Pd (111) surface and Pd-cluster is further calculated. The free energy barrier of two surface adsorbed hydroxyl species coupling into H_2O* and O* on the Pd_1/TS-1 (0.55 eV), Pd cluster (0.96 eV), and the Pd (111) surface (0.51 eV) is much lower than that on Pd_1/TS-1@CN (1.47 eV). Those results indicate that the formed surface adsorbed hydroxyl species enable to stably adsorb on Pd_1/TS-1@CN.

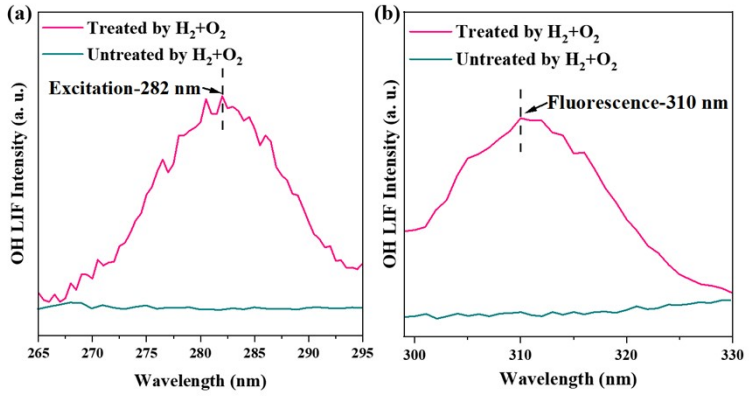

Fig. S54 The laser-induced-fluorescence spectra of •OH* species on Pd_1/TS-1@CN (1:100). Excitation at 282 nm (a) and Fluorescence detected at 310 nm (b).

It has been reported that the •OH* radicals on catalyst surface can be excited by the $A^2\Sigma^+(\nu'=1)\leftarrow X^2\Pi(\nu=0)$ transition at around 282 nm, and the fluorescence of the $A^2\Sigma^+(\nu'=1)\rightarrow X^2\Pi(\nu''=1)$ transition at around 310 nm can be collected.[54,55] Therefore, the laser-induced fluorescence (LIF) spectra were used to detect the surface •OH* species. As shown in **Fig. S54**, the surface •OH^* species were clearly detected from the Pd_1/TS-1@CN surface after the treatment of H_2+O_2 by the LIF spectra on the A-X transition of •OH*. The signals at 282 nm and 310 nm associated with the excitation and fluorescence of surface •OH* can be clearly observed. Alternatively, no OH-LIF signals can be observed when the sample was not treated by H_2+O_2, which suggests no surface •OH* is formed. Those results clearly confirm the presence of surface •OH* generated by H_2 and O_2 on Pd_1/TS-1@CN (1:100).

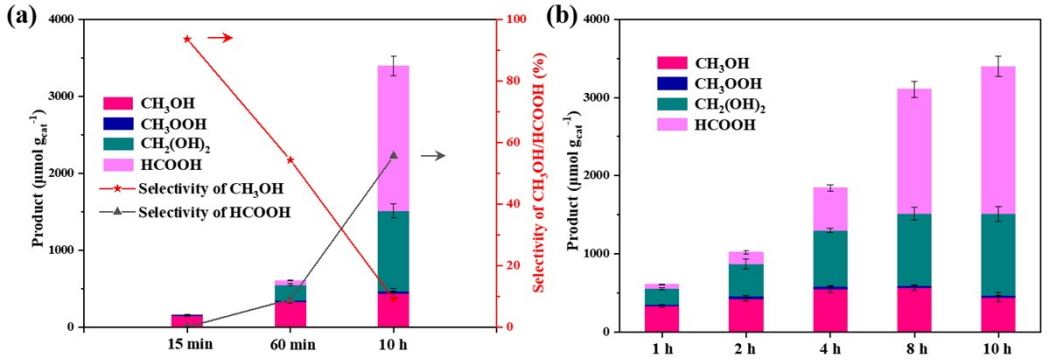

Fig. S55 The time-varying product distribution of DOM.

The selectivity of a single product such as methanol or HCOOH can be enhanced by tuning the reaction time. When the reaction time was shortened to 15 mins, the selectivity of methanol can reach 93.5% in all products. When the reaction time is prolonged to 10 h, the selectivity of formic acid is increased to 55.6% from 9.0 % at 1 h. Our DFT calculation results show that the methane was firstly converted to methanol, and then the methanol was further oxidized to methanediol and finally to formic acid dominated by surface hydroxyl groups, which verified our above results.

As the reaction time further prolongs, the productivity of C1 oxygenates is increased to 3,398 μmol•g_{cat}^{-1}•h^{-1} at 10 h from 606 μmol•g_{cat}^{-1}•h^{-1} at 1 h but the total selectivity of oxygenated species remains 100%, which indicates that the Pd_1/TS-1@CN (1:100) possesses long-term stability. Furthermore, the yield of methanediol accumulates approximately 5 times to 1,048 μmol•g_{cat}^{-1}•h^{-1} at 10 h from 200 μmol•g_{cat}^{-1}•h^{-1} at 1 h and formic acid gradually accumulate approximately 34 times to 1,887 μmol•g_{cat}^{-1}•h^{-1} at 10 h from 55 μmol•g_{cat}^{-1}•h^{-1} at 1 h with the extension of reaction time, while the yield of methanol exhibits a slight increase to 443 μmol•g_{cat}^{-1}•h^{-1} at 10 h from 329 μmol•g_{cat}^{-1}•h^{-1} at 1 h. These results indicates that the product generation process is from methanol to methanediol and finally to formic acid, which is in line with the DFT calculation as shown in manuscript **Fig. 6**.

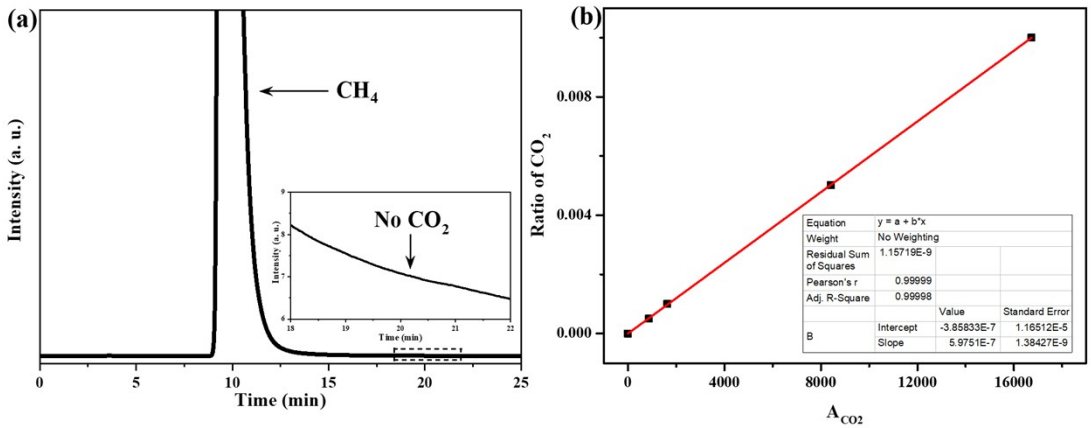

Fig. S56 (a) A typical chromatogram of Pd_1/TS-1@CN (1:100) after DOM. (b) Standard curve for CO_2 quantification. The ordinate (Y) represents the content of CO_2 and the abscissa (X) represents the peak area of CO_2 in the chromatogram.

Only CH_4 (9.8 min) could be detected in GC from gas mixture after DOM and there is no any CO_2 peak (20.1 min) observed in the spectrum (the detection limit of CO_2 is 1~2 ppm).

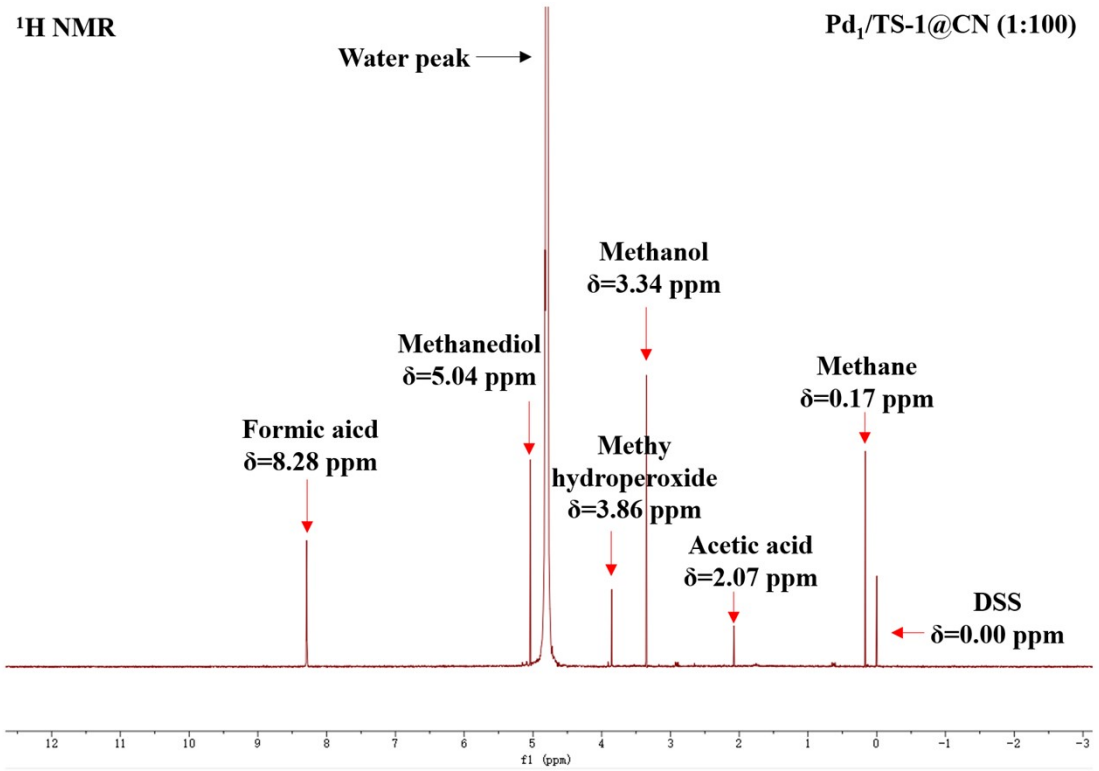

Fig. S57 Typical ^{1}H NMR of liquid mixtures over Pd_1/TS-1@CN (1:100). Reaction conditions: 20 mg catalysts dispersed in 20 ml D.I. H_2O, 15 ^oC with 28 bar CH_4, 6 bar O_2 and 6 bar H_2 for 1 h.

All ^{1}H NMR data were calibrated by phase correction and baseline before quantitative calculation of products for the DOM.

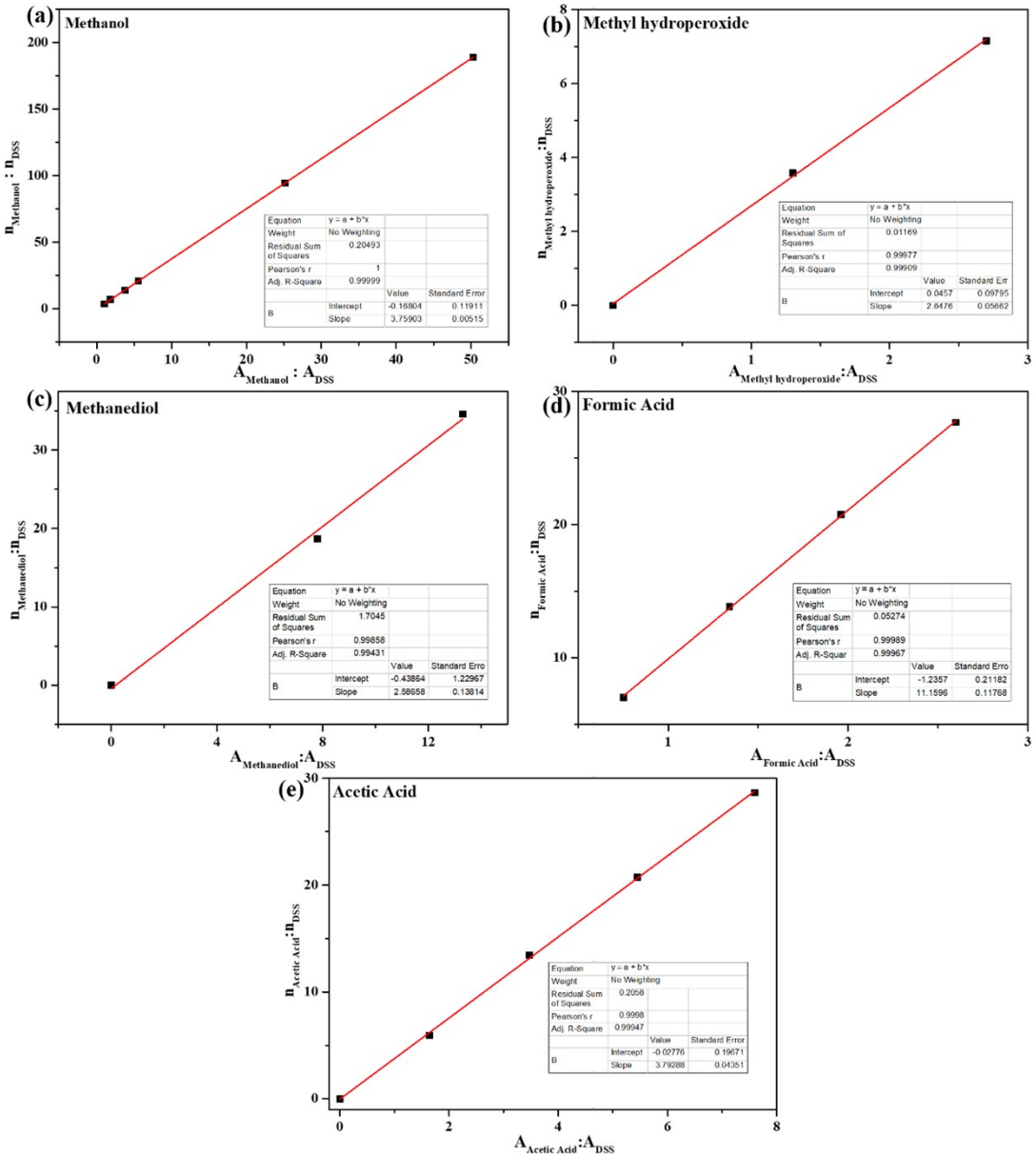

Fig. S58 The standard curves of (a) methanol, (b) methyl hydroperoxide, (c) methanediol, (d) formic acid and (e) acetic acid for calculating liquid product after DOM.

3-(trimethylsilyl)-1-propanesulfonic acid sodium salt (DSS) was used as a calibration standard to build standard curves. The X-axis represents the peak area ratio of the product vs DSS ($A_{product}$:A_{DSS}) in the ^{1}H NMR spectrum. The Y-axis represents the amount of the product vs DSS ($n_{product}$:n_{DSS}). The R-square of standard curves are all higher than 0.99, indicating the degree of fitting is reliable.

Table S1. Catalytic performance of the most promising catalysts in the DOM reported in literature recently.

Catalyst	Lighting/ Potential	Loading	P©	t	T	Yield of Liquid Oxygenates	Selectivity of Liquid Oxygenates	Stability	Oxidant/ Atmosphere	Notes
		(wt.%)	(bar)	(h)	(^{o}C)	(μmol g_{cat}^{-1} h^{-1})	(%)	(Cycles/ Time[f])		
Pd_1/TS-1@CN	**None**	**0.94***	**28[a]**	**1**	**15**	**9423**	**100**	**30**	**H_2+O_2**	**This work**
Pd_1/TS-1@CN	**None**	**0.94***	**28[b]**	**1**	**15**	**647**	**100**	**30**	**H_2+O_2**	**This work**
Fe-ferrierite	None	0.95	1	1	25	75	-	1	O_2	Ref [56]
Au_1/In_2O_3	Xe lamp	0.10*	20[c]	3	25	1983	97.6	3	O_2	Ref [57]
Au_{NPs}/In_2O_3	Xe lamp	2.42*	20[c]	3	25	2067	91	3	O_2	Ref [57]
$Ag/TiO_{2(001)}$	Xe lamp	3.2	20[d]	2	25	5400	90	-	O_2	Ref [58]
Au-CoO_x/TiO_2	Xe lamp	1(Au)	20[d]	2	25	2540	95	5	O_2	Ref [59]
$Au_{0.2}Cu_{0.15}$-ZnO	Xe lamp	0.2(Au)	19[e]	2	25	8900	79	5	O_2	Ref [60]
q-$BiVO_4$	Hg lamp	-	10[f]	3	25	766	52	5	O_2	Ref [61]
Defect-TiO_2 (H_2-600)	Xe lamp	-	19[f]	1	25	3620	93.1	5	O_2	Ref [62]
90% A-TiO_2	Xe lamp	-	20[g]	3	25	8090	98	5	O_2	Ref [63]
Pd-def-In_2O_3	LED	0.083*	19[e]	3	25	2995	99	5	O_2	Ref [40]
$Au_{0.3}$/c-WO_3	Xe lamp	0.3	19[e]	24	25	300	100	5	O_2	Ref [64]
0.1 wt% Au/ZnO	Xe lamp	0.1	20[d]	2	25	13145	95.4	5	O_2	Ref [65]
Cu-def-WO_3	LED	0.029*	19[e]	2	25	2490	96.5	5	O_2	Ref [66]
ER-MoS_2	None	-	0.1[h]	24	25	1.69	99	10	O_2	Ref [67]
$Cu_2@C_3N_4$	Xe lamp	0.35	10[i]	1	50	4897	98	5	O_2	Ref [23]
Au_1/BP	Xe lamp	0.20*	30[j]	2	90	113.5	99	10	O_2	Ref [68]
Ce-UiO-Cu(OH)	None	5.36*	30[k]	40	115	8378	96	-	O_2	Ref [69]
$Ru_{0.5}Ir_{0.5}O_2$/CuO	None	1 (1:1)	3[l]	3	150	450	100	5	O_2	Ref [70]
IrO_2/CuO	None	0.9(Ir)*	20[m]	3	150	680	-	5	O_2	Ref [71]
Cu/ZIF-8	None	20	1[n]	6	200	0.13	68	1	O_2	Ref [72]
Au-ZSM-5	None	0.5	23.2[o]	1	240	24	73	3	O_2	Ref [73]
PMOF-RuFe(OH)	Xe lamp	2.6(Fe)	0.5[p]	2	25	3485	100	10	O_2+H_2O	Ref [74]
As-prepared Ir	None	3.06*	19[q]	3	150	3682.2	67.5	5	CO+O_2	Ref [75]
H_2-treated Ir	None	3.06	19[q]	3	150	3300	62	1	CO+O_2	Ref [75]
$Ir_1Cu_1Pd_{0.1}$-ZSM-5	None	1.39(Ir)*	20[r]	1	150	1270	85	4	CO+O_2	Ref [76]
Rh_1/ZSM-5	None	0.5	20[r]	1	150	2721	100	-	CO+O_2	Ref [77]
1.0Rh/TiO_2/Cu^{2+}	None	1	23[s]	1	150	5200	99	4	CO+O_2	Ref [78]
Au/H-MOR	None	0.46*	20[t]	1	150	1377	80	5	CO+O_2	Ref [79]
Rh/ZSM-5	None	0.1	10[u]	1	150	8786	100	-	CO+O_2	Ref [80]
Rh_1/PMOF	Xe lamp	5.05*	15[v]	3	150	28333	78	7	CO+O_2	Ref [81]
(Pt/NPW)/TiO_2	Hg-Xe lamp	0.5	10[w]	4	20	22	10.2	3	CO+H_2O	Ref [82]
Fe-BN/ZSM-5	None	0.31*	24[x]	6	50	350	82	4	CO+H_2O_2	Ref [83]
AuPd/TiO_2	None	5(1:1)	30.5	0.5	2	53	83.0	-	H_2+O_2	Ref [41]
Pd/CsPMA	None	0.25(Pd)	20[y]	0.08	25	67.4	100	5	H_2+O_2	Ref [42]
AuPd/TiO_2	None	5(1:1)	30.5	0.5	50	116	83.3	-	H_2+O_2	Ref [41]

AuPd@ZSM-5-C16	None	5	0.048[z]	0.5	70	4600	100	10	H_2+O_2	Ref [84]
Pd_9Au_1 NWs	None	100	20[f]	0.5	70	2890	99	5	H_2+O_2	Ref [85]
PdCu/Z-5	None	0.14(Pd)*	24[π]	1	120	1630	95	-	H_2+O_2	Ref [86]
AC-Co_1/PCN_{KOH}	Xe lamp	4.01*	8	6	25	296	98	10	H_2O	Ref [87]
ZnO/Fe_2O_3	Xe lamp	6(Fe)	1	1.5	25	119.3	100	20	H_2O	Ref [88]
W-SA-PCN-7.5	Xe lamp	0.47*	5	5	25	991	100	6	H_2O	Ref [89]
Fe-N-C SAC	1.6 V_{RHE}	1.45*	1	0.5	25	191.3[#]	100	-	H_2O	Ref [90]
TiO_2/RuO_2/V_2O_5	2.0 V_{RHE}	5.6(V_2O_5)	1	1	25	306	100	-	H_2O	Ref [91]
Rh/ZnO	2.2 V_{RHE}	0.58*	1	-	25	928	100	24(h)[£]	H_2O	Ref [92]
NiO/Ni	1.4 V_{RHE}	3.02*	1	1	25	32	100	24(h)[£]	H_2O	Ref [93]
ZrO_2-NT/Co_3O_4	1.6 V_{RHE}	-	1	12	25	7106	100	10(h)[£]	H_2O	Ref [94]
Cu/Al_2O_3@NH_4BF_4	2.0 V_{RHE}	1	1	2	25	3641	100	25(h)[£]	H_2O	Ref [95]
Ga_2O_3	Xe lamp	-	1	2	40	355	95	10	H_2O	Ref [96]
Au-Pd colloid	None	100	30	0.5	23	8600	93	5	H_2O_2	Ref [97]
FeO_x/TiO_2	Xe lamp	0.33*	-	3	25	350	90	3	H_2O_2	Ref [98]
FeN_4/GN	None	2.7*	20	10	25	240	94	6	H_2O_2	Ref [99]
Fe/ZSM-5(66)	None	0.03*	30	0.5	25	7250	99	5	H_2O_2	Ref [100]
ZnO nanosheets	Xe lamp	-	1	1	50	2210	90.7	4	H_2O_2	Ref [101]
Cu-Fe(2/0.1)/ZSM-5	None	0.13(Fe)*	30	0.5	50	9200	96	-	H_2O_2	Ref [102]
Cu_1/ZSM-5	None	0.34*	30	0.5	50	8400	99	-	H_2O_2	Ref [103]
Cu-Fe/ZSM-5	None	2.5 (Fe)	30.5	0.5	50	8200	85	-	H_2O_2	Ref [104]
Fe/ZSM-5	None	2.5	30.5	0.5	50	820	83	-	H_2O_2	Ref [104]
Au-Pd/TiO_2	None	1 (1:1)	30.5	0.5	50	500	85	-	H_2O_2	Ref [105]
Pd_1/ZSM-5	None	0.01	30	0.5	50	7600	96	-	H_2O_2	Ref [106]
UiO-66-H	None	-	30	0.5	50	364	100	4	H_2O_2	Ref [107]
Cr_1/TiO_2	None	1	30	1	50	4390	93	4	H_2O_2	Ref [108]
Rh_1/CeO_2 NWs	None	0.29*	5	1	50	7000	93	10	H_2O_2	Ref [109]
$Pd_{0.25}Cu_{0.75}O$/C	None	1 (1:3)	5	1	50	2400	82	10	H_2O_2	Ref [110]
0.75FeCA800-4	None	0.1(Fe)	1	1.5	50	13.2	100	8	H_2O_2	Ref [111]
0.72Ru_1/UiO-66	None	0.72*	30	0.25	60	3703	100	3	H_2O_2	Ref [112]
MIL-53(Fe,Al)	None	0.3	30.5	2	60	3900	76	5	H_2O_2	Ref [113]
Rh_1/ZrO_2	None	0.3*	30	0.5	70	760	78	5	H_2O_2	Ref [114]

*: The actual loading of metal measured by ICP.
©: Pressure of methane.
#: The yield calculated on the basis of the overall catalyst weight.
£: Time (hours) is denoted as the stability of current density during the DOM.
a: Gas mixture contains 6 bar H_2, 6 bar O_2, 28 bar CH_4.
b: Gas mixture contains 1.2 bar H_2, 6 bar O_2, 28 bar CH_4 and 4.8 bar Ar, which is out of the explosive limits of $CH_4/H_2/O_2$ mixtures system (**Table S7**).
c: Gas mixture contains 10 bar O_2, 20 bar CH_4.
d: Gas mixture contains 1 bar O_2, 20 bar CH_4.
e: Gas mixture contains 1 bar O_2, 19 bar CH_4.
f: Gas mixture contains 10 bar O_2, 10 bar CH_4.
g: Gas mixture contains 5 bar O_2, 20 bar CH_4.
h: Gas mixture contains 1 bar O_2, 0.1 bar CH_4.

i: Feed gas at 3.0 MPa with 1.0 MPa CH_4, 0.5 MPa O_2, 1.5MPa N_2.
j: Gas mixture contains 3 bar O_2, 30 bar CH_4.
k: Gas mixture contains 6 bar O_2, 30 bar CH_4.
l: Gas mixture contains 1 bar air, 3 bar CH_4.
m: Gas mixture contains 1 bar air, 20 bar CH_4.
n: Gas mixture contains 1 bar O_2, 1 bar CH_4.
o: Gas mixture contains 1 bar O_2, 23.2 bar CH_4.
p: Gas mixture contains 0.5 bar O_2, 0.5 bar CH_4.
q: Gas mixture contains 4 bar O_2, 5 bar CO, 19 bar CH_4.
r: Gas mixture contains 2 bar O_2, 5 bar CO, 20 bar CH_4.
s: Gas mixture contains 3 bar O_2, 5 bar CO, 23 bar CH_4.
t: Gas mixture contains 5 bar O_2, 5 bar CO, 20 bar CH_4.
u: Gas mixture contains 2 bar O_2, 5 bar CO, 10 bar CH_4.
v: Gas mixture contains 4 bar O_2, 5 bar CO, 15 bar CH_4.
w: Gas mixture contains 2 bar CO, 8 bar CH_4.
x: Gas mixture contains 1 bar N_2, 5 bar CO, 24 bar CH_4.
y: Feed gas at 4.0 MPa with 0.4 MPa H_2, 0.03 MPa O_2, 1.0 MPa CH_4, 2.57 MPa N_2.
z: Feed gas at 3.0 MPa with 0.099 MPa H_2, 0.198 MPa O_2, 0.048 MPa CH_4, 1.851 MPa Ar, 0.804 MPa He.
π: Gas mixture contains 3 bar O_2, 8 bar H_2, 24 bar CH_4.

Table S2. The S_{BET} and pore volume of different catalysts.

Sample	S_{BET} (m^2/g)	V_{pore} (cm^3/g)
Pd_1/TS-1	388.2	0.272
Pd_1/TS-1@CN (1:100)	386.2	0.268
Pd_1/TS-1@CN (1:5)	355.8	0.221

Table S3. Actual Pd loading of before and after used Pd_1/TS-1 samples.

Samples	Pd content* (w. t.%)
Pd_1/TS-1 fresh	0.95
Pd_1/TS-1 used	0.95

*: The data was used to determinate the actual loading of metal by ICP-OES.

Table S4. EXAFS fitting results for Pd_1/TS-1.

Sample	Path	CN.	R (Å)	σ^2 (Å^2)	ΔE (eV)	R-factor
Pd_1/TS-1	Pd-O_{OH}	1.0	2.12	0.00073	1.33	0.017
	Pd-O_{FM}	2.0	2.00	0.00177		

CN. is the coordination number; R is interatomic distance (the bond length between central atoms and surrounding coordination atoms); σ^2 is Debye-Waller factor (a measure of thermal and static disorder in absorber-scatterer distances); ΔE is edge-energy shift (the difference between the zero kinetic energy value of the sample and that of the theoretical model). R factor is used to value the goodness of the fitting.

Table S5. EXAFS fitting results for Pd_1/TS-1@CN (1:100).

Sample	Path	CN.	R (Å)	σ^2 ($Å^2$)	ΔE (eV)	R-factor
Pd_1/TS-1@CN (1:100)	Pd-N	1.0	2.06	0.00072	1.20	0.009
	Pd-O_{FM}	2.0	2.02	0.00013		

CN. is the coordination number; R is interatomic distance (the bond length between central atoms and surrounding coordination atoms); σ^2 is Debye-Waller factor (a measure of thermal and static disorder in absorber-scatterer distances); ΔE is edge-energy shift (the difference between the zero kinetic energy value of the sample and that of the theoretical model). R factor is used to value the goodness of the fitting.

Table S6. Bader charge analysis of Pd cation at different sites.

Site	Bader charge of Pd (|e|)	Valence state
Pd_1/TS-1	+0.38	+1
Pd_1/TS-1@CN	+0.52	+1
Pd_2O bulk	+0.41	+1
PdO bulk	+0.89	+2

We performed the Bader charge analysis to identify the valence state of the palladium cations in the key intermediates with reference to the Bader charges of Pd^{+} in bulk Pd_2O, Pd^{2+} in bulk PdO.

Table S7. The explosive limits of $CH_4/H_2/O_2$ mixtures system.

Gas	Pressure (bar)	Concentration (%)	Explosive limits of sole component in air		Concentration of flammable gas mixtures (%)	Explosive limits of mixtures system	
			LFL (%)	UFL (%)		LFL_{mix} (%)	UFL_{mix} (%)
H_2	1.2	3	4	75.6	73	5.23	15.51
CH_4	28	70	5.3	15			
O_2	6	15	/	/			
Ar	4.8	12	/	/			

The reaction condition of DOM over the synthesized Pd_1/TS-1@CN catalysts has been changed at 70% CH_4, 15% O_2, 3% H_2, 12% Ar with a total pressure of 4 MPa which is out of the explosive limits of $CH_4/H_2/O_2$ mixtures system. The lower flammability limit (LFL) and the upper flammability limit (UFL) for mixture gas is measured as:

$$LFL_{mix} = \frac{1}{\sum_{i=1}^{n} \frac{y_i}{LFL_i}} \qquad (6)$$

LFL_i is the lower flammable limit for component i (in volume%) of component i in fuel and air, y_i is the mole fraction of component i on a combustible basis, and n is the number of combustible species.

Similarly

$$UFL_{mix} = \frac{1}{\sum_{i=1}^{n} \frac{y_i}{UFL_i}} \qquad (7)$$

The calculated explosion zone is 5.23%-15.51% and the flammability gas in our system is 73% which is not in the explosion zone. Meanwhile, 3% H_2 also allows the H_2 concentration to fall within the explosion limit range of H_2/O_2.

Table S8. Intensity of hydroxyl radicals signal in EPR data.

Catalyst	Intensity of hydroxyl radical signal (a. u.)*				Total Intensity (a. u.)	Normalization (a. u.)
	a	b	c	d		
Added-H_2O_2	497	1033	959	484	2973	~49
In situ H_2+O_2	11	20	21	10	62	1

***: The signal intensity of hydroxyl radical is determined by the area of the integral peak.**

The amount of hydroxyl radical species from in situ H_2+O_2 sample is defined as "1". The amount of hydroxyl radical species produced by dissociating hydrogen peroxide of the additionally added H_2O_2 is ~49 times higher than that of the in situ H_2+O_2 sample.

Table S9. The free energy barrier of activation of CH_4 in the micropores of TS-1 solution at 288 K.

Elementary steps	**$\Delta G^{\neq}$ (eV)**
$CH_4 + \bullet OH^* \rightarrow \bullet CH_3 + H_2O$	0.92
$CH_4 + OH^{-*} \rightarrow \bullet CH_3 + H_2O$	1.49
$CH_4 + \bullet OH \rightarrow \bullet CH_3 + H_2O$	1.34

The Bader charge analysis (Table S10, ESI†) reveals that the two surface adsorbed hydroxyl species formed from H_2 and O_2 on Pd_1/TS-1@CN can be classified as one hydroxyl radical (•OH*) and one hydroxyl anion (OH^{-}*) at $[Pd(OH)_2]^+$**.** The activities of two hydroxyl species adsorbed on the surface and free hydroxyl radicals (free •OH) to activate methane C-H bonds were calculated and compared.

Table S10. Bader charge analysis of oxygen species at different sites.

Site	Bader charge of O (|e|)	Oxygen species
$[PdOH]^+$/TS-1	-1.08	OH^-*
$[PdH(OH)_2]^+$/TS-1	-0.86, -1.02	•OH*, OH^-*
$[PdO_2]^+$/TS-1@CN	-0.66	O^-
$[Pd(OH)_2]^+$/TS-1@CN	-0.63, -1.01	•OH*, OH^-*
$[Pd(OH)(H_2O)]^+$/TS-1@CN	-0.95	OH^-*
$[(OH)_2]$-$Pd_{cluster}$	-1.09, -1.27	OH^-*, OH^-*
$[(OH)_2]$-Pd(111)	-1.01, -1.02	OH^-*, OH^-*
Free •OH	-0.60	•OH
H_2O_2	-0.62	O^-/O_2^{2-}
H_2O	-1.12	O^{2-}

According to the recent work[115-117], the formal charge of the oxygen species could be identified based on the reference Bader charges of the O^-/O_2^{2-} in H_2O_2 (-0.62 |e|) and the O^{2-} in H_2O (-1.12 |e|). The Bader charge of the key site of Pd_1/TS-1@CN was calculated, and the charge of the key oxygen species was listed from the above table, further indicating the state of the adsorbed hydroxyl group.

Supplementary References

1 Y. Lou, Y. Zheng, X. Li, N. Ta, J. Xu, Y. Nie, K. Cho and J. Liu, *J. Am. Chem. Soc.* 2019**, 141**, 19289-19295.
2 Y. Lou, F. jiang, W. Zhu, L. Wang, T. Yao, S. Wang, B. Yang, B. Yang, Y. Zhu and X. Liu, *Appl. Catal. B Environ.* 2021**, 291**, 120122.
3 B. Qiao, J. Liu, Y.-G. Wang, Q. Lin, X. Liu, A. Wang, J. Li, T. Zhang and J. Liu, *ACS Catal.* 2015**, 5**, 6249-6254.
4 W. Zhan, Q. He, X. Liu, Y. Guo, Y. Wang, L. Wang, Y. Guo, A. Y. Borisevich, J. Zhang, G. Lu and S. Dai, *J. Am. Chem. Soc.* 2016**, 138**, 16130-16139.
5 H.-C. Yang, R. Z. Waldman, M.-B. Wu, J. Hou, L. Chen, S. B. Darling and Z.-K. Xu, *Adv. Funct. Mater.* 2018**, 28**, 1705327.
6 D. Tsukamoto, A. Shiro, Y. Shiraishi, Y. Sugano, S. Ichikawa, S. Tanaka and T. Hirai, ACS Catal. 2012**, 2**, 599-603.
7 D. M. Davies and M. E. Deary, *J. Chem. Soc., Perkin Trans.* 1992**, 2**, 559-562.
8 G. Kresse and J. Hafner, *Phys. Rev. B.* 1994**, 49**, 14251.
9 J. P. Perdew, J. A. Chevary, S. H. Vosko, K. A. Jackson, M. R. Pederson, D. J. Singh and C. Fiolhais, *Phys. Rev. B.* 1992**, 46**, 6671.
10 S. Grimme, S. Ehrlich and L. Goerigk, *J. Comput. Chem.* 2011**, 32**, 1456-1465.
11 J. P. Perdew, K. Burke and M. Ernzerhof, *Phys. Rev. Lett.* 1996**, 77**, 3865.
12 A. Alavi, P. Hu, T. Deutsch, P. L. Silvestrelli and J. Hutter, *Phys. Rev. Lett.* 1998**, 80**, 3650.
13 L. Zhang, X.-M. Cao and P. Hu, *Appl. Surf. Sci.* 2017**, 392**, 456-471.
14 P. J. Dauenhauer and O. A. Abdelrahman, *ACS Central. Sci.* 2018**, 4**, 1235-1243
15 A. El Brahmi and S. Abderafi, *Int. J. Environ. Sci. Technol.* 2023, **20**, 2127-2140.
16 C. Hank, S. Gelpke, A. Schnabl, R. J. White, J. Full, N. Wiebe, T. Smolinka, A. Schaadt, H.-M. Henning and C. Hebling, *Sustain. Energy. Fuels.* 2018, **2**, 1244-1261.
17 C. Martínez de León, C. Ríos and J. J. Brey, *Int. J. Hydrogen. Energy.* 2023, **48**, 11885-11898.
18 B. Adhikari, C. J. Orme, J. R. Klaehn and F. F. Stewart, *Sep. Purif. Technol.* 2021, **268**, 118703.
19 C. Qi, S. Li, Z. Yang, Z. Xiao, L. Zhao, F. Yang, G. Ning, X. Ma, C. Wang, J. Xu and J. Gao, *Carbon* 2022**, 186**, 530-538.
20 X. Yu, V. L. Zholobenko, S. Moldovan, D. Hu, D. Wu, V. V. Ordomsky and A. Y. Khodakov, *Nat. Energy* 2020**, 5**, 511-519.
21 G. Peng, J. Wu, M. Wang, J. Niklas, H. Zhou and C. Liu, *Nano Lett.* 2020**, 20**, 2879-2885.
22 Y. Liang, Y. Li, H. Wang, J. Zhou, J. Wang, T. Regier and H. Dai, *Nat. Mater.* 2011**, 10**, 780-786.
23 P. Xie, J. Ding, Z. Yao, T. Pu, P. Zhang, Z. Huang, C. Wang, J. Zhang, N. Zecher-Freeman, H. Zong, D. Yuan, S. Deng, R. Shahbazian-Yassar and C. Wang, *Nat. Commun.* 2022**, 13**, 1375.
24 X. Zheng, J. Zhang, J. Wang, X. Qi, J. M. Rosenholm and K. Cai, *J. Phys. Chem. C* 2015**, 119**, 24512-24521.
25 A. Palazov, C. C. Chang and R. J. Kokes, *J. Catal.* 1975**, 36**, 338-350.
26 Z. Hong, B. Shen, Y. Chen, B. Lin and B. Gao, *J. Mater. Chem. A* 2013**, 1**, 11754-11761.
27 C. Lv, Y. Qian, C. Yan, Y. Ding, Y. Liu, G. Chen and G. Yu, *Angew. Chem. Int. Ed.* 2018**, 57**, 10246-10250.
28 P. A. Thiel and T. E. Madey, *Surf. Sci. Reports* 1987**, 7**, 211-385.
29 L. Zhuang, Z. Jia, Y. Wang, X. Zhang, S. Wang, J. Song, L. Tian and T. Qi, *Chem. Eng. J.* 2022**, 438**, 135585.
30 J. Liu, Z. Chen, C. Liu, B. Zhang, Y. Du, C.-F. Liu, L. Ma, S. Xi, R. Li, X. Zhao, J. Song, X. Z. Sui, W. Yu, L. Miao, J. Jiang, M. J. Koh and K. P. Loh, *J. Mater. Chem. A* 2021**, 9**, 11427-11432.
31 Z. Li, X. Lu, W. Sun, L. Leng, M. Zhang, H. Li, L. Bai, D. Yuan, J. H. Horton, Q. Xu and J. Wang, *Appl. Catal. B Environ.* 2021**, 298**, 120535.
32 Z. Li, Q. Ren, X. Wang, W. Chen, L. Leng, M. Zhang, J. H. Horton, B. Liu, Q. Xu, W. Wu and J. Wang, *ACS Appl. Mater. Interfaces* 2021**, 13**, 2530-2537.
33 N. Wang, X. Zhao, R. Zhang, S. Yu, Z. H. Levell, C. Wang, S. Ma, P. Zou, L. Han, J. Qin, L. Ma, Y. Liu and H. L. Xin, *ACS Catal.* 2022**, 12**, 4156-4164.
34 G. Li, P. Vassilev, M. Sanchez-Sanchez, J. A. Lercher, E. J. M. Hensen and E. A. Pidko, *J. Catal.* 2016**, 338**, 305-312.
35 N. Agarwal, S. J. Freakley, R. U. McVicker, S. M. Althahban, N. Dimitratos, Q. He, D. J. Morgan, R. L. Jenkins, D. J. Willock, S. H. Taylor, C. J. Kiely and G. J. Hutchings, *Science* 2017**, 358**, 223-227.

36 R. J. Lewis, K. Ueura, X. Liu, Y. Fukuta, T. E. Davies, D. J. Morgan, L. Chen, J. Qi, J. Singleton, J. K. Edwards, S. J. Freakley, C. J. Kiely, Y. Yamamoto and G. J. Hutchings, *Science* 2022**, 376**, 615-620.
37 O. Pozdnyakova, D. Teschner, A. Wootsch, J. Kröhnert, B. Steinhauer, H. Sauer, L. Toth, F. C. Jentoft, A. Knop-Gericke, Z. Paál and R. Schlögl, *J. Catal.* 2006**, 237**, 17-28.
38 C. Pan and Y. Zhu, *Environ. Sci. Technol.* 2010**, 44**, 5570-5574.
39 C. Pan, G. Bian, Y. Zhang, Y. Lou, Y. Zhang, Y. Dong, J. Xu and Y. Zhu, *Appl. Catal. B Environ.* 2022**, 316**, 121675.
40 L. Luo, L. Fu, H. Liu, Y. Xu, J. Xing, C.-R. Chang, D.-Y. Yang and J. Tang, *Nat. Commun.* 2022**, 13**, 2930.
41 M. H. Ab Rahim, M. M. Forde, R. L. Jenkins, C. Hammond, Q. He, N. Dimitratos, J. A. Lopez-Sanchez, A. F. Carley, S. H. Taylor, D. J. Willock, D. M. Murphy, C. J. Kiely and G. J. Hutchings, *Angew. Chem. Int. Ed.* 2013**, 52**, 1280-1284.
42 S. Wang, V. Fung, M. J. Hülsey, X. Liang, Z. Yu, J. Chang, A. Folli, R. J. Lewis, G. J. Hutchings, Q. He and N. Yan, *Nat. Catal.* 2023, **6**, 895-905.
43 D. Lin, X. Zheng, X. Feng, N. Sheng, Z. Song, Y. Liu, X. Chen, Z. Cai, D. Chen and C. Yang, *Green Energy Environ.* 2020, **5**, 433-443.
44 S. Praserthdam, M. Rittiruam, K. Maungthong, T. Saelee, S. Somdee and P. Praserthdam, *Sci. Rep.* 2020, **10**, 18952.
45 Z. Su, S. Yi, W. Zhang, X. Xu, Y. Zhang, S. Zhou, B. Niu and D. Long, *Nano-Micro Lett.* 2023, **15**, 183.
46 E. M. Stuve, S. W. Jorgensen and R. J. Madix, *Surf. Sci.* 1984**, 146**, 179-198.
47 K. L. Yeung, S. T. Yau, A. J. Maira, J. M. Coronado, J. Soria and P. L. Yue, *J. Catal.* 2003**, 219**, 107-116.
48 D. Ciuparu, E. Perkins and L. Pfefferle, *Appl. Catal. A-Gen.* 2004**, 263**, 145-153.
49 K.-i. Ataka, T. Yotsuyanagi and M. Osawa, *J. Phys. Chem. C* 1996**, 100**, 10664-10672.
50 P. A. Giguère and K. B. Harvey, *J. Mol. Spectrosc.* 1959**, 3**, 36-45.
51 I. X. Green, C. Buda, Z. Zhang, M. Neurock, J. T. Yates and Jr, *J. Phys. Chem. C* 2010**, 114**, 16649-16659.
52 I. X. Green, W. Tang, M. Neurock and J. T. Yates, *Science* 2011**, 333**, 736-739.
53 X.-M. Cao, H. Zhou, L. Zhao, X. Chen and P. Hu, *Chinese Chem. Lett.* 2021**, 32**, 1972-1976.
54 Y. Murakami, K. Endo, I. Ohta, A. Y. Nosaka and Y. Nosaka, *J. Phys. Chem. C.* 2007, **111,** 11339-11346.
55 Y. Murakami, E. Kenji, A. Y. Nosaka and Y. Nosaka, *J. Phys. Chem. B.* 2006, **110,** 16808-16811.
56 E. Tabor, J. Dedecek, K. Mlekodaj, Z. Sobalik, P. C. Andrikopoulos and S. Sklenak, *Sci. Adv.* 2020**, 6**, eaaz9776.
57 Y. Jiang, S. Li, S. Wang, Y. Zhang, C. Long, J. Xie, X. Fan, W. Zhao, P. Xu, Y. Fan, C. Cui and Z. Tang, *J. Am. Chem. Soc.* 2023**, 145**, 2698-2707.
58 N. Feng, H. Lin, H. Song, L. Yang, D. Tang, F. Deng and J. Ye, *Nat. Commun.* 2021**, 12**, 4652.
59 H. Song, X. Meng, S. Wang, W. Zhou, S. Song, T. Kako and J. Ye, *ACS Catal.* 2020**, 10**, 14318-14326.
60 L. Luo, Z. Gong, Y. Xu, J. Ma, H. Liu, J. Xing and J. Tang, *J. Am. Chem. Soc.* 2022**, 144**, 740-750.
61 Y. Fan, W. Zhou, X. Qiu, H. Li, Y. Jiang, Z. Sun, D. Han, L. Niu and Z. Tang, *Nat. Sustain.* 2021**, 4**, 509-515.
62 P.-P. Luo, X.-K. Zhou, Y. Li and T.-B. Lu, *ACS Appl. Mater. Interfaces* 2022**, 14**, 21069-21078.
63 Y. Jiang, W. Zhao, S. Li, S. Wang, Y. Fan, F. Wang, X. Qiu, Y. Zhu, Y. Zhang, C. Long and Z. Tang, *J. Am. Chem. Soc.* 2022**, 144**, 15977-15987.
64 S. Wei, X. Zhu, P. Zhang, Y. Fan, Z. Sun, X. Zhao, D. Han and L. Niu, *Appl. Catal. B Environ.* 2021**, 283**, 119661.
65 H. Song, X. Meng, S. Wang, W. Zhou, X. Wang, T. Kako and J. Ye, *J. Am. Chem. Soc.* 2019**, 141**, 20507-20515.
66 L. Luo, X. Han, K. Wang, Y. Xu, L. Xiong, J. Ma, Z. Guo and J. Tang, *Nat. Commun.* 2023**, 14**, 2690.
67 J. Mao, H. Liu, X. Cui, Y. Zhang, X. Meng, Y. Zheng, M. Chen, Y. Pan, Z. Zhao, G. Hou, J. Hu, Y. Li, G. Xu, R. Huang, L. Yu and D. Deng, *Nat. Catal.* 2023**, 20230921**.
68 L. Luo, J. Luo, H. Li, F. Ren, Y. Zhang, A. Liu, W.-X. Li and J. Zeng, *Nat. Commun.* 2021**, 12**, 1218.
69 N. Antil, M. Chauhan, N. Akhtar, R. Kalita and K. Manna, *J. Am. Chem. Soc.* 2023**, 145**, 6156-6165.

70 L. Yang, J. Huang, S. Dai, X. Tang, Z. Hu, M. Li, H. Zeng, R. Luque, P. Duan and Z. Rui, *J. Mater. Chem. A* 2020**, 8**, 24024-24030.
71 L. Yang, J. Huang, R. Ma, R. You, H. Zeng and Z. Rui, *ACS Energy Lett.* 2019**, 4**, 2945-2951.
72 Y. Yang, S. Kanchanakungwankul, S. Bhaumik, Q. Ma, S. Ahn, D. G. Truhlar and J. T. Hupp, *J. Am. Chem. Soc.* 2023**, 145**, 22019-22030.
73 G. Qi, T. E. Davies, A. Nasrallah, M. A. Sainna, A. G. R. Howe, R. J. Lewis, M. Quesne, C. R. A. Catlow, D. J. Willock, Q. He, D. Bethell, M. J. Howard, B. A. Murrer, B. Harrison, C. J. Kiely, X. Zhao, F. Deng, J. Xu and G. J. Hutchings, *Nat. Catal.* 2022**, 5**, 45-54.
74 B. An, Z. Li, Z. Wang, X. Zeng, X. Han, Y. Cheng, A. M. Sheveleva, Z. Zhang, F. Tuna, E. J. L. McInnes, M. D. Frogley, A. J. Ramirez-Cuesta, L. S. Natrajan, C. Wang, W. Lin, S. Yang and M. Schröder, *Nat. Mater.* 2022**, 21**, 932-938.
75 H. Li, M. Fei, J. L. Troiano, L. Ma, X. Yan, P. Tieu, Y. Yuan, Y. Zhang, T. Liu, X. Pan, G. W. Brudvig and D. Wang, *J. Am. Chem. Soc.* 2023**, 145**, 769-773.
76 M. Li, J. Shan, G. Giannakakis, M. Ouyang, S. Cao, S. Lee, L. F. Allard and M. Flytzani-Stephanopoulos, *Appl. Catal. B Environ.* 2021**, 292**, 120124.
77 J. Shan, M. Li, L. F. Allard, S. Lee and M. Flytzani-Stephanopoulos, *Nature* 2017**, 551**, 605-608.
78 F. Gu, X. Qin, M. Li, Y. Xu, S. Hong, M. Ouyang, G. Giannakakis, S. Cao, M. Peng, J. Xie, M. Wang, D. Han, D. Xiao, X. Wang, Z. Wang and D. Ma, *Angew. Chem. Int. Ed.* 2022**, 61**, e202201540.
79 W. Wang, W. Zhou, Y. Tang, W. Cao, S. R. Docherty, F. Wu, K. Cheng, Q. Zhang, C. Copéret and Y. Wang, *J. Am. Chem. Soc.* 2023**, 145**, 12928-12934.
80 Y. Tang, Y. Li, V. Fung, D.-e. Jiang, W. Huang, S. Zhang, Y. Iwasawa, T. Sakata, L. Nguyen, X. Zhang, A. I. Frenkel and F. Tao, *Nat. Commun.* 2018**, 9**, 1231.
81 H. Li, C. Xiong, M. Fei, L. Ma, H. Zhang, X. Yan, P. Tieu, Y. Yuan, Y. Zhang, J. Nyakuchena, J. Huang, X. Pan, M. M. Waegele, D.-e. Jiang and D. Wang, *J. Am. Chem. Soc.* 2023**, 145**, 11415-11419.
82 C. Dong, M. Marinova, K. B. Tayeb, O. V. Safonova, Y. Zhou, D. Hu, S. Chernyak, M. Corda, J. Zaffran, A. Y. Khodakov and V. V. Ordomsky, *J. Am. Chem. Soc.* 2023**, 145**, 1185-1193.
83 B. Wu, T. Lin, Z. Lu, X. Yu, M. Huang, R. Yang, C. Wang, C. Tian, J. Li, Y. Sun and L. Zhong, *Chem* 2022**, 8**, 1658-1672.
84 J Z. Jin, L. Wang, E. Zuidema, K. Mondal, M. Zhang, J. Zhang, C. Wang, X. Meng, H. Yang, C. Mesters and F.-S. Xiao, *Science* 2020**, 367**, 193.
85 Y. Xu, D. Wu, P. Deng, J. Li, J. Luo, Q. Chen, W. Huang, C. M. Shim, C. Jia, Z. Liu, Y. Shen and X. Tian, *Appl. Catal. B Environ.* 2022**, 308,** 121223.
86 B. Wu, T. Lin, M. Huang, S. Li, J. Li, X. Yu, R. Yang, F. Sun, Z. Jiang, Y. Sun and L. Zhong, *Angew. Chem. Int. Ed.* 2022**, 61**, e202204116.
87 J. Ding, Z. Teng, X. Su, K. Kato, Y. Liu, T. Xiao, W. Liu, L. Liu, Q. Zhang, X. Ren, J. Zhang, Z. Chen, O. Teruhisa, A. Yamakata, H. Yang, Y. Huang, B. Liu and Y. Zhai, *Chem* 2023**, 9**, 1017-1035.
88 X. Meng, X. Cui, N. P. Rajan, L. Yu, D. Deng and X. Bao, *J. Am. Chem. Soc.* **2022,** *144*, 12357-12366.
89 Y. Wang, J. Zhang, W.-X. Shi, G.-L. Zhuang, Q.-P. Zhao, J. Ren, P. Zhang, H.-Q. Yin, T.-B. Lu and Z.-M. Zhang, *Adv. Mater.* 2022**, 34**, 2204448.
90 C. Kim, H. Min, J. Kim and J. H. Moon, *Energy Environ. Sci. 2023,* **16**, 3158-3165.
91 R. S. Rocha, R. M. Reis, M. R. V. Lanza and R. Bertazzoli, *Electrochim. Acta* 2013**, 87**, 606-610.
92 Z. Xie, M. Chen, Y. Chen, A. Guan, Q. Han and G. Zheng, *J. Phys. Chem. C* 2021**, 125**, 13324-13330.
93 Y. Song, Y. Zhao, G. Nan, W. Chen, Z. Guo, S. Li, Z. Tang, W. Wei and Y. Sun, *Appl. Catal. B Environ.* 2020**, 270**, 118888.
94 C. Oh, J. Kim, Y. J. Hwang, M. Ma and J. H. Park, *Appl. Catal. B Environ.* 2021**, 283**, 119653.
95 E. Ponticorvo, M. Iuliano, C. Cirillo and M. Sarno, *Chem. Eng. J.* 2023**, 451**, 139074.
96 C. Han, Y. Cao, W. Yu, Z. Huang, F. Dong, L. Ye, S. Yu and Y. Zhou, *J. Am. Chem. Soc.* 2023**, 145**, 8609-8620.
97 N. Agarwal, S. J. Freakley, R. U. McVicker, S. M. Althahban, N. Dimitratos, Q. He, D. J. Morgan, R. L. Jenkins, D. J. Willock, S. H. Taylor, C. J. Kiely and G. J. Hutchings, *Science* 2017**, 358**, 223-227.
98 J. Xie, R. Jin, A. Li, Y. Bi, Q. Ruan, Y. Deng, Y. Zhang, S. Yao, G. Sankar, D. Ma and J. Tang, *Nat. Catal.* 2018**, 1**, 889-896.
99 X. Cui, H. Li, Y. Wang, Y. Hu, L. Hua, H. Li, X. Han, Q. Liu, F. Yang, L. He, X. Chen, Q. Li, J. Xiao, D. Deng and X. Bao, *Chem* 2018**, 4,** 1902-1910.

100 K. Zhu, S. Liang, X. Cui, R. Huang, N. Wan, L. Hua, H. Li, H. Chen, Z. Zhao, G. Hou, M. Li, Q. Jiang, L. Yu and D. Deng, *Nano Energy* 2021**, 82**, 105718.
101 S. Zhu, X. Li, Z. Pan, X. Jiao, K. Zheng, L. Li, W. Shao, X. Zu, J. Hu, J. Zhu, Y. Sun and Y. Xie, *Nano Lett.* 2021**, 21**, 4122-4128.
102 T. Yu, Z. Li, L. Lin, S. Chu, Y. Su, W. Song, A. Wang, B. M. Weckhuysen and W. Luo, *ACS Catal.* 2021**, 11**, 6684-6691.
103 X. Tang, L. Wang, B. Yang, C. Fei, T. Yao, W. Liu, Y. Lou, Q. Dai, Y. Cai, X.-M. Cao, W. Zhan, Y. Guo, X.-Q. Gong and Y. Guo, *Appl. Catal. B Environ.* 2021**, 285**, 119827.
104 C. Hammond, M. M. Forde, M. H. Ab Rahim, A. Thetford, Q. He, R. L. Jenkins, N. Dimitratos, J. A. Lopez-Sanchez, N. F. Dummer, D. M. Murphy, A. F. Carley, S. H. Taylor, D. J. Willock, E. E. Stangland, J. Kang, H. Hagen, C. J. Kiely and G. J. Hutchings, *Angew. Chem. Int. Ed. Engl.* 2012**, 51**, 5129-5133.
105 M. H. Ab Rahim, M. M. Forde, R. L. Jenkins, C. Hammond, Q. He, N. Dimitratos, J. A. Lopez-Sanchez, A. F. Carley, S. H. Taylor, D. J. Willock, D. M. Murphy, C. J. Kiely and G. J. Hutchings, *Angew. Chem. Int. Ed.* 2013**, 52**, 1280-1284.
106 W. Huang, S. Zhang, Y. Tang, Y. Li, L. Nguyen, Y. Li, J. Shan, D. Xiao, R. Gagne, A. I. Frenkel and F. Tao, *Angew. Chem. Int. Ed. Engl.* 2016**, 55**, 13441-13445.
107 G. Fang, J.-N. Hu, L.-C. Tian, J.-X. Liang, J. Lin, L. Li, C. Zhu and X. Wang, *Angew. Chem. Int. Ed.* 2022**, 61**, e202205077.
108 Q. Shen, C. Cao, R. Huang, L. Zhu, X. Zhou, Q. Zhang, L. Gu and W. Song, *Angew. Chem. Int. Ed.* 2020**, 59**, 1216-1219.
109 S. Bai, F. Liu, B. Huang, F. Li, H. Lin, T. Wu, M. Sun, J. Wu, Q. Shao, Y. Xu and X. Huang, *Nat. Commun.* 2020**, 11**, 954.
110 S. Bai, Y. Xu, P. Wang, Q. Shao and X. Huang, *ACS Catal.* 2019**, 9**, 6938-6944.
111 K. Zheng, Y. Wu, Z. Hu, X. Jiao, L. Li, Y. Zhao, S. Wang, S. Zhu, W. Liu, W. Yan, Y. Sun and Y. Xie, *Nano Lett.* 2021**, 21**, 10368-10376.
112 G. Fang, F. Wei, J. Lin, Y. Zhou, L. Sun, X. Shang, S. Lin and X. Wang, *J. Am. Chem. Soc.* 2023**, 145**, 13169-13180.
113 D. Y. Osadchii, A. I. Olivos-Suarez, Á. Szécsényi, G. Li, M. A. Nasalevich, I. A. Dugulan, P. S. Crespo, E. J. M. Hensen, S. L. Veber, M. V. Fedin, G. Sankar, E. A. Pidko and J. Gascon, *ACS Catal.* 2018**, 8**, 5542-5548.
114 Y. Kwon, T. Y. Kim, G. Kwon, J. Yi and H. Lee, *J. Am. Chem. Soc.* 2017**, 139**, 17694-17699.
115 A. S. Rosen, J. M. Notestein and R. Q. Snurr, *Angew. Chem. Int. Ed.* 2020**, 132**, 19662-19670.
116 M. Zeng, L. Cheng, Q. Gu, B. Yang, B. Yu, J. Xu, Y. Zhang, C. Pan, X.-M. Cao, Y. Lou and Y. Zhu, *EES. Catal.* 2023**, 1**, 153-161.
117 B. Yu, L. Cheng, S. Dai, Y. Jiang, B. Yang, H. Li, Y. Zhao, J. Xu, Y. Zhang, C. Pan, X.-M. Cao, Y. Zhu and Y. Lou, *Adv. Sci.* 2023**, 10,** 2302143.